Universitá degli Studi di Trieste
Dipartimento di Fisica
Scuola di Dottorato in Fisica
Ciclo XXIX

A Comprehensive ARPES Study on the Anomalous Transport Properties and Topological Character of $ZrTe_5$

Settore Scientifico Disciplinare:
FIS-03 Fisica della Materia

Dottoranda: Giulia Manzoni
Coordinatore: Prof. Livio Lanceri
Supervisore di Tesi: Prof. Fulvio Parmigiani

Anno Accademico 2015/2016

PhD Candidate:
Giulia Manzoni

Supervisor:
Prof. F. Parmigiani

School Coordinator:
Prof. L. Lanceri

Reviewers:
Prof. C. Dallera
Prof. D. N. McIlroy
Prof. K. Roßnagel

Defence Committee:
Prof. G. Comelli
Prof. L. Perfetti
Prof. W. Widdra

Contents

Introduction **vii**

1 $ZrTe_5$: Structural, Electronic and Topological Properties **1**

1.1 Crystal Structure 1

1.2 Transport Properties 3

1.2.1 Resistivity 3

1.2.2 Thermopower 4

1.2.3 Positive Out of Plane Magnetoresistance 5

1.3 Theoretical Models for the Anomalous Transport Properties of $ZrTe_5$ 7

1.3.1 Charge Density Wave Formation 7

1.3.2 Polarons Formation 9

1.3.3 The Energy Shift of the Band Structure 11

1.4 Topological Properties of $ZrTe_5$ 14

1.4.1 Quantum Hall Insulators and Quantum Spin Hall Insulators 14

1.4.2 Topological Insulators 16
1.4.3 3D Topological Dirac Semimetals 19
1.4.4 Negative in Plane Magnetoresistance 19
1.4.5 The Predicted Topological Phase Transition. Theory and Experiments. 21

2 Experimental Techniques **27**
2.1 Angle Resolved Photoelectron Spectroscopy (ARPES) . 27
2.1.1 Photoelectric Effect 27
2.1.2 Conservation Laws 28
2.1.3 3-Step Model and Photoemission Intensity 30
2.1.4 Ultra High Vacuum and Hemispherical Electron Energy Analyzers 34
2.1.5 Time Resolved ARPES 35
2.1.6 The T-ReX Laboratory at Elettra 36
2.1.7 Geometry of the ADRESS Beamline at SLS and of the APE Beamline at Elettra 38
2.1.8 Spin Resolved ARPES 40
2.2 X-Ray Diffraction (XRD) 44
2.2.1 Why XRD? 44
2.2.2 The XRD1 Beamline 45

3 The Temperature Dependence of the $ZrTe_5$ Band Structure **47**
3.1 Electronic Band Structure at Low Temperature 48
3.2 Te $4d_{3/2}$ and $4d_{5/2}$ Core Levels 51
3.3 Multiple Domains at the Surface 53
3.4 Evolution of the Electronic Band Structure as a Function of the Temperature 55
3.4.1 Laser-ARPES Data 55
3.4.2 UV-ARPES Data 56
3.5 Rigid Shift of the Electronic Band Structure 59
3.6 Revealing the Unoccupied Band Structure by 2PPE . . 64
3.7 Conclusions 66

4 Ultrafast Optical Control of the Electronic Properties of $ZrTe_5$ 67
4.1 Effect of the Optical Excitation 67
4.2 Study of the Pump-Probe Dynamics 71
4.3 Fluence Dependence of the Pump-Probe Dynamics . . . 74
4.4 Conclusions 77

5 On the Strong Topological Insulator Character of $ZrTe_5$ 79
5.1 Disentangling Bulk and Surface States in Proximity of the Fermi Energy: UV- and SX-ARPES Measurements . 81
5.2 Gapless States Observed with Scanning Tunneling Microscopy and Spectroscopy 87
5.3 Theoretical Prediction of the Topological Phase Transition and Estimation of $b/2$ with X-Ray Diffraction . . . 91
5.4 Circular Dichroic ARPES Measurements 95
5.5 The Spin Polarized State at the Surface 97
5.6 Conclusions 101

Concluding Remarks 103

Bibliography 106

List of Publications 125

Introduction

Pentatelluride compounds, $HfTe_5$ and $ZrTe_5$, have been matter of great attention from their first synthesis in 1973 [1]. The reason originates from the transport anomalies shown by these materials, like the resistivity peak at a characteristic temperature, T*, [2], along with a sudden switch of the sign of the thermopower at the same T* [3].

$HfTe_5$ and $ZrTe_5$ belong to the family of layered transition-metal tellurides, MTe_n, where M is a transition-metal and $n = 1, 2, 3, 5$. Several members of this family have been matter of intense studies for their rich physics. In particular, WTe_2 has become object of intense debates after the discovery of its non-saturating extreme magnetoresistance [4] and, with $MoTe_2$ [5], it has also been predicted to be a type-II Weyl semimetal [6], a new phase of quantum matter. Furthermore, ZrTe has been theoretically foretold to belong to a new class of topologically non-trivial materials, i.e. a triple-point topological metals [7]. $ZrTe_3$ has attracted the attention of the scientific community for the formation of a charge density wave (CDW) at low temperature [8].

In this quite unique scenario, the possible applications of $HfTe_5$ and $ZrTe_5$ in thermoelectrics [9, 10] have promoted an intense study aimed at explaining the origins of their transport anomalies [11–13], although with little success so far.

In these last years, $ZrTe_5$ has also gained increasing attention about

its topological character [14,15] and an intense debate about this question [14–23] has been recently developed.

However, an unambiguous experimental confirmation of the topological character of $ZrTe_5$ is still elusive.

The scope of this thesis is the study of the electronic band structure of $ZrTe_5$ by means of Angle Resolved Photoelectron Spectroscopy (ARPES), a powerful and direct technique capable to address the open questions related to the physics of this material.

We have examinated the evolution of the electronic band structure of $ZrTe_5$ upon cooling, showing that the long lasting question related to the anomalous resistivity peak at T* [1] can be related to a non-monotonic band shift observed as a function of the sample temperature [24,25]. Moreover, we have proven, by means of time resolved ARPES, the possibility to manipulate and control, on the ultrafast time scale, the sample temperature, and, consequently, the transport properties of the material [24]. Finally, the strong topological character of $ZrTe_5$ has been shown, thanks to a multi-technique approach comprising of ultra violet and soft X-ray ARPES, scanning tunneling microscopy (STM) and scanning tunneling spectroscopy (STS), density functional theory (DFT) calculations, X-ray diffraction (XRD) [25,26] and spin resolved ARPES [27].

The author of this thesis has planned and performed the equilibrium and out-of-equilibrium ARPES measurements reported in this manuscript and their analysis. These measurements have been carried out both at the T-Rex laboratory, in Trieste, and at several synchrotron facilities, after the evaluation of scientific proposals. The author has also written a scientific proposal and she has partecipated to the XRD experiment whose results are reported in Chapter 5.

The thesis is organized as follows:

1. Chapter 1 introduces the physical properties of $ZrTe_5$. The debate about its anomaly in the transport properties is reviewed. The topological character of $ZrTe_5$ is also discussed, summarizing the main results of the last few years.

2. Chapter 2 describes the experimental techniques. Particular at-

tention is given to ARPES, both at equilibrium and out of equilibrium and with different light sources and detectors.

3. Chapter 3 reports the experimental results obtained as a function of the sample temperature. Complementary results taken in two different laboratories are discussed.

4. In chapter 4, the study of the evolution of the electronic properties of $ZrTe_5$ on the ultrafast time scale is presented. In this chapter, the possibility to optically control the transport properties of the material is proved.

5. Chapter 5 shows our contribution to the outgoing debate about the topological character of $ZrTe_5$. Multiple techniques have been exploited, in collaboration with other scholars and reaching the conclusion that this material is a bulk strong topological insulator (STI).

6. The last chapter is devoted to the concluding remarks, summarizing the main results and the open perspectives of this project.

1

$ZrTe_5$: Structural, Electronic and Topological Properties

Layered transition-metal tellurides, MTe_n (being $n = 1, 2, 3$ or 5 and M a transition metal) have been intensively studied for their rich physics [4–8].

In particular, $ZrTe_5$, first synthetized in 1973 [1], has been recently object of a strong debate because of its elusive topological properties, renewing the interests on this material with anomalous transport properties [2, 3, 9–30].

1.1 Crystal Structure

$ZrTe_5$ crystallizes in the orthorhombic layered structure with space group Cmcm (D_{2h}^{17}), as shown in Fig. 1.1 (a).

The crystal structure is formed by trigonal prismatic chains of $ZrTe_3$ which run along the a axis. The prismatic chains are connected along the c axis by parallel zigzag chains of Te atoms thus forming 2D $ZrTe_5$ sheets in the $a - c$ plane. The sheets of $ZrTe_5$ stack along the b

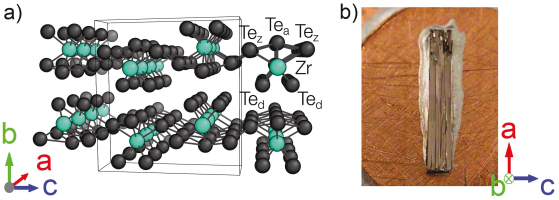

Figure 1.1: (a) The crystal structure of $ZrTe_5$. (b) A sample of $ZrTe_5$ glued on a sample holder.

axis, forming a layered structure.

Each $ZrTe_5$ layer has nominally neutral charge, and the interlayer distance (along the b axis) is $\sim$ 7.25 Å. A small interlayer binding energy, due to van der Waals interactions, has been estimated equal to 12.5 meV/Å^2 for $ZrTe_5$, a value comparable to that measured for graphite, equal to 9.3 meV/Å^2 [14]. The unit cell contains four formula units and it has dimensions $a = 3.974$ Å, $b = 14.492$ Å and $c = 13.730$ Å [1].

The bulk Brillouin zone (BZ) of $ZrTe_5$ is shown in figure 1.2 (black) with the projected surface BZ of three-dimensional $ZrTe_5$. The projected surface (010) is represented in green and it has been investigated in this thesis by means of different experimental techniques.

The specimens object of this study have been grown by direct vapor transport technique mediated by iodine gas [31]. As it can be seen in Fig. 1.1 (b), samples grow as single crystals naturally oriented along the a axis.

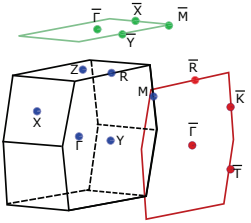

Figure 1.2: Brillouin zone and projected Brillouin zone of $ZrTe_5$.

1.2 Transport Properties

1.2.1 Resistivity

The resisitivity $\rho(T)$ of $ZrTe_5$ presents a significant anomalous peak at T* [2], with an increase by a factor 3, respect to its room temperature (RT) value, $\rho(300\ K) \sim 0.6\ \Omega$cm. Looking at several studies on $ZrTe_5$ present in the literature, it is possibile to find samples with a temperature T*$\sim$ 60 K [16], T* $\sim$ 135 K [32], T* $\sim$ 140 K [2] and T* $\sim$ 170 K [33]. It has been also shown that a controlled substitutional doping of the material can strongly vary the value of T*. $ZrSe_xTe_{5-x}$, $Zr_{1-x}Ti_xTe_5$ or $Hf_xZr_{1-x}Te_5$ samples, for example, can lower the value of T* of $\sim$ 70 K [9,10,32]. Consequently, it seems that the different T* values reported for several undoped $ZrTe_5$ crystals [2,16,32,33] depend on the defect density determined by the crystal growth.

The samples object of this thesis project, grown with a direct vapor transport technique with iodine methods, show the resistivity peak at T* $\sim$ 150 K as reported in figure 1.3. The $\rho(T)/\rho(300K)$ graph reported in figure 1.3 was determined using a four-point method, with the contacts made using silver paste and gold wires. The current was

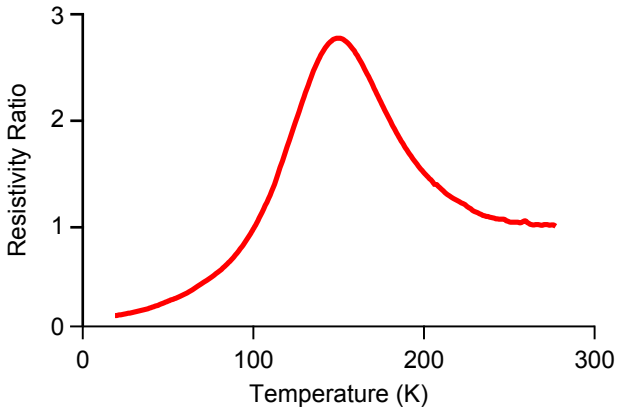

Figure 1.3: Resistivity ratio $\rho(T)/\rho(300K)$ of $ZrTe_5$.

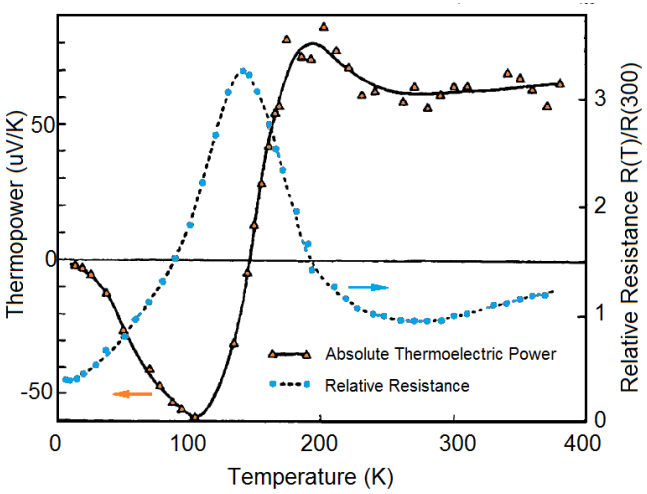

Figure 1.4: Thermopower (yellow triangles) and relative resistance (blu dots) of single crystals of $ZrTe_5$, as adapted from [3].

injected along the a axis [1]. The measured samples had dimensions of $\sim 1 \times 0.2 \times 0.05$ mm^3, as for those used for ARPES, XRD and STM experiments.

1.2.2 Thermopower

$ZrTe_5$ is also known for its thermoelectric properties that are related to its transport anomaly. In fact, the resisitivity peak is accompained by a sign change in the thermopower [3] in proximity of the same T*. As shown in figure 1.4, the thermopower changes sign from positive to negative, cooling across T*.

The thermopower of a material quantifies the magnitude of the induced electric voltage in response to a temperature gradient across the material and it can be either positive or negative. In conductors,

[1] The resisitivity characterization of the $ZrTe_5$ samples object of this study was performed by *A. Akrap* of the Université de Genève.

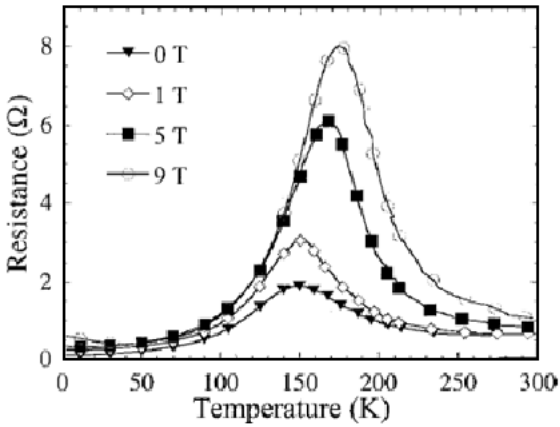

Figure 1.5: Magneto-Resistance of $ZrTe_5$. The applied magnetic field is perpendicular to the surface. Figure taken from [34].

the sign of the thermopower is fully defined by the nature of the free charge carriers. The thermopower is negative for negatively charged carriers, such as electrons, and positive for positive carriers, such as electron holes. Consequently, the change of sign of the $ZrTe_5$ thermopower across T* could be related to a change of the charge carriers sign.

1.2.3 Positive Out of Plane Magnetoresistance

$ZrTe_5$ displays also a marked magnetoresistance (MR), the property of a material to change its electrical resistance under the application of an external magnetic field.

Tritt et al., in 1999 [34], have shown that the resistivity of $ZrTe_5$ can be increased applying a magnetic field, B, perpendicular to the surface, *i.e.* along the b axis. The resulting resistivity measurements are shown in figure 1.5.

As previously described, at zero magnetic field the material exhibits a resistivity peak at T* when a current I is injected along the

a axis. The action of a transverse magnetic field, $B \perp I$ and $B//b$, has a remarkable effect on the resistive peak of the material, shifting the peak to higher temperatures ($T^*_{MR} > T^*$) and triggering a large enhancement of the resistivity peak value. The maximum applied magnetic field is $\sim$ 9 T reaching $T^*_{MR}(9T) \sim 200K$ and $\rho(T^*_{MR}(9T))/\rho(300K) \sim 8$ [34].

1.3 Theoretical Models for the Anomalous Transport Properties of $ZrTe_5$

Several models have been developed trying to describe the origin of the transport anomalies of $ZrTe_5$. In the following, the most relevant will be briefly overviewed. The limits of these theoretical models and how they were confuted by experiments will be highlighted, when possible.

1.3.1 Charge Density Wave Formation

A charge density wave (CDW) is a periodic distortion of the lattice accompanied by a periodic modulation of the charge carriers density. CDW formation occurs also in materials with two- or three-dimensional band structures, however, the simplest ground state and phase transition descriptions are based on one-dimensional models [35].

Consider a one-dimensional metal with one free electron per atom at T = 0 K. In the absence of electron-electron or electron-phonon interaction, the ground state corresponds to the situation shown in figure 1.6 (a). The electronic states are filled up to the Fermi level (E_F) and the lattice is a periodic array of atoms with lattice constant a.

In the presence of an electron-phonon interaction, it is energetically favorable to introduce an additional periodic lattice distortion with period λ related to the Fermi wave vector k_F by

$$\lambda = \frac{\pi}{k_F} \tag{1.1}$$

This distorsion creates a new periodicity and new Bragg planes where gaps are open at E_F, as shown in figure 1.6 (b), where the case of a half-filled band is displayed. Since only the states between $k = 0$ and $k = \pm k_F$ are occupied, the development of a gap leads to a lowering of the electronic energy [35].

At finite temperatures, electrons excited across the single-particle gap screen the electron-phonon interaction. This in turn leads to the reduction of the gap and of the magnitude of the lattice distortion,

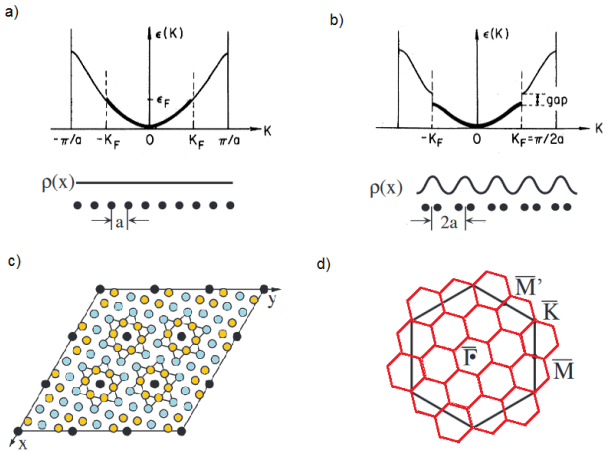

Figure 1.6: (a) 1D-system with uniform charge distribution and conduction band for a linear chain of atoms. (b) 1D-system with CDW reconstruction. Band structure for the insulator with opening of the gap 2Δ at the Fermi level. The atomic position in the chain are modulated. (c) Sketch of the Ta plane with CDW-induced ($\sqrt{13} \times \sqrt{13}$) reconstruction. (d) TaS_2 normal state (large hexagon) and CDW-induced (small hexagons) BZs. Adapted from Ref. [42].

and eventually to a second-order transition at the Peierls temperature T_P [36]. The material is a metal above the transition while it is a semiconductor below T_P with a temperature-dependent gap $\Delta(T)$ [35].

In a large class of transition metal-chalcogenides (for example $NbSe_2$ [37], $NbSe_3$ [38], TaS_2 [39], TaS_3 [40], $ZrTe_3$ [8]) and in 'blue bronze' $K_{0.3}MoO_3$ [41], the electron gas and the ion lattice spontaneously develop a periodic modulation when the temperature decreases below a critical transition temperature T_p.

Figure 1.6 (c) shows an example of 2D CDW in the prototypical TaS_2 [42]. At $T < T_P$, the position of the Ta atoms are distorted in the so-called David-star reconstruction, thus reflecting CDW formation. As a consequence of the lattice deformation, also the Brilluion

zone (BZ) has a reconstruction, shown in figure 1.6 (d). The superperiodicity becomes also detectable with low-energy diffraction (LEED), resulting in the appearence of extra spots. The CDW formation is often accompanied by anomalies in the transport properties. This is the case of TaS_2, for example, as reported in Ref. [43].

The structural low dimensionality of $ZrTe_5$ crystals and the anomalies in the transport properties of this material were interpreted as clues of the formation of CDWs at $T<T^*$, as previously shown for other materials. However, a search for direct evidences supporting the formation of CDWs in $ZrTe_5$ has failed. Notably, superlattice spots signature of the CDW were absent in the x-ray diffraction (XRD) patterns and in the LEED patterns [2]. Moreover, also evidences of nonlinear electrical conductivity, considered hallmark of CDW formation, were missing [11].

The formation of CDW in $ZrTe_5$ was definitively discarted thanks to an XRD study at 80 K of the Zr chain direction (*i.e.* a^*). Measurements acquired along [100] and [010] directions revealed no additional diffraction peaks, excluding the CDW formation in $ZrTe_5$ [11].

1.3.2 Polarons Formation

Large electron phonon coupling can be responsible of ground state even more exotic than the CDW phase. The motion of an electron through a polar solid can be schematized as in figure 1.7 (a). If the interaction between the electron and the positevely charged ions is strong enough, the electron can create a local lattice distortion as cartooned in Fig. 1.7 (b). Under such an interaction the electron is not anymore adeguately described in terms of a *bare* electron. The electron is instead *dressed* by a self-induced polarization in the ionic crystal, hence forming a quasiparticle, known as *polaron*.

The polaron is characterized by an effective mass $m^* > m_{electron}$ and a radius r_p that accounts for the size of the lattice distortion. If $r_p > l$, where l is the material lattice constant, the polaron is viewed as a *large* (delocalized) polaron, while if $r_p < l$, the polaron is considered as a *small* (localized) polaron, largely influencing the transport

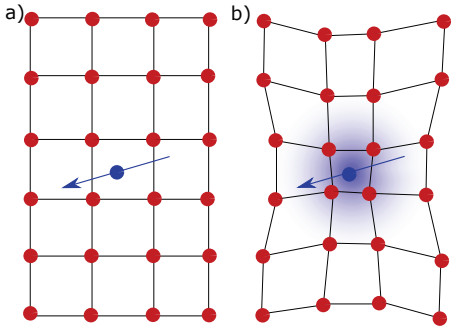

Figure 1.7: (a) An electron (blue) moves unpertubed through a region containing positevely charged ions (red). (b) The electron produces a lattice distortion that forms a new quasi-particle called polaron.

properties.

M. Rubinstein in 1999 has proposed to explain the charge transport properties of $ZrTe_5$ in terms of polarons [12]. In his work, three distinct temperature regions were recognized:

- At low temperatures, as a result of purely *elastic interactions*, polarons jump from site to site, guaranteering a low resistivity value.
- At some intermediate temperature, $T \sim$ T*, coexisting *inelastic* events affect the lifetime of the polaronic states, thereby increasing the solid's resistivity as the temperature increases.
- At higher temperatures, polarons hop via a thermal excitation process involving an activation energy and the resistivity decreases again.

In this sequence of events, from a metal-like behaviour, when resistivity increases with increasing temperature, to an insulator-like behaviour, when resistivity decreases with increasing temperature, no sudden phase transition occurs. Rather, a competition between elastic and inelastic events gives rise to a gradual metal-insulator transition.

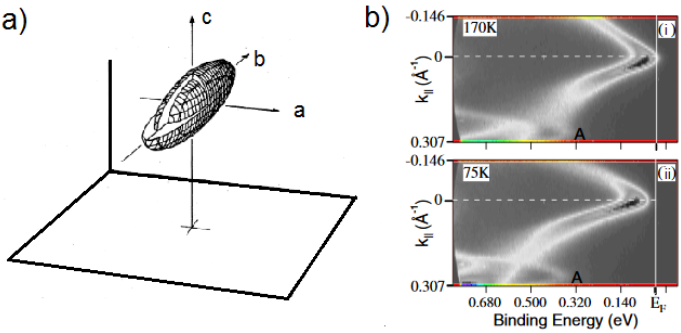

Figure 1.8: (a) A three-dimensional representation of the ellipsoidal Fermi surfaces derived from the Shubnikov-de Haas effect, taken from [44]. (b) Intensity maps of the density of states of $ZrTe_5$ acquired along the Γ - X high symmetry direction for (i) T = 170 K and (ii) T = 75 K. Adapted from [13].

This is the observable feature that first has brought to consider $ZrTe_5$ as a possible polaronic solid.

However, this model was not supported by experimental evidences of polaronic charge carriers in $ZrTe_5$.

1.3.3 The Energy Shift of the Band Structure

The origin of the anomalous transport properties of $ZrTe_5$ was attributed also to temperature dependent modifications of the band structure.

In 1985, *Kamm et al.* have reported a study of the Fermi Surfaces (FS) of $ZrTe_5$ at T $\sim$ 4.2 K, by exploiting the Shubnikov-de Haas effect [44]. The resulting FS of $ZrTe_5$, shown in figure 1.8 (a), is composed by three concentric and nearly-degenerate 3-dimensional ellipsoids elonged along the b direction. A representation of this ellipsoidal FS is shown in figure 1.8 (a).

McIlroy et al. have performed the first ARPES study on $ZrTe_5$ [13]. They have recorded the band structure of $ZrTe_5$ at 170 K and 75 K, also

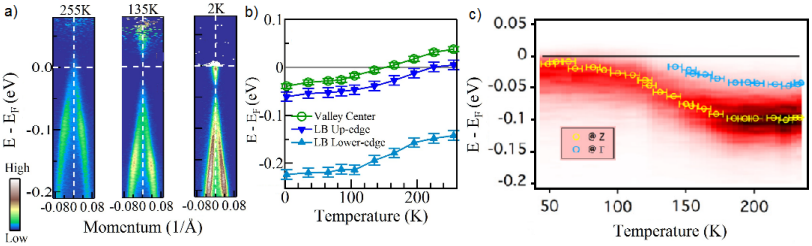

Figure 1.9: (a) $ZrTe_5$ band structure measured along Γ-X at three characteristic temperatures. Adapted from [18]. (b) Energy positions of three reference quantities extracted from the band structure at different temperatures. Adapted from [18]. (c) A sequence of EDCs measured at the Z point as a function of the temperature. The yellow (blue) markers indicate the peak positions as obtained by a simple Voigt fit at Y (Γ). Adapted from [19].

shown in figure 1.8 (b). These two temperatures are respectively larger and smaller than T*, found to be T* $\sim$ 135 K for the samples used in their experiments. By measuring in the temperature range $20 - 170$ K with a 22 eV photon energy, they have observed at the Γ point a band gap. This was interpreted as the indication of a semiconducting phase. In addition, the band structure was observed to shift towards higher binding energies when lowering the temperature, as shown in figure 1.8 (b). Consistently with the Shubnikov-de Haas study of Ref. [44], *McIlroy et al.* have concluded that a metal-semiconductor phase transition is occurring between 4.2 K and 20 K.

Moreover, the band structure at the Γ point appears parabolic, composed by two different quasi-degenerate bands, which was proposed to correspond to a heavy hole (HH) band and a light hole (LH) band.

Noticebly, *McIlroy and co-workers* are not the only group who focused its attention on the temperature behaviour of the band structure of $ZrTe_5$. In the recent years, many experimental works have reported discrepancies and very controversials results.

- Recent ARPES data of *Zhang et al.* [18], acquired between $\sim$ 300 K and $\sim$ 2 K, have shown that the band shift is monotonic toward

higher binding energies, when the sample is cooled, as shown in figure 1.9 (a). As a consequence the bottom of the upper band (UB) is detected below the Fermi energy (E_F) at $\sim$ 2 K [18]. The total band shift was estimated and it is reported in figure 1.9 (b). In this work, the band structure at Γ seems composed by one single parabolic-like band.

- Other ARPES experiments, performed at 24 K [17] and at 20 K [16], have shown the Valence Band (VB) of $ZrTe_5$ crossing E_F, in contrast with what discussed in the previous point [18].

- *Moreschini et al.* have performed ARPES experiments between $\sim$ 250 K and $\sim$ 50 K, reporting a rigid shift of the band structure toward lower binding energies by cooling the sample [19]. These results are summarized in Fig. 1.9 (c). Moreover, two different bands have been observed at Γ in proximity of E_F and the authors have discussed them as a folding along the k_b direction with a superperiodicity b.

These results seem to be in conflict, hence opening the question about the relation between temperature and band structure in $ZrTe_5$.

1.4 Topological Properties of $ZrTe_5$

1.4.1 Quantum Hall Insulators and Quantum Spin Hall Insulators

The observation of the anomalous *Quantum Hall* effect (QH) [45], reported first by *K. von Klitzing* on a metal-oxide semiconductor, in two-dimensional insulating materials has opened to new and unespected perspectives. This discovery was regarded as a major breakthrough for solid state physics and *K. von Klitzing* was awarded the Nobel prize in 1985 *"for the discovery of the quantized Hall effect"* [46]. This effect consists in the quantization at low temperature and under high magnetic field of the Hall conductivity, σ, as multiple of

$$\sigma = \nu e^2/h \tag{1.2}$$

where ν is called *filling factor* and it represents the number of the Landau levels that are filled [47].

The theoretical description of this quantization was first addressed in term of gauge invariance by *Laughlin* [48], who was awarded in 1998 the Nobel prize *"for the discovery of a new form of quantum fluid with fractionally charged excitations"* [46]. His contribution was successively generalized by *Halperin* who has shown that under strong magnetic field the Landau levels form delocalized extended states at the boundary of the sample [49].

In the QH regime, free electrons give rise also to quantized cyclotron orbits in the bulk becoming localized. At the edges, gapless states are formed due to a skipping orbits mechanism [50], as schematized in figure 1.10 (a). These edge-states carry current with opposite chiralities, and they cannot be modified by disorder.

In general, we define an insulator as a material characterized by an energy bandgap. However, such definition is not sufficient in the case of the QH conductance at the edge states. As proposed by *Fu and Kane* an insulator can be defined as a system in which the electronic properties are local and not affected by boundary effects [51]. Following this definition, the QH state does not share the same property of

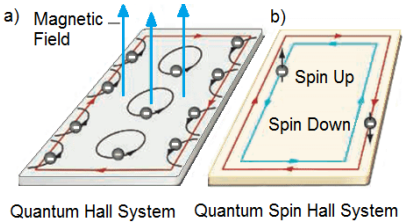

Figure 1.10: (a) A QH insulator and (b) a QSH insulator.

locality and it belongs to a different class of materials. Consequently, the atomic insulators and the QH state are topologically distinct.

Thouless, Kohmoto, Nightingale and den Nijs showed that the QH state is identified by an integer number, the TKNN number [52], which represents the topological invariant which distinguishes this state of matter from conventional insulators. The passage from a QH state to a conventional insulating state is not adiabatic and involves a so-called *topological phase transition*. Significantly, *D. J. Thouless*, with *F. Ducan M. Haldane* and *J. M. Kosterliz*, were awarded the physics Nobel prize in 2016 *"for theoretical discoveries of topological phase transitions and topological phases of matter"* [46].

The stability of the edge states in the presence of disorder motivated several studies, with the aim to find a QH state beyond the constrains of low temperature and high magnetic field. This state of matter was proposed to exist preserving the time-reversal symmetry but with the special requirement of strong spin-orbit coupling [53]. This novel topological phase of matter is named *Quantum Spin Hall Insulator* (QSHI), whose existence was theoretically advanced by *C. L. Kane* and *E. J. Mele* in 2005 [54]. The experimental evidence of the existance of the QSHI state was reported in 2007 with a study of *M. Köning* on HgTe/HgCdTe quantum wells [55].

QSHIs have similar, although distinct, non trivial topological properties as the QH insulators. QSHI are invariant under time-reversal symmetry, they show a bulk gap and the gapless edge states disperse within the bulk gap, as shown in figure 1.10 (b).

The spin degeneracy in the edge states is resolved as consequence of the strong spin-orbit coupling (SOC). The edge states are not spin-degenerate, and the concept of edge chirality is substituted by the concept of spin helicity: two states with opposite spin counterpropagate at a given edge [54,56,57]. Therefore, in QSHI the edge states are spin filtered, and QSHI systems are the ideal candidates for spintronics and quantum computing applications.

The QSHI phase is associated with a novel Z_2 topological invariant, which distinguishes it from an ordinary insulator [56]. The Z_2 classification, which is defined for time reversal invariant Hamiltonians, is analogous to the TKNN number classification of the quantum Hall effect [56].

1.4.2 Topological Insulators

Between 2007 and 2009, three theoretical groups [58–60] independently discovered that the topological characterization of the QSHI state has a natural generalization in three dimensions. Among them, *Moore* and *Balents* [59] have coined the term *topological insulator* (TI) to describe this new electronic phase. The single Z_2 topological invariant is now replaced by four numbers, ν_0, ν_1, ν_2, ν_3, fully characterizing the topological phases.

The simplest non-trivial 3D TI can be viewed as stacking layers of the 2D QSHI [47]. When 2D QSHI systems are stacked, the edge states form surface states on the four lateral surfaces but the top and the bottom surfaces have no surface states. This is the case of the so-called *weak* TI, where $\nu_0 = 0$ and at least one of the other indexes is different from zero.

If surface states along all the surfaces of the material are formed, we are in the presence of a *strong* TI. Here, the fourth invariant, ν_0 is $= 1$.

The indices ν_1, ν_2, ν_3 can be interpreted as Miller indices describing the orientation of the layers and indicating on which surfaces is possibile to find, or not, the surface state.

In 2006 *Bernevig et al.* [61] have proposed a general model for

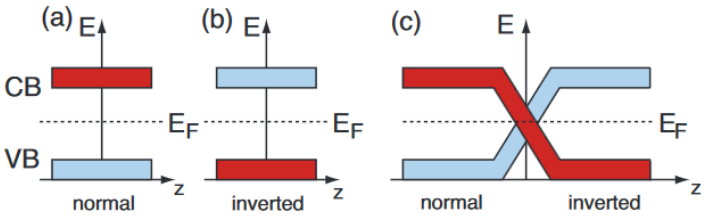

*Figure 1.11: Simplified band diagram for semiconductors, showing the valence band (VB) and conduction band (CB) energies as a function of position (*i.e. *the edges signify the macroscopic ends of the sample). (a) Colour (parity) ordering of VB and CB in a normal semiconductor. (b) Semiconductor with an inverted band gap. (c) Joining a semiconductor with a normal band gap and one with an inverted band gap while maintaining the symmetry of the states gives rise to metallic interface states. Figure taken from [62].*

identifying the topologically protected or trivial nature of a material, based on the *bulk band inversion*. In a normal (*i.e.* topologically trivial) semiconductor the valence band maximum and the conduction band minimum have p-character, *i.e.* negative parity, and s-character, *i.e.* positive parity, respectively. This case is represented in figure 1.11 (a). This ordering can be inverted in materials characterized by a small band gap and a large spin-orbit interaction, because the degeneracy of the p levels is splitted, leading to the creation of $j = 1/2$ and $j = 3/2$ states, and the latter can move above the s level, as shown in figure 1.11 (b). When these two kind of materials, with normal and inverted gap ordering, are joined together, as depicted in figure 1.11 (c), their electronic states must be connected satisfying the conservation of the parity number. This implies that the negative and positive parities states have to cross E_F at the interface, giving rise to two metallic surface states. In general when dealing with topological insulator, such interface with a trivial insulator is naturally provided by the vacuum. Vacuum, in fact, can be viewed as a system with "normal" band ordering [62].

As in QSHI the edge states are spin filtered, the TI phase is char-

acterized by metallic spin-polarized surface states lying in the bulk bandgap [51]. The existence of such states is required by the bulk band structure, in contrast to the more fragile metallic surface states frequently encountered on semiconductor surfaces [63]. These states are stable under small perturbation of the Hamiltonian and only the closing of the bulk band gap may be responsible for their disappearence [62, 63].

The high symmetry points of the reciprocal space connected from a reciprocal lattice vector are called Time Reversal Invariant Momenta (TRIM) points. The spin degeneracy is the consequence of the simultaneous presence of time reversal and spatial inversion symmetries, which can be represented, respectively

$$E(k,\uparrow) = E(-k,\uparrow) \tag{1.3}$$

$$E(k,\uparrow) = E(-k,\downarrow) \tag{1.4}$$

Therefore, the so-called Kramers' spin degeneracy follows:

$$E(k,\uparrow) = E(k,\downarrow). \tag{1.5}$$

Nonetheless, time reversal symmetry is sufficient alone to guarantee the spin degeneracy in a finite number of points of the reciprocal space, which are exactly the TRIM points.

The first bulk topological insulator found experimentally was obtained by doping the semimetal Bi with Sb to obtain $Bi_{1-x}Sb_x$ ($x \sim 0.1$) [51, 53, 64], a material with a very small band gap, but stable surface states that, not surprisingly, strongly resemble those on the pure Bi surface [65]. Unfortunately, $Bi_{1-x}Sb_x$ has several disadvantages for technological applications, since it grows with a random crystal structure, that implies poor crystal quality and a rather complicated surface (111) electronic structure. Furthermore, the bulk band gap is of the order of 30 meV restricting the potential applications to low temperatures.

Later, a *second generation* of topological insulators, such as Bi_2Se_3 and Bi_2Te_3, have been discovered [66–70]. These materials are ordered layered crystals, they have a gap size of ~ 300 meV, and their surface

electronic structure consists of a single, metallic state with a Dirac cone-like dispersion.

1.4.3 3D Topological Dirac Semimetals

TIs are not the only new states of quantum matter , since recently three-dimensional (3D) topological Dirac semimetals (3D TSMs) have been proposed to further extend the topological classification of materials [71, 72].

A 3D TSM is a bulk analogue of graphene. However, while graphene and similar TIs host 2D linearly dispersing state, *i.e.* 2D Dirac particles, a 3D TSM possesses bulk Dirac fermions that disperse linearly along all three momentum directions [47, 73, 74]. $NaBi_3$ and Cd_3As_2 represent the first exponents of this topological class of materials. The 3D Dirac point is experimentally observed close to E_F, thus resulting in a small density of states at E_F. This, combined with an extremely large band velocity results in a high charge mobility.

In addition, the electronic properties of 3D TSM are topologically protected. The semimetallic character, resulting from the degeneracy of the bulk valence and conduction band in a single Dirac point, is not accidental but it respects topological constrains imposed by the lattice symmetry [75]. As a consequence, the electronic properties at E_F are insensitive to small perturbation of the Hamiltonian. All together, the high mobility and the topological protection of the bulk 3D state make 3D TSMs ideal platforms for novel applications and transport devices.

1.4.4 Negative in Plane Magnetoresistance

In the previous section we have briefly reviewed the anomalies in the transport properties of $ZrTe_5$ and the following debate about the physical mechanism at their origin. However, the transport anomalies are not limited to the resistivity, the out-of-plane magnetoresistivity and the thermopower.

Recently, *Li et al.* have investigated the dependence between the magnetoresistance (MR) and the angle between the applied magnetic

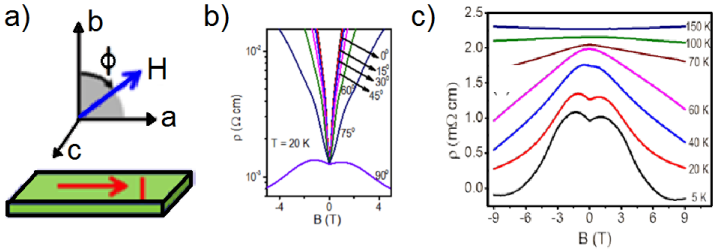

Figure 1.12: (a) The geometry used for the measurements of the MR. a, b and c are the crystal axis, H is the applied magnetic field, I is the current across the sample and Φ is the angle between H and I. (b) MR of $ZrTe_5$ changing the angle between the applied magnetic field and the surface of the sample and (c) in-plane magneto-resistance ($\Phi = 90^o$) of $ZrTe_5$ for different temperatures [16].

field H and the current I, flowing along the a axis, as shown in figure 1.12 (a) [16]. When changing the angle with the sample kept at 20 K, passing from a perpendicular magnetic field position to a parallel position, the MR decreases and becomes negative, as shown in figure 1.12 (b). This negative value reverts its sign increasing the temperature of the sample from 20 K to 150 K, as shown in figure 1.12 (c).

Li et al. have interpretated the negative MR as indication of a chiral magnetic effect (CME), a physical effect that manifests only in the case of the presence of 3D Dirac particles. These authors conclude that such a CME calls for an interpretation of $ZrTe_5$ as a 3D TSM [16].

The CME consists in the generation of an electric current, the chiral magnetic current, induced by *Weyl fermions* [76]. The Dirac point in a 3D TSM is composed of two overlapping *Weyl nodes* with opposite chirality, which can be separated in momentum space by breaking the time-reversal symmetry or the spatial inversion symmetry [77]. As a consequence of this symmetry breaking, the charges at the two momentum-splitted Weyl nodes have opposite chirality. In the presence of parallel magnetic and electric fields, the Weyl fermions are transferred to another Weyl node with opposite chirality, resulting in

the observed negative MR [78]. The CME is a macroscopic quantum phenomenon present in systems with charged chiral fermions, such as Dirac semimetals, like Cd_3AS_2 and Na_3Bi [75, 79–81].

The debate regarding the reliability of the negative MR as a fingerprint of a 3D TSM physics is already open with conflicting points of view.

Recently *Arnold et al.* reported a study on the bulk FS topology of the Weyl semimetal TaP [82]. By combined quantum oscillation studies and band structure calculations, it has been shown that E_F is well outside the range for observing chiral Weyl fermions. Therefore, FS consists only of topologically trivial pockets. However, the negative MR effect survives even when the chirality of the system is not well-defined.

In Ref. [83], experimental evidences about the not total reliability of chiral anomalies as fingerprint of 3D TSM are shown. This study demonstrates, indeed, that measurement of the longitudinal MR in materials with field-induced resistance anisotropy is not straightforward. Furthermore, they suggest a careful checking before intrinsic physical properties of the material, such as the chiral anomaly in Weyl semimetals, are extracted.

Moreover, 3D TSM are not the only topological materials showing a negative MR. *Banerjee et al.* have reported negative MR in the topological insulator $BiSbTeSe_2$. Here, the negative MR originates from an increase in the density of defect states. However, the presence of defects leaves the surface states unaffected, conserving the non-trivial topological character of the material [84].

1.4.5 The Predicted Topological Phase Transition. Theory and Experiments.

Besides the proposed 3D TSM ground state, the interest on $ZrTe_5$ has grown, in the last years, thanks to the theoretical work reported in Ref. [14]. The single layer of $ZrTe_5$ has been computed to be a QSHI, presenting spin polarized states at the edges. In the work of *Weng et al.* it is also discussed how, by stacking different layers of

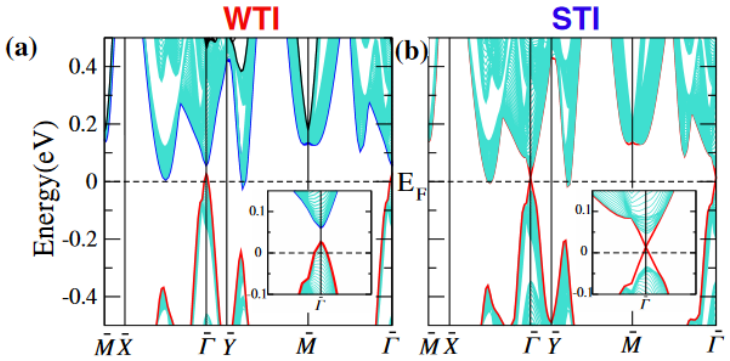

Figure 1.13: (a) The calculated band structures and surface states for the top surface. The weak TI (WTI) solutions (panel (a)) has been obtained by using optimized lattice parameters, while the strong TI (STI) solution (panel (b)) has been calculated from the experimental ones. Adapted from [14].

$ZrTe_5$, it is possible to obtain a bulk material which, depending on the stacking lattice distance, lies in proximity of a topological phase transition between STI and WTI. The calculated band structures for different lattice parameters are shown in Fig. 1.13. On the left panel, figure 1.13 (a), the calculated electronic band structures at the top surface for the WTI case, while on the right panel, figure 1.13 (b), the STI case is shown. The phase transition from STI to WTI takes place at the Γ point. Noticebly, the WTI case has been obtained using optimized lattice parameters, while the strong TI (STI) phase has been calculated from the experimental ones.

The work of *Weng et al.* has been recently supported by another theoretical work. *Fan et al.* have found a clear topological transition between a STI and WTI in $ZrTe_5$, accompanied by a Dirac semi-metal phase between them [15].

Many experimental works have tried to confirm the prediction of Ref. [14]. Nonetheless, the experiments show conflicting results which make challenging to determine univocally the topological phase of

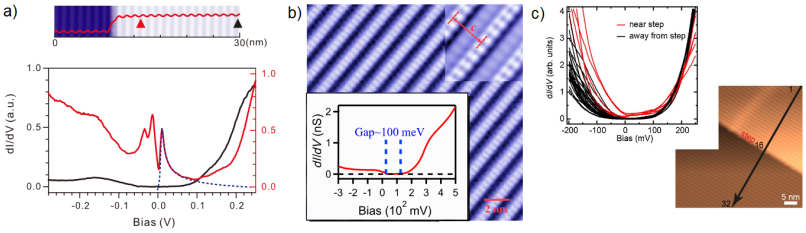

Figure 1.14: (a) Two spectra extracted from the STM figure at the top at the positions marked by black and red triangles. The dotted blue line is the fitting results with a 1D density of states exhibiting the inverse-square-root singularity. Taken from [22]. (b) STM constant current topographic image of the cleaved a-c (010) surface of $ZrTe_5$ crystal. Right top inset: High-resolution topography showing the details of the surface structure. Bottom left inset: Tunneling differential conductance spectrum on the a-c surface showing a large energy gap of $\sim$ 100 meV above E_F with zero conductance inside the gap. Taken from [17]. (c) STM/STS measurements on the pristine $ZrTe_5$. STM topography image with a step and in the inset the dI/dV curves collected along the solid black arrow [23].

$ZrTe_5$.

The main experimental results obtained on $ZrTe_5$ with scanning tunneling microscopy and spectroscopy (STM and STS) are summarized in figure 1.14.

(a) The STM and STS experiment performed by *Li et al.* shows a gap of $\sim$ 80 meV [22]. The measurements were carried out with a current $I = 500$ pA and a voltage $V = 500$ mV. Moreover, they have reported also the presence of a metallic edge state at the step edge, as shown in figure 1.14(a). The metallic edge state at the step edge and the gap at the surface were interpreted as fingerprints of the WTI phase.

(b) *Wu et al.* have also performed a STM and STS experiment, estimating a gap of $\sim$ 100 meV [17]. Their results are reported in figure 1.14 (b). The differential conductance map was collected

with $I = 200$ pA and $V = 250$ mV. They have interpreted their results as the indication that $ZrTe_5$ is a WTI.

(c) In the work of *Shen et al.*, STM and STS data collected on $ZrTe_5$ are reported [23]. These data were obtained with $V = -1.6$ V and $I = 100$ pA. The STM measurements show a V-shaped total density of states near E_F, thus suggesting a gapless nature of the electronic structure of $ZrTe_5$. The authors have left open the interpretation of their results: the gapless nature of the electronic structure of $ZrTe_5$ can be either the indication that the material is a 3D TSM rather than a STI. Their results are reported in figure 1.14 (c).

In order to understand the topological character of $ZrTe_5$, also ARPES experiments were performed and the results were often shown as complemental to STM and STS data. Figure 1.15 summarizes the main ARPES results on $ZrTe_5$.

(a) *Li et al.*, in their ARPES and magneto-transport study, conclude that $ZrTe_5$ is a 3D TSM [16]. However, *"because the Dirac point is unoccupied, the ARPES studies cannot provide a complete picture of the electronic structure in its vicinity, and the existence of a small mass gap cannot be excluded".* The measured band structure along the $\Gamma - X$ direction is shown on figure 1.15 (a).

(b) The problem of the unoccupied Dirac point was faced by *Wu et al.* by means of sustitutional doping of the material [17]. In figure 1.15 (b) the ARPES spectrum collected, along the $\Gamma - X$ direction on f $Zr_{0.9975}Ta_{0.0025}$ is shown. As reported also before, the conclusion of this work is that $ZrTe_5$ is a WTI.

(c) A substitutionally doped $ZrTe_5$ sample was measured also by *Shen et al.* [23]. In figure 1.15 (c) the ARPES data obtained measuring $Ta_{0.12}Zr_{0.88}Te_5$ are shown . As previously discussed, they conclude their work leaving open the possibility that the material could be either a STI rather than a 3D TSM.

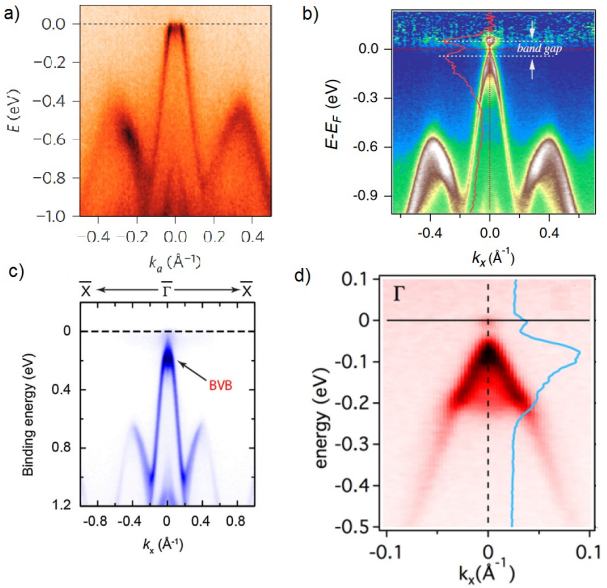

Figure 1.15: (a) ARPES image of $ZrTe_5$. Measurement taken along Γ-X. Adapted from [16]. (b) ARPES image of $Zr_{0.9975}Ta_{0.0025}Te_5$ along Γ-X, divided by the FD distribution function (T= 190 K) convoluted with the energy resolution Gaussian function. Adapted from [17]. (c) ARPES image of $ZrTe_5$. Measurement taken along Γ-X. Adapted from [23]. (d)ARPES image of $ZrTe_5$ after deposition of Rb. Measurement taken along Γ-X. Adapted from [19].

(d) Last but not least, the ARPES work of *Moreschini et al.* shows data collected on $ZrTe_5$ after Rb deposition [19]. In figure 1.15 (d) one of their ARPES images is reported. A gap at the Γ point was detected and the authors' interpretation is that $ZrTe_5$ is a WTI.

Optical studies, with and without the application of a magnetic field, were also performed in order to clarify the topological character of $ZrTe_5$ [20, 21].

(a) Infrared reflectivity measurements were used in order to derive the optical conductivity of $ZrTe_5$. It was observed that the optical conductivity increases linearly with frequency below normal interband transitions, which provides optical spectroscopic proof of a 3D Dirac semimetal [20].

(b) Magnetoinfrared measurements have shown a transitions between Landau levels and their further splitting under a magnetic field. Both the sequence of transitions and their field dependence follow quantitatively the relation expected for 3D massless Dirac fermions [21].

2 Experimental Techniques

2.1 Angle Resolved Photoelectron Spectroscopy (ARPES)

2.1.1 Photoelectric Effect

Electrons have been used as a tool for the investigation of matter since many decades. In some experiments, for example in the case of Low-Energy Electron Diffraction (LEED), they are used to probe the atomic and molecular crystal structure and their orders [85]. In other experiments, electrons are observed in collision processes and they carry information on the atomic environment and the scattering process. In general, an electron spectroscopy consists in detecting and analysing scattered or emitted electrons looking at their energy, momentum, spin. What makes electrons successful as a probing tool is not only their strong interaction with matter, but also the fact that, experimentally, they are easy to handle and to detect. In fact, simple electronic lenses and deflection systems can be employed to determine their angular and energy distribution.

Photoemission spectroscopy (PES), or photoelectron spectroscopy,

is a method to study the electronic structure of atoms, molecules, solids and adsorbates [86]. The term photoemission spectroscopy usually refers to a wide set of experimental techniques based on the application of the *photoelectric effect*. This effect was first detected by Hertz in 1887 when he reported about the observation of an electric discharge between two polarized elecrodes if the cathode was illuminated by ultraviolet (UV) light [87]. A consistent interpretation of this phenomenon was given by Einstein [88] in 1905 adopting a quantized model for the light-matter interaction. For this reason, Einstein was awarded the Nobel Prize in Physics in 1921 [46].

In the modern view, PES can be described as a *photon in - electron out* process. Angle-resolved photoemission spectroscopy (ARPES) constitutes one of the recent technical development of PES allowing to measure the kinetic energy and the angular distribution of the electrons photoemitted from a sample illuminated with a quasi-monochromatic radiation at a frequency larger than its ionization potential. In this way, informations on both the energy and momentum of the electrons photoemitted from the material under study can be achieved.

2.1.2 Conservation Laws

By measuring the kinetic energy and the emission angle of the photoelectrons, the binding energy and the momentum inside the crystal can be univocally retrieved thanks to the conservation laws of the photoemission process. Assuming the simple case of a metal, where the sample is illuminated by a monochromatic photon source with photon energy $h\nu \geq \Phi$, being Φ (typically $\Phi \simeq 4.5$ eV) the *workfunction* [89]. The *binding energy*, E_{Bin}, of the electron inside the material can be obtained by the energy conservation law:

$$E_{kin} = h\nu - \Phi - E_{Bin}. \tag{2.1}$$

Since the electron conserves his momentum parallel to the surface when escaping the surface, two components, k_x and k_y, can be determ-

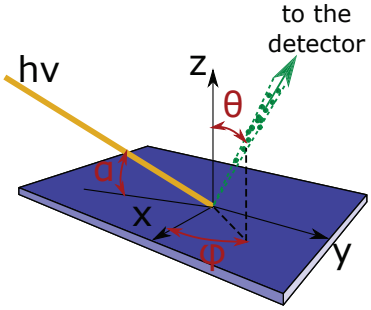

Figure 2.1: Typical geometry of an experimental ARPES setup. In red the polar angle θ, the azimuthal angle ϕ and the angle of incidence α.

ined from the following relations:

$$k_x = \frac{1}{\hbar}\sqrt{2mE_{kin}}sin\theta cos\phi \tag{2.2}$$

$$k_y = \frac{1}{\hbar}\sqrt{2mE_{kin}}sin\theta sin\phi \tag{2.3}$$

where θ and Φ are determined by the crystal and experimental geometry [89], as shown in figure 2.1.

The evolution of the detected electronic density of states while varying the photon energy reflects the dispersion along the k_z direction of the Brillouin zone. k_z can be obtained from the following relation

$$k_z = \frac{1}{\hbar}\sqrt{2m(E_{kin}cos^2\theta + V_0)} \tag{2.4}$$

where V_0 is the *inner potential*. V_0 can be determined experimentally, with some approximation, by observing the periodicity of the k_z dispersion itself.

Of course, the equations above are exact for data acquired with low photon energy, i.e. when the momentum transferred by the photon is negligible. As shown by the yellow line of figure 2.2, the tranferred photon momentum can be neglected at low photon energies, i.e. in the ultra violet (UV) range with $h\nu < 100$ eV. When the photon energy

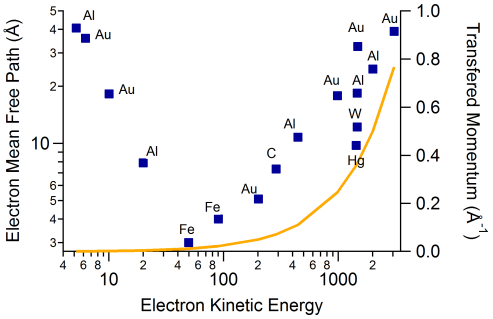

Figure 2.2: Electron mean free path (blu markers) and momentum transferred by the photon computed for $\theta_x = 0°$ (yellow line) versus electron kinetic energy. Adapted from [86].

reaches the soft x-ray (SX) regime the transferred photon momentum cannot be neglected anymore and the equations 1.2-1.4 must include an additional term to account for the photon transferred momentum:

$$k_x = \frac{1}{\hbar}\sqrt{2\ m\ (E_{kin})}\ \sin\theta\cos\phi - \frac{2\pi\nu}{c}\cos(\alpha+\theta) \tag{2.5}$$

$$k_y = \frac{1}{\hbar}\sqrt{2\ m\ (E_{kin})}\ \sin\theta\sin\phi + \frac{2\pi\nu}{c}\sin(\alpha+\theta)\ sin\phi \tag{2.6}$$

$$k_z = \frac{1}{\hbar}\sqrt{2\ m\ (E_{kin}\ \cos^2\theta + V_0)} + \frac{2\pi\nu}{c}\sin(\alpha+\theta) \tag{2.7}$$

where α represents the angle of incidence of the photon beam with respect to the sample surface, as defined in figure 2.1.

2.1.3 3-Step Model and Photoemission Intensity

The photoemission process can be theoretically described in two different ways: the so-called *one step model* or the *three step model*.

The one-step model is the most rigorous approach. It consists in the description of the whole photoemission process in terms of a single coherent process [89,90,95–97]. However, due to the complexity of the

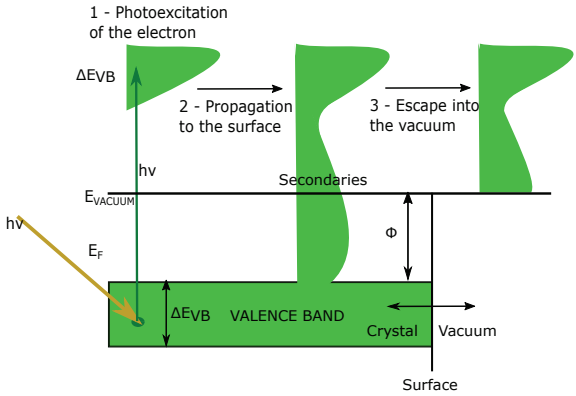

Figure 2.3: A scheme representing the three-step model. Adapted from [86].

one-step model, photoemission data are usually discussed within the three-step model, which is a phenomenological model.

Within the three-step model, schematized in figure 2.3, the photoemission process is divided into three independent steps [97–99]:

1. Excitation of the electron in the solid after the interaction with the photon.

2. Propagation of the excited electron to the surface, with the generation of secondary electrons given by the interaction with atoms or electrons and

3. Escape of the photoelectron into the vacuum after the transmission through the surface potential.

In order to to deduce the electronic structure of a solid from photoelectrons, the *sudden approximation* should be satisfied [86,89,100]. This approximation consists in the assumption that the time taken by the photoelectrons to travel from the bulk to the vacuum is much shorter than the recovery time of the transient electronic system after having emitted electrons. The interactions between the photoelectrons and the ionized solid are also not considered. When this condition is

met, the emitted photoelectrons carry the information of the ground state electronic structure of the probed solid.

The electron system is usually described by the Green's function formalism $G(k,\omega)$ [91–94]. Its imaginary part is called single particle spectral function,

$$A(k,\omega) = -\frac{1}{\pi} ImG(k,\omega) \tag{2.8}$$

where the item $k = k_{//}$ is the in-plane momentum component and ω is the energy related to the Fermi level.

The photoemission intensity can be written as a function of the energy and of the momentum of the electrons

$$I(k,\omega) = I_0(k,\nu,A) f(\omega) A(k,\omega) \tag{2.9}$$

where:

- $I_0(k,\nu,A) \propto |M^k_{f,i}|^2$ which is the *matrix element* [86, 89, 100]. This quantity is related to the photon energy, photon polarization and experimental geometry. The matrix element may even bring to a complete suppression of the photoemission intensity [101, 102].
- $f(\omega) = (e^{\omega k_B T}+1)^{-1}$ is the Fermi-Dirac distribution, since direct photoemission probes only the occupied electronic states.
- $A(k,\omega) = A^-(k,\omega)+A^+(k,\omega)$ is the single particle spectral function, given by the sum of the one-electron removal and addition spectra which one can probe with direct and inverse photoemission, respectively [89].

The second step consists in the propagation, after the excitation, of the electron through the solid to the surface. An important quantity that helps to understand the consequences of this motion inside the bulk, is the *electron mean free path*. This quantity characterizes the average distance travelled by a photoelectron inside the solid without undergoing any scattering event (these electrons are defined *primary photoelectrons*), and it determines the thickness of the sample from

which the primary photoelectrons originate. Figure 2.2 shows the estimated electron mean free path for selected materials, as a function of the electron kinetic energy [86].

The minimum of the electron mean free path is found at about 50 eV of electron kinetic energy, where the electron mean free path is expected to be of the order of few angstroms. Therefore, conventional Extreme Ultraviolet (EUV) light sources, such as He discharge lamp characterized by two emission lines at 21.22 eV and at 40.81 eV, are quite surface sensitive. A more bulk sensitive PES is obtained when the photoelectron kinetic energy is indicatively larger than few hundreds of eV. However such model is not universal and for each material the escape depth must be calculated on the base of appropriate scattering calculations.

For very low photon energy sources, like the fourth-harmonics of table-top Ti:Sapphire laser sources at about $h\nu \simeq 6.2$ eV, the result is more debated [86, 103–106]. The mean free path of photoelectrons can be of the order of ~ 30 Å, as shown in figure 2.2. Although other recent works have estimated the electron mean free path at low energy as $\sim 7 \pm 2$ Å [106]. This last result [105, 106] suggests that, for a practical use of low energy PES as a bulk-sensitive technique, the real sample properties have to be taken into account. In particular, care should be exerted since a different probing depth may not be the only origin for changes of the spectral intensity as the photon energy is varied. The variation of the photoemission matrix element versus the photon energy in the low-energy regime is not well known and often just ignored. Moreover, the presence of small defects or valleys at the surface can have a major effect in the photoemission process with low-photon energy sources.

In the next chapters, we will show several datasets taken with different photon energies and the consequences will be deeply analyzed.

2.1.4 Ultra High Vacuum and Hemispherical Electron Energy Analyzers

We have explained how the electrons are photoemitted from the material, the laws governing this process and the choice of the optimal photon energy when a more bulk or surface sensitive experiment is required. Before the photoelectron reaches the detector, it has to travel, as shown in figure 2.1, for a relatively significant distance. Since we are interested to study primary electrons, generated by non contaminated materials, spurious and surface contaminants must be avoided. This can happen only if the entire system is kept in ultra high vacuum (UHV) conditions.

The UHV condition is a necessary requirement to allow that the maximum number of primary photoelectrons reaches the detector since free electrons are strongly absorbed or scattered by gases. UHV is necessary also for ensuring the purity of the probed crystal over a long time interval. Sample surface deterioration, caused by the absorption of contaminants, can in fact completely hamper the results of ARPES or PES experiments.

The UHV regime is normally characterized by a pressure between 10^{-9} $mbar$ and 10^{-11} $mbar$. In the ARPES setups used during the measurements presented in this thesis, the pressure was always $< 2 \times 10^{-10}$ $mbar$. The samples were cleaved *in situ* at room temperature at a pressure $\sim 5 \times 10^{-10}$ $mbar$.

ARPES was strongly developed after the advent of two-dimensional detectors. These type of detectors are able to performing simultaneously the energetic and angular distributions of the photoelectrons emitted from the sample. Such measurement is typically achieved by a hemispherical electron analyser, where the photoelectrons are deflected by the electric field created between the outer and inner hemispherical capacitor plates.

The trajectory of the photoelectrons inside the electron analyzer, shown in figure 2.4, can be decomposed in two perpendicular components. The first contains the angular dispersion information and it is controlled by the entrance slit width. The second brings the inform-

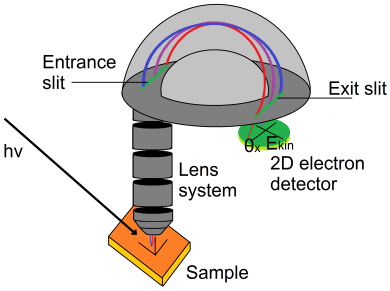

Figure 2.4: A scheme of a hemispherical electron analyzer.

ation about the energy dispersion. A set of electrostatic lenses are set between the sample and the entrance slit of the energy analyser in order to collect and retard/accelerate the photoelectrons before the entrance slit to match a special selected energy known as *pass energy* (E_P). This is the energy which characterizes the central circular trajectory inside the hemispherical capacitors. The angular dispersion of the electron analyser will also be controlled by these electrostatic lenses. The two-dimensional detector set after the exit slit of the hemisphere allows the collection of ARPES images (E_{kin} vs θ). Because of the above arguments, one axis is associated to the angular dispersion and the second is associated to the kinetic energy.

2.1.5 Time Resolved ARPES

The investigation of the time-dependent electronic structure is made possible by the development of time-resolved ARPES (Tr-ARPES). This technique has become quite important in the last years thanks to many successful experiments done on superconductors [107, 108], graphene [109,110], charge density wave materials [111] and topological insulators [112–116].

The main advantages of Tr-ARPES, with respect to conventional ARPES, are:

- The possibility to transiently populate the empty states of a material, observing states not detectable with conventional ARPES.

- The possibility to study the excitation or relaxation time of a material, disentangling different processes (each of which acts with a peculiar time scale) that coexist at the equilibrium in the same energy scale.

Tr-ARPES is based on the pump-probe approach, which exploits two synchronized and delay controlled pulses, called *pump* and *probe* beams. The pump beam excites the sample into a non-equilibrium condition, while the probe beam is used to measure, as a function of the time delay from the pump pulse arrival, the effect induced by the excitation. The delay control between the two pulses is obtained by introducing a relative difference in the pump-probe optical paths.

The time-resolved experiments have been made possible by the advent of pulsed laser sources able to produce ultrashort laser pulses ($<$ 100 fs), typically in the near-IR region. In a pump-probe experiment, the pump beam is often the fundamental emission of the laser source, while different probe beams can be obtained by non-linear optical processes, such as the generation of harmonics in crystals [117, 118] or in gas [119, 120]. Two important parameters of the laser source are the pulse photon energy and the repetition rate, defined as the number of pulses per unit of time.

2.1.6 The T-ReX Laboratory at Elettra

The T-ReX laboratory is equipped with a state of the art Specs Phoibos 225 hemispherical analyzer, mounted with the entrance slit oriented horizontally. The sample under scrutiny is transferred on a vertical six degrees of freedom precision manipulator with He-cryostat, allowing for minimum sample temperature of $\sim$ 30 K. Atomically clean sample surfaces can be obtained via sputtering-annealing cycles (for metallic single crystals) or by in-situ cleavage. Sample alignment and surface quality can be routinely verified by means of low energy electron diffraction (LEED) technique.

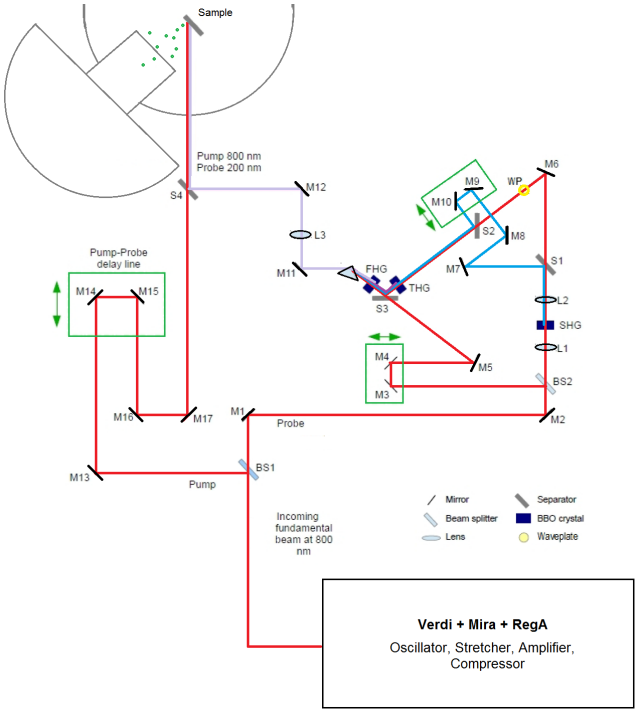

Figure 2.5: A sketch of the experimental setup of the T-Rex laboratory in Trieste.

A scheme of the Tr-ARPES experimental setup of the T-Rex laboratory is shown in figure 2.5. A *Coherent Mira oscillator*, in which the active medium is a Ti:Sapphire crystal (Titanium doped Al_2O_3), is pumped by a *Coherent Verdi V18* solid state laser. The stretched pulses produced by the oscillator are amplified in a regenerative amplifier (*Coherent RegA 9050*) and then compressed. The typical repetition rate of the source is 250 kHz and the output pulses have a temporal duration of approximately ~ 60 fs with a spectrum centered at 800 nm, corresponding to ~ 1.55 eV. The fourth harmonics of the

fundamental of the laser is used as probe for the photoemission experiments. The photon energy must be higher than the work function Φ of the material: the fourth harmonics (~ 6.2 eV) is the lowest harmonics that satisfies this requirement. To obtain ultrashort fourth harmonics pulses, the Sum Frequency Generation in phase-matched BBO crystals is used. The generation scheme is reported in figure 2.5, and exploits three steps of frequency mixing. Before reaching the experimental chamber, the pump and the probe are recombined in a collinear geometry, to ensure a good spatial overlap.

The spectrum of the probe pulse was measured by a high resolution single-grating monochromator, having a target resolution of 0.08 nm. It is characterized by a central wavelength $\lambda = 196.80$ nm, with $\Delta\lambda = 0.59$ nm FWHM [121]. Hence, the photon energy is $E_{IV} = 6.2$ eV. $\Delta\lambda$ corresponds to $\Delta E_{IV} = 18$ meV, which sets the energy resolution in ARPES experiments. The temporal duration of the fourth harmonic pulse was characterized by performing a cross-correlation measurement between the fourth harmonic and the fundamental pulses, by recording their difference frequency (third harmonic) [121]. The fourth harmonic FWHM is calculated by deconvolving the pump FWHM from the cross-correlation FWHM, and results ~ 250 fs. This value determines the temporal resolution in Tr-ARPES experiments, i.e. the fastest dynamics that can be resolved in a measurement. The pump and probe spot sizes have been routinely characterized via the knife-edge technique, and resulted of the order 180 ± 10 μm and 150 ± 10 μm respectively. In the experiments reported in Chapters 3 and 4, the p-polarized pump beam excites the $ZrTe_5$ samples with an impinging fluence ~ 100 μJ/ cm^2, except for the study of the fluence dependence of the pump probe dynamics in which the fluence was varied from ~ 20 μJ/ cm^2 to ~ 400 μJ/cm^2.

2.1.7 Geometry of the ADRESS Beamline at SLS and of the APE Beamline at Elettra

Measurements at the ADRESS beamline, operating at the Swiss Light Source (SLS) storage ring, were performed in the energy range 310 –

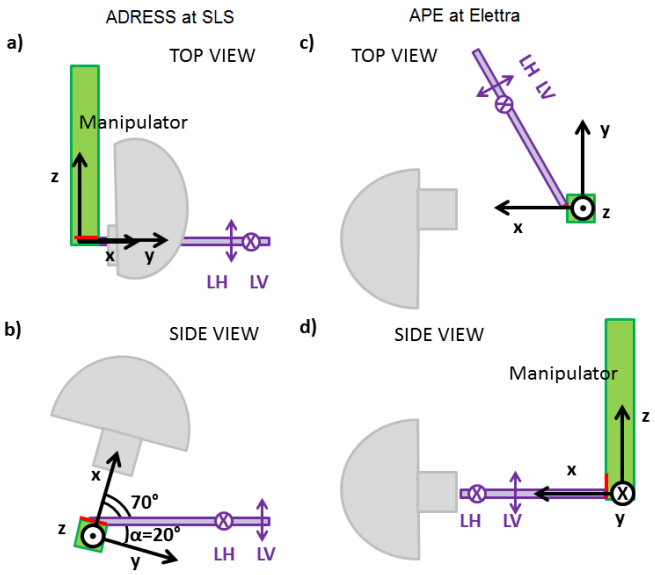

Figure 2.6: A comparison of the geometry of the APE and ADRESS end stations. In green the manipulator, in violet the incoming beam trajectory and polarization, in grey the analyzer and in red the sample. ADRESS (SLS synchrotron) beamline geometry, Top view (a) and Side view (b). APE (Elettra synchrotron) beamline geometry, (c) Top View and (d) Side view.

510 eV, with an overall energy and angular resolution between 60 and 70 meV and 0.07°, respectively. The photon energy dependence of the measured ARPES images was investigated for both horizontal (LH) and vertical (LV) linear polarizations. The concepts and technical realization of the high-resolution soft X-ray ADRESS beamline operating in the energy range from 300 to 1600 eV and intended for resonant inelastic X-ray scattering (RIXS) and angle-resolved photoelectron spectroscopy (ARPES) are described in Ref. [122]. Figure 2.6 (a-b) shows the top and side view of the beamline. The manipulator, oriented along the z direction, lies perpendicular to the photon beam direction. The sample surface, when mounted on the manipulator,

forms an angle of 20° with the photon beam. The analyzer is above the photon beam, along the x direction and it forms an angle of 70° with the photon beam. The slit of the analyzer is oriented along the y direction.

During the experiments at the ADRESS beamline, reported in Chapter 5, the sample was aligned with the a vector along the y direction of the manipulator and the b vector along the x direction. In this configuration, the LH polarization measures odd states, because the electric field is oscillating in the direction orthogonal to the sample symmetry plane. In contrast, being the electric field oscillating in the sample symmetry plane for LV polarization, even states are observed in this geometry.

Measurements at the APE beamline, operating at Elettra storage ring, were performed in the energy range between 20 and 36 eV, with energy and angular resolution better than 20 meV and 0.1°, respectively. The geometry and the main characteristics of the APE beamline, composed by a fully independent double branch scheme obtained by the use of chicane undulators and able to keep polarization control in both linear and circular mode, are described in Ref. [123].

This beamline, which top and side view are shown in figure 2.6 (c) and 2.6 (d), respectively, has the manipulator along the z direction. The analyzer focus is along the x direction, with the slit oriented along the z direction.

During the experiments on APE, reported in Chapter 3 and Chapter 5, the sample was oriented with its chain direction a along the z axis of the manipulator. In this configuration, the used LH polarization has non zero projections both parallel and orthogonal to the material symmetry plane.

Unfortunately, being the parity undefined in this particular geometry we cannot infer about the symmetries of the probed states.

2.1.8 Spin Resolved ARPES

Spin Resolved ARPES measurements were performed at the APE beamline using a *very low energy electron diffraction* (VLEED) de-

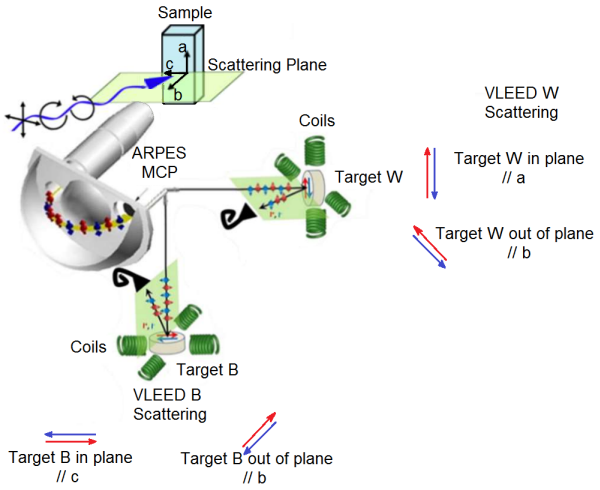

Figure 2.7: Experimental geometry scheme. Polarized monochromatic synchrotron radiation is travelling at 45° with respect to the analyser lens axis, in the horizontal plane of the storage ring while the analyser slit is perpendicular to it. The two VLEED targets cover all the three directions of the sample geometry. Black *VLEED measures the spin polarizations parallel to the c and b directions, while* white *VLEED measures the spin polarizations parallel to the a and b directions. Figure adapted from Ref. [124].*

tector. This spin filter allows a potential hundred-fold higher sensitivity with respect to the Mott polarimeters. The spin-ARPES setup is implemented in the low energy (LE) branch at APE, which operates between 8 eV and 120 eV.

The spin detector used at APE is based on pure oxide Fe(001) surface, grown atomically ordered, hence minimizing spurious electron diffusion effects originating from defects and impurities. The target, in this setup, is a ferromagnet with single domain orientation in the remanent magnetization state. The magnetization of the target can be easily switched between orthogonal directions in order to probe two in plane components of the spin polarization vector.

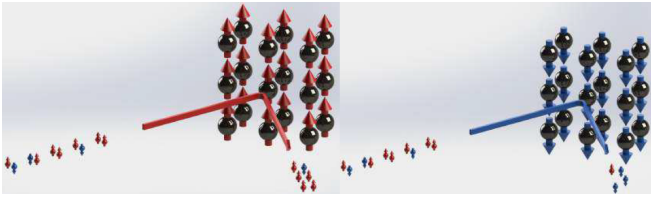

Figure 2.8: Cartoon of the exchange scattering mechanism: if the target is magnetized with its spin pointing up, the reflected electrons will be mostly spin up (top panel). Reversing the target magnetization causes spin down electrons are mainly reflected (bottom panel). If the primary beam is polarized, then a non-zero asymmetry value will be measured.

Two independent VLEED detectors (*black* and *white* detectors) form the whole 3D vectorial spin polarimeter by matching one component, as shown in figure 2.7. The arranged geometry ensures that the *white* VLEED polarimeter measures the spin component aligned parallel to the analyser slit, a and the component perpendicular both to the analyser slit and to the sample surface, b. The second polarimeter, *black* VLEED, measures the spin polarization components along the direction parallel to the sample surface and perpendicular to the slit, b, and the same out-of-plane component, b that is redundant with the identical measurement by VLEED-W. The possibility to measure the same b polarization component with both *white* and *black* polarimeters (i.e. with two different targets) allows to cross-normalize the data.

When the target is magnetized, its electronic bands are split determining a scattering spin asymmetry. The resulting experiment is shown in the cartoon of figure 2.8. If the target is magnetized with its spin pointing up, the reflected electrons will be mostly spin up. Reversing the target magnetization causes that spin down electrons are mainly reflected. If the primary beam is polarized, then a non-zero asymmetry value will be measured [124].

For every point in the (k_x, k_y) space that has to be measured, it is necessary to measure the intensity detected by the target, changing its magnetization, m. Then, it is easy to calculate the resulting

asymmetry:

$$A = \frac{I_{m+} - I_{m-}}{I_{m+} + I_{m-}} \tag{2.10}$$

from which one can deduce also the polarization

$$Pol = \frac{1}{S} A \tag{2.11}$$

where S is the *Sherman function*, which is a characteristic of the target. Before our experiments on $ZrTe_5$, the detector has been calibrated by measuring the Rashba-split surface states of Au(111), as a spin polarization standard [125]. The Sherman function of the setup was fixed to $S \sim 0.3$. At this point, the spin up and down components of the signal can be written as

$$S_{up} = (1 + Pol) \times (I_{m+} + I_{m-}) \tag{2.12}$$

$$S_{down} = (1 - Pol) \times (I_{m+} + I_{m-}). \tag{2.13}$$

2.2 X-Ray Diffraction (XRD)

2.2.1 Why XRD?

X-rays are an invaluable probe of the structure of matter and the range of problems where X-rays have proved to be decisive in unravelling a material structure is very wide. In particular, in recent years X-ray diffraction (XRD) has become an increasingly important technique for qualitative and quantitative analyses as well as for fundamental studies of the properties and structure of crystals and polymers [126–128].

Crystals are regular arrays of atoms and X-rays are highly energetic waves of electromagnetic radiation. Atoms scatter X-ray waves producing secondary spherical waves. This phenomenon is known as elastic scattering and the atom is called scatterer. A regular array of scatterers produces a regular array of spherical waves. Although these waves cancel one another out in most directions through destructive interference, they add constructively in a few specific directions, determined by Bragg's law [129]:

$$2dsin\theta = n\lambda \tag{2.14}$$

here d is the spacing between diffracting planes, θ is the incident angle, n is any integer and λ is the wavelength of the beam. These specific directions appear as spots on the diffraction pattern called reflections.

In principle, any wave impinging on a regular array of scatterers produces diffraction. However, to produce significant diffraction, the spacing between the scatterers and the wavelength of the impinging wave should be similar. X-rays are used to produce the diffraction pattern and to study the crystal structure because their wavelength, λ, is typically of the same order of magnitude as the spacing d between crystal planes ($1 - 100$ Å, corresponding to a photon energy of $12.4 - 0.124$ keV).

The power of this technique is that it can be used not only in presence of a sample composed by a single crystal, but it can be used also with poly-crystals or powders. Figure 2.9 shows a typical XRD pattern collected from a powder (panel (a)) and from a single crystal

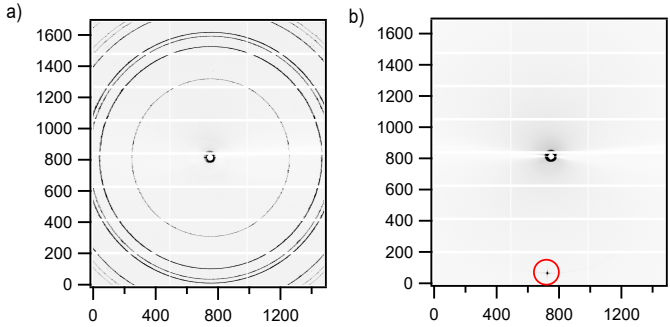

Figure 2.9: XRD measurements taken on (a) powders of AgBeh, used as calibrant, and on (b) a single crystal of $ZrTe_5$. The reported data are espressed in pixel of the detector.

(panel (b)). In particular, the ordered atoms of the single crystal produce single peaks while poly-crystals or powders produces diffracted radiation in many directions giving the classical ring-pattern.

2.2.2 The XRD1 Beamline

The X-Ray Diffraction 1 (XRD1) beamline, operating at the Elettra storage ring, was designed (in collaboration with the Istituto di Cristallografia - CNR) primarily for macromolecular crystallography, but the characteristics of the beamline allows to perform a wide variety of experiments such as small molecules, protein crystallography, powder diffraction, high pressure physics and solid-state experiments.

The XRD experiment reported in this thesis was performed at a wavelenght of 1.4 Å, i.e. ~ 8.86 keV. The diffractometer was calibrated using *silver behanate* (AgBeh) powders (figure 2.9 (a)). The sample was mounted on a 4 degrees of freedom manipulator and cooled by a liquit nitrogen jet.

3

The Temperature Dependence of the $ZrTe_5$ Band Structure

In this chapter, we investigate by ARPES experiments the effect of the temperature on the electronic band structure of $ZrTe_5$. The ultimate goal of this study is to find an explanation for the anomalous transport properties reported for this material.

In the first part of this chapter the ARPES data, measured at 16 K, are reported and discussed. In the following sections, ARPES data collected at different temperatures and with different photon energies are analyzed and compared. Finally, a brief discussion aimed to find a clue between the rigid shift of the electronic band structure revealed by ARPES and the anomalies in the transport properties of $ZrTe_5$ is reported.

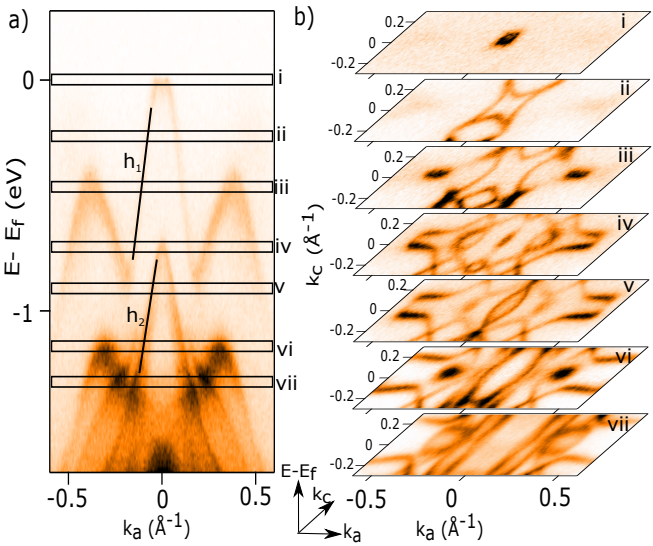

Figure 3.1: (a) Electronic band structure of $ZrTe_5$ along the k_a direction measured at 16 K with photon energy of 22 eV. The black lines, h_1 and h_2, indicate two bands dispersing with similar group velocity: $V_{h_1} = 8 \pm 1 \times 10^5$ m/s and $V_{h_2} = 7 \pm 1 \times 10^5$ m/s. (b) Constant Energy maps obtained by integrating 45 meV around (i) E_F, (ii) -0.24 eV, (iii) -0.46 eV, (iv) -0.72 eV, (v) -0.88 eV, (vi) 1.15 eV and (vii) -1.30 eV.

3.1 Electronic Band Structure at Low Temperature

High resolution ARPES measurements collected along the k_a direction are shown in figure 3.1 (a). This dataset were collected at the APE beamline with 22 eV photon energy and holding the sample at 16 K. Different constant energy maps in the (k_a, k_c) plane obtained by integrating over ~ 45 meV at selected binding energies are reported in figure 3.1 (b).

The $ZrTe_5$ Fermi surface (FS) is shown in panel (b-i). The hole-like

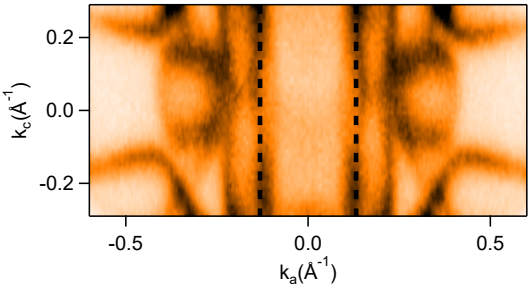

Figure 3.2: Constant Energy map obtained by integrating data on a ~ 45 *meV window at* -1.30 *eV. A black dashed line indicates the evolution of the* h_1 *state.*

state h_1 forms a circular pocket at E_F, and its evolution is tracked in figure 3.1 (b-i) - (b-iv). The pocket changes from a circle to a warped rectangle (b-i) - (b-ii), then it evolves in a more complex shape (figure 3.1 (b-iii)-(b-iv)).

Figure 3.1 (a) reveals a second band, h_2, dispersing with similar group velocity of h_1 and appearing at a higher binding energy. This band has the maximum located at $k_a = k_c \simeq 0$ Å^{-1} and binding energy ~ -0.72 eV. The bands velocities V_{h_1} and V_{h_2} have been estimated to be $(8 \pm 1) \times 10^5$ m/s and $(7 \pm 1) \times 10^5$ m/s, respectively.

The different trend displayed by the h_1 and h_2 bands in the constant energy maps (CEMs) of figure 3.1 (b) confutes the possibility that could have been suggested by the similarity of V_{h_1} and V_{h_2}: the band h_2 might be a higher binding energy replica of h_1, as it happens instead for other compounds having multiple surface terminations [130]. In particular, figure 3.1 (b-v) shows that h_2 does not evolve in a warped rectangle, as h_1 does (panel b-ii), but in an almond-like shape, suggesting a different origin for the h_1 and h_2 bands.

In figure 3.1 (b-vi) and (b-vii), the quasi one dimensional (1D) character of h_2 is revealed by the linear dispersion of the band that crosses the surface Brillouin zone (BZ) with negligible dispersion along the k_c direction. This can be better seen in figure 3.2 where the CEM

of panel (b-vii) is reported. A black dashed line indicates the evolution of the h_2 state in the (k_a, k_c) plane.

The observation of the linear dispersion of the band h_2 provides new information about this material. Indeed, even though the crystal is formed by chains with reduced dimensionality, the quasi 1D band h_2 does not reach E_F. This can explain why the electronic transport properties do not reflect a 1D character.

3.2 Te $4d_{3/2}$ and $4d_{5/2}$ Core Levels

The core level PES of $ZrTe_5$ reveals a splitting of the Te $4d_{3/2}$ and $4d_{5/2}$ core levels. The Te $4d$ emission peaks, collected at a temperature of $\sim$ 77 K and at photon energy $h\nu = 75$ eV, are reported in figure 3.3 (a). These spectra clearly show a replica shifted by ~ 0.72 eV for both the $4d_{3/2}$ and $4d_{5/2}$ spin-orbit splitted peaks. We ascribe this replica to the presence of two differently coordinated Te ions at the surface.

To better clarify the origin of these spectral features in the $4d$ core levels, we performed density functional theory (DFT) calculations [1]. The calculated Te core levels are shown in figure 3.3 (b).

Relativistic norm-conserving pseudopotentials were used, including the $4d$ core states of Te. The density of state projected on the $4d$ orbitals of the three Te atom positions is shown in figure 3.3 (b). Te_t and Te_d correspond to the top and to the two bottom atoms of the $ZrTe_3$ prism, while Te_z corresponds to the atoms connecting the $ZrTe_3$ chains along the c axis. As it can be seen, the DFT results reproduce accurately the spin-orbit splitting of the $4d$ Te states.

The splitting of the core levels of atoms occupying different sites is also qualitatively described. In particular, the Te_t core levels are shifted up by ~ 0.6 eV with respect to the Te_z site core level. The projected density of states, which relies on the position of the Kohn-Sham eigenvalues and considering only the initial state, can only reproduce qualitatively the photoemission spectra. As a consequence, small discrepancies are observed in the energy shift estimation (~ 0.72 eV in the experiment, ~ 0.6 eV in the DFT model) and, more importantly, in the obtained binding energy values. However, the calculations provide us with valuable information about the mechanism at the origin of the chemical shift.

The calculated core level splitting gives an energetic position of the Te_z peaks that has not been observed experimentally. Within DFT, a more accurate estimation of the XPS spectra can be obtained by following the method proposed in Ref. [131]. Within this scheme, the

[1] DFT calculations have been performed by the group of prof. *O. Yazyev* of the École Politechnique Fédérale de Lausanne.

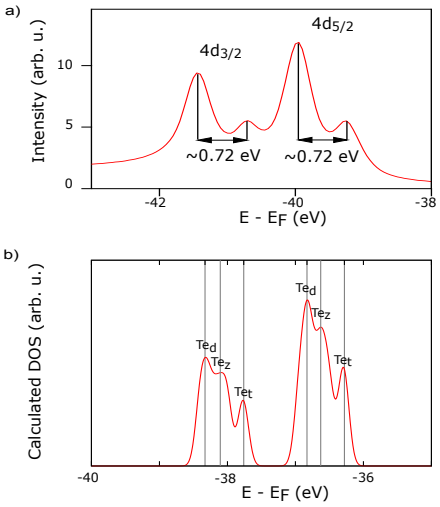

Figure 3.3: (a) Measured Te core levels: $4d_{3/2}$ and $4d_{5/2}$. (b) Calculated Te 4d core levels.

core level shifts are calculted as the difference of total energy between the unexcited system and a system with a core hole on an excited Te atom.

To simulate excited Te atoms, we produce a pseudopotential for Te where a hole in the $4d$ shell is treated as a core level. One excited atom is then introduced as an impurity in a $2 \times 2 \times 2$ supercell for each of the three inequivalent Te positions. These calculations show, in agreement with the experiments, that the Te_d and Te_z core levels are separated by only 8 meV while the Te_t core level is shifted upward by ~ 515 meV with respect to the Te_d level. The strong chemical shift of the Te_t core level with respect to the other Te sites can be ascribed to the different coordination of the Te ions. In particular, the Te_t atom at the top of the $ZrTe_3$ prism has longer bounds with the neighboring Zr and Te atoms when compared to the two other sites.

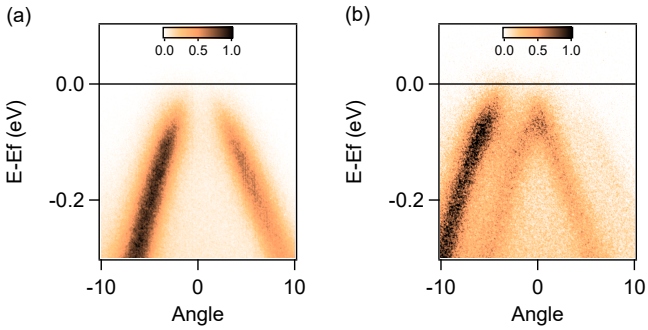

Figure 3.4: Electronic band structure of $ZrTe_5$ measured with s-polarized light along the chain direction ΓX at 300 K (a) on a single-domain region of the sample, (b) on a multi-domain region of the sample. A replica of the bare band dispersion is evident with an angular displacement equal to 4.3°.

3.3 Multiple Domains at the Surface

As a consequence of the low dimensional nature of the prismatic chains and of the weak interlayer binding energy, the cleaved surface of $ZrTe_5$ can result in a multiple domains structure, characterized by slightly different out-of-plane chain orientations. The existence of different domains results in the appereance of band replica in the ARPES images.

A special care when performing ARPES measurements allowed to avoid such spurious signal. Figure 3.4 shows a comparison between two ARPES images collected at 300 K with 6.2 eV photon energy.

The experimental conditions are exactly the same, but one measured sample region was composed by a single crystal (figure 3.4 (a)) while the other was composed by two crystals randomly oriented (figure 3.4 (b)). Figure 3.4 (a) shows a pair of bands, dispersing simmetrically with respect to the high simmetry Γ point and resulting from a single domain surface termination. Conversely, figure 3.4 (b) shows a weak clear replica of the bands, which is ascribed to the presence of a second domain with 4.3° misalignment.

This angle corresponds to an out-of-plane rotation, along the chain

axis. We found the ARPES signal from a single domain termination more often than the multiple domains signal. This suggests an average domain dimension larger than the beam spot size ($\sim 150\mu m \times 150\mu m$) used in the experiment.

3.4 Evolution of the Electronic Band Structure as a Function of the Temperature

Having detailed some significative features of the $ZrTe_5$ electronic band structure, we now turn to the study of the evolution of the electronic properties as a function of the temperature.

We have investigated in detail the temperature evolution of the electronic band structure of $ZrTe_5$ along the Zr chain direction, corresponding to the ΓX high symmetry direction in the reciprocal space. Along this direction, ΓX is equal to 0.78 $Å^{-1}$.

The experiment was performed in two laboratories. Two different but overlapping temperature ranges have been investigated.

Laboratory	Light Source	Photon Energy	Temperature	Figure
T-Rex	Laser	6.2 eV	125 K - 300 K	3.5
APE	Synchrotron	22 eV	16 K - 300 K	3.6

Table 3.1: Summary of the main parameters set during the two experiments at the T-Rex laboratory and at the APE beamline.

3.4.1 Laser-ARPES Data

In this experiment, only the states close to Γ (± 0.13 $Å^{-1}$) were detected, owing to the low photon energy (6.2 eV). However, previous ARPES experiments [16], band structure calculations [14] and Shubnikov de Haas studies [44] have shown that the maximum of the valence band and the minimum of the conduction band are located at the Γ point and disperse close to E_F. Hence, we expect that only these states are responsible for the electronic transport properties, while the low photon energy of this setup is not a significant limitation.

Figure 3.5 (a) and (b) show the laser-ARPES images of the valence band (VB), dispersing with negative effective mass, measured with s-polarized light at $T = 300$ K and $T = 125$ K, respectively. Figure 3.5

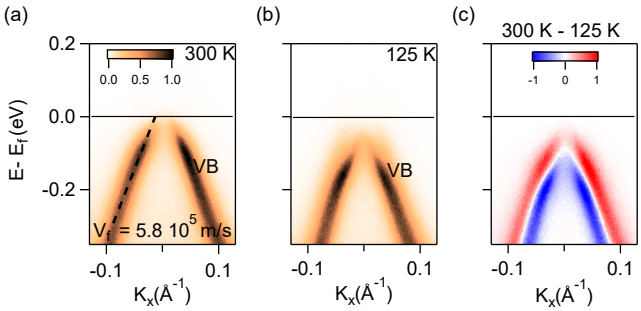

Figure 3.5: (a-b) Laser-ARPES measurements of $ZrTe_5$ oriented along the Zr chain direction ΓX at $T = 300$ K and $T = 125$ K, respectively, for s-polarized light. (c) Difference image obtained by subtracting the low temperature band dispersion from the high temperature one.

(c) shows the difference of the two, revealing a dramatic transfer of spectral weight.

These results are consistent with what we have observed in figure 3.1. The h_1 velocity, as extracted from figure 3.5 is , indeed, $5.8 \times 10^5 m/s$, in good agreement with the results reported in the previous section.

At 300 K, VB is found to cross E_F. The Fermi wave-vector k_F decreases at lower temperatures, consistently with the data reported in Ref. [13]. At 125 K, instead the binding energy of the band structure is higher respect to the one measured at 300 K. It is not clear if VB is crossing E_F anymore at this temperature.

3.4.2 UV-ARPES Data

We have repeated the same experiment at the APE beamline using 22 eV photon energy. Here, the temperature evolution of the $ZrTe_5$ electronic band structure was investigated in a wider temperature range, collecting ARPES data between 16 K and 300 K, with regular steps of ~ 25 K.

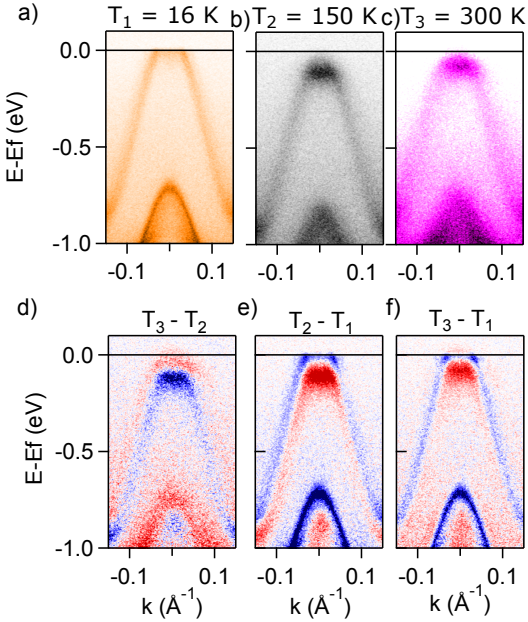

Figure 3.6: (a-c) UV-ARPES data, taken at $h\nu = 22$ eV, at a) $T_1 = 16$ K, b) $T_2 = 150$ K and c) $T_3 = 300$ K. (d-f) Differential ARPES images obtained by subtracting the low temperature dispersion from the high temperature one. Blue (< 0) and red (> 0) features in the differential images mark the temperature driven spectral weight transfer.

Three representative temperatures are reported here, $T_1 = 16$ K, $T_2 = 150$ K and $T_3 = 300$ K. The results are shown in figure 3.6 (a-c), respectively. Figure 3.6 (d-f) shows the differential maps resulting from the subtraction of the UV-ARPES data as follow: (d) T_3 - T_2, (e) T_2 -T_1 and (f) T_3 - T_1.

In this wider temperature range, a remarkable transfer of spectral weight is observed in all the three differential images. By cooling the sample from 300 K to 150 K (d), the band structure moves towards lower $E - E_F$ values. However, by further cooling the sample down

to 16 K, the band shift inverts direction between 150 K and 120 K reveiling an unexpected non-monotonic trend.

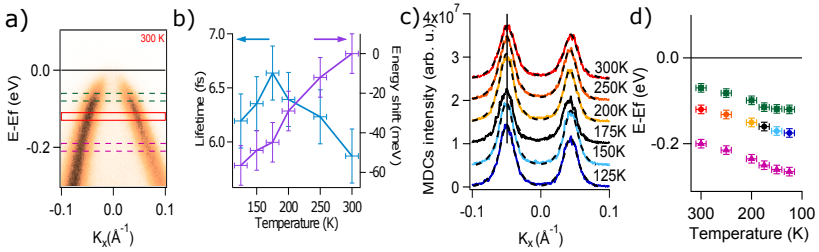

Figure 3.7: (a) Electronic band structure of $ZrTe_5$ measured with s-polarized light along the chain direction $\Gamma - X$ at 300 K. (b) Evolution of the binding energy shift and the quasiparticle lifetime as extracted from the fit of the MDCs at -0.115 eV as a function of the temperature. (c) MDCs cuts integrated over 20 meV, colored line in (a) and (b), and positively shifted along the vertical axis for the different sample temperatures. The traces are fitted (black dashed lines) with two lorentzian plus a polynomial background.(d) Energy of the MDCs cut versus sample temperature (colored), starting energy at 300 K: -0.115 eV, in green and purple the energy of MDCs cut done at different starting energies (-0.07 eV, green, and -0.2 eV, purple).

3.5 Rigid Shift of the Electronic Band Structure

In order to obtain a quantitative estimation of the observed band shifts, we used the following procedure. A momentum distribution curve (MDC), integrated over 20 meV, has been extracted at -0.115 eV from the Laser-ARPES measurement taken at 300 K, and the wavevectors k_a of the two peaks have been evaluated. The integration region is shown in the red rectangle of figure 3.7 (a). Then, MDCs have been extracted at all the measured temperatures. In these cases, the binding energies have been chosen in order to preserve the peak positions at the same wavevectors k_a. The energy position of the MDC extracted at T=300 K, $E - E_F \simeq -0.115$ eV, has been taken as a reference. The reported energy shift is the difference between the MDC energy found at temperature T with respect to the reference at T=300 K. Note that the MDCs have been fitted with a function which is the sum of two

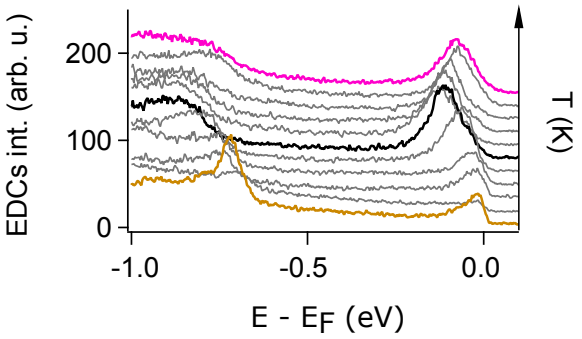

Figure 3.8: EDC curves extracted at $k_a \simeq 0$ $Å^{-1}$ integrating over $\simeq 0.025$ $Å^{-1}$ from ARPES data taken at different temperatures.

Lorentzians and a second order polynomial background. Figure 3.7 (b) shows the extracted energy shift.

Figure 3.7 (c) shows the resulting stack of MDCs as a function of the temperature along with the best fit, vertically shifted for the ease of reading. Besides the precise peak position, the MDCs fitting also provides information about the evolution of the peak width. The full width at half maximum (FWHM) has been used to evaluated the temperature evolution of the quasiparticle lifetime, τ_l, which is reported in figure 3.7 (b).

Between 300 K and 175 K, τ_l increases with decreasing temperature, as expected for a metal. Conversely, below $T < 175$ K, τ_l monotonically decreases. This is regarded as the signature of an increased electronic scattering rate as the VB is fully occupied.

We repeat the same procedure also starting from other energies (-0.07 eV and -0.2 eV at 300 K), thus tracking the peak position at a different k value. The results are shown in figure 3.7 (d), with colored circle markers for -0.115 eV, and purple triangle and green square markers for -0.07 and -0.2 eV, respectively.

For the UV-ARPES data the same procedure has been used but the reference momentum distribution curve (MDC), integrated over 20 meV, has been extracted at -0.3 eV from the UV-ARPES measure-

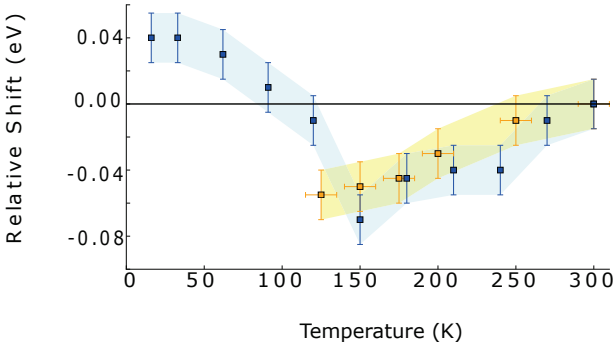

Figure 3.9: Evolution of the extracted energy shift as a function of the temperature. The laser-based ARPES datatset is represented with orange markers while the synchrothron-based ARPES dataset is represented with blue markers.

ment taken at 300 K.

The spectral weight transfer observed in the UV-ARPES data reported in figure 3.6 (d-f) can be better seen in figure 3.8 thanks to the energy distribution curves (EDCs) extracted from data taken at different temperatures between 16 K and 300 K. The EDCs have been taken at $k_a \simeq 0$ Å^{-1} and integrated over $\simeq 0.025$ Å^{-1}. The EDCs extracted from data at the three characteristic temperatures are shown in gold (T_1), black (T_2) and violet (T_3), respectively.

We now compare the shift value extracted from the two datasets. The minimum of the shift in the UV-ARPES measurements is found at ~ 150 K, hence close to the temperature of the resistivity maximum, T*. The full trend of the energy shift, as obtained from the synchrotron study, is shown in figure 3.9 (blue squares) and compared to the laser-ARPES data (orange squares). The two datasets overlap quite well. This result is chiefly important despite the uncertainties in the measurements, mostly due to possible significant discrepancies about the temperature measurements since they were taken using different setups.

The FS evolution as a function of the temperature brings comple-

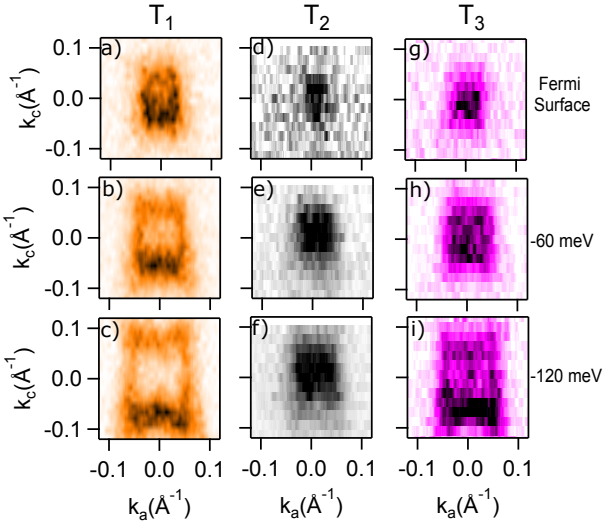

Figure 3.10: (a-i) Constant Energy maps taken at E_F, at -60 meV and at -120 meV, at three different temperatures ($T_1 = 16$ K, $T_2 = 150$ K and $T_3 = 300$ K).

mentary information about the non-monotonic band shift. In panels (a - i) of figure 3.10, we report the Fermi surfaces and different CEMs taken at $T_1 \simeq 16$ K (a - c), $T_2 \simeq 150$ K (d - f) and $T_3 \simeq 300$ K (g - i). Panels (a), (d) and (g) display the FSs of the material at different temperatures.

The band structure shifts toward higher binding energies, when the temperature is lowered from T_3 to T*. At T*, the maximum of VB is located approximately at E_F (figure 3.10, panel (e)). This determines a very low density of charge carriers available, inducing the rise of the resisitivity. When cooling the sample from 150 K to 16 K, the band structure shift inverts its trend, i.e. the bands move toward lower binding energies. At T_1 the band structure reaches the largest shift value with respect to the room temperature. This observation is supported by considering that the area of the hole pocket at temper-

ature T_1 (figure 3.10 panel (b)) is larger than the one at T_3 (figure 3.10 panel (h)). According to the raw data shown in figure 3.6 (a-c), the band structure shift is rigid without any significant change of the Fermi velocity.

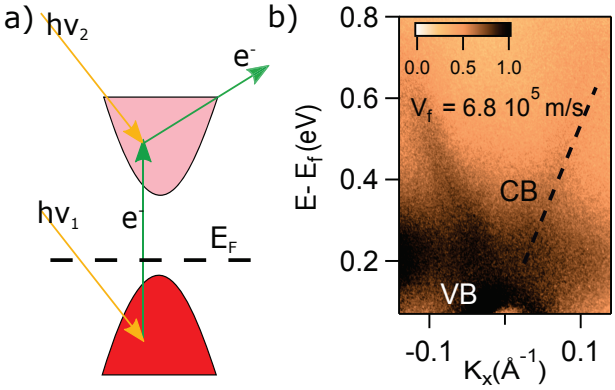

Figure 3.11: (a) A schematic of the 2PPE process. (b) Unoccupied conduction band (CB), probed with p-polarized light after optical excitation of electrons from the occupied VB. The band velocity, extracted from a linear fit, corresponds to $\sim 6.8 \times 10^5$ *m/s. This dataset was taken at* 300 *K.*

3.6 Revealing the Unoccupied Band Structure by 2PPE

A key result of our experiments was the possibility to directly visualizing the conduction band (CB) of $ZrTe_5$, that lies above E_F. This result has been achieved by transiently populating and detecting via a non linear two photons photoemission (2PPE) experiment the bands located above E_F.

In order to fully explain the mechanism at the origin of the $ZrTe_5$ anomalous transport properties it is mandatory to access the unoccupied band structure, whose contribution becomes relevant when new bands approach E_F at temperature close to T*.

The band dispersion of the unoccupied CB can be usually observed thanks to two photons photoemission (2PPE) experiments. Following this scheme, an optical excitation transiently populates CB, which is at the same time probed by an ultrafast UV laser pulse [142, 143]. A schematic of the 2PPE process is shown in figure 3.11 (a). 2PPE results

are interpreted as the projection of the initial state onto intermediate unoccupied states below the vacuum level.

Figure 3.11 (b) shows the results of the 2PPE experiment performed with p-polarized light on $ZrTe_5$. The intensity is almost completely suppressed in measurements with s-polarized light. Since the VB disperses around Γ with a negative effective mass, the observed positive dispersion is ascribed to the conduction band (CB), in agreement with *ab initio* calculations [14]. A linear fit of the band dispersion (dashed line in figure 3.11 (b)) results in a band velocity of 6.8×10^5 m/s, which is close to the value 5.8×10^5 m/s obtained for VB. These comparable band velocities leave open the possibility to describe these states as a 2D or a 3D Dirac Cone, as we will discuss in Chapter 5.

Moreover, our data are compatible with an energy gap not larger than 50 ± 10 meV, therefore comparable with the observed energy shift.

3.7 Conclusions

In this chapter we have reported a comprehensive investigation of both the occupied (VB) and unoccupied (CB) states of $ZrTe_5$ revealing a non-monotonic binding energy shift of these bands as a function of the temperature [24, 25].

$ZrTe_5$ is a metal at room temperature, having the valence band crossing E_F. By lowering the sample temperature from 300 K to $T^* \simeq$ 150 K, the band structure rigidly shifts towards higher binding energies, reaching a point with a very low charge carriers density or, maybe, a small gap. This fact can possibly explain the rising of the resistivity value at T^*.

By further cooling the sample to 16 K, we observe an inversion of the binding energy shift, i.e. a rigid shift towards lower binding energies, unveiling a non-monotonic dependence of the band structure of this material versus the temperature. This finding is in contrast with the data reported in Refs. [18, 19], however it is consistent with other works [16, 17] showing that, at low temperature (20 K [16] and 24 K [17]), the VB is crossing E_F. The material becomes, again, a conductor justifying the low value of the resistivity measured at $T<T^*$, consistently with the Shubnikov-de Haas study of Ref. [44].

We have shown experimental data justifying the resistivity anomaly of $ZrTe_5$. However, the change of charge carriers sign, as suggested by the thermopower measurements, is not fully understood and further investigations are needed in order to address this question.

Acknowledgments

We acknowledge prof. O. V. Yazyev and G. Autès for providing the DFT calculations , A. Akrap for the resistivity measurements, M. Grioni for the fruitful discussions and A. Magrez, H. Berger and Ph. Bougnon for supplying the $ZrTe_5$ single crystals. A special thanks also to I. Vobornik, J. Fuji and P. K. Das for their support during the experiments at the APE beamline at Elettra.

4

Ultrafast Optical Control of the Electronic Properties of $ZrTe_5$

In this chapter, we report on the possibility to control the electronic properties of $ZrTe_5$ on ultrafast timescales, by means of an ultrafast optical pulse. In this respect, Tr-ARPES is a very powerful tool which has recently unveiled important details about the physics of different families of materials such as superconductors [107,108], graphene [109, 110], charge density wave materials [111] and topological insulators [112–116].

4.1 Effect of the Optical Excitation

Figure 4.1 (a) shows the electronic properties of $ZrTe_5$ for an equilibrium lattice temperature of 125 K, before the arrival of the optical perturbation ($t - t_0 = -800$ fs). Figure 4.1 (b) shows the difference between the data immediately after ($t - t_0 = 200$ fs) the arrival of the pump pulse and the data before. Red and blue colours represent the photo-induced variation of spectral weight: the regions with a posit-

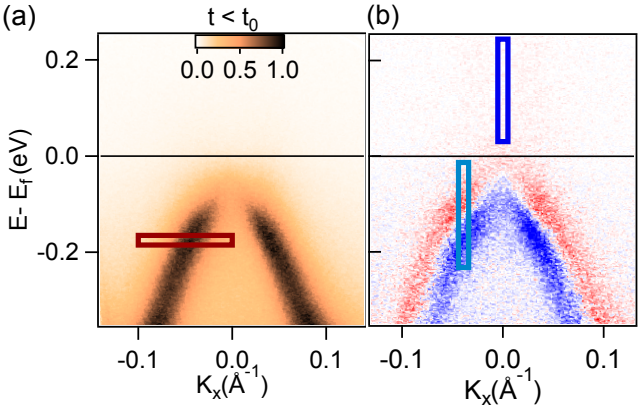

Figure 4.1: (a) Equilibrium electronic structure of $ZrTe_5$ measured along the chain direction with s-polarized light at 125 K before the optical excitation ($t - t_0 = -800$ fs). (b) Difference image between the data acquired immediately after ($t - t_0 = 200$ fs) and before ($t - t_0 = -800$ fs) the optical excitation.

ive variation are represented in red, while in blue the regions with a negative change of spectral weight.

Figure 4.1 (b) makes evident a large energy shift of the bands, which is very similar to that shown in figure 3.5 (c), obtained as a differential image between two ARPES maps acquired at equilibrium, at T= 300 K and T= 125 K. Clearly, this comparison shows that the optical excitation is responsible for two intertwined effects:

- the first is the promotion of charges from the valence band to the conduction band, as also previously observed for the 2PPE experiment shown in Chapter 3.

- The second effect is an increase of the electronic energy, originated from the increase of both the electronic and lattice temperatures, that produces an energy shift of the electronic band structure. However, a few femtoseconds temporal resolution would

have been necessary in order to disentangle the electronic and the lattice contributions. The overall temporal resolution of the setup is $\sim$ 250 fs, as seen in Chapter 2, unfortunately insufficient for observing possible differences between the lattice and the electronic dynamics.

Figure 4.2 (a) shows the temporal evolution of the MDCs at $E_F = -0.2$ eV for $-0.1^{-1} < k < 0^{-1}$ in the region limited by the brown rectangle in figure 4.1 (a). This small momentum window has been chosen in order to better visualize the dynamics of the band shift as a consequence of the transient temperature increasing. A shift of the band position, towards smaller k_a values, is clearly visible in proximity of $t - t_0 = 0$ fs.

The dynamics of the charge transfer between VB and CB can be also studied. Figure 4.2 (b) shows the temporal evolution of the electron population in VB and CB integrated in the energy-momentum windows enclosed by the light blue and blue rectangles, respectively, in figure 4.1 (b). The integration windows are chosen in order to fully contain the signal derived from the energy shift of the bands. The VB presents a negative signal, typical of an electronic depletion process, while the signal of CB is positive (and multiplied by a factor 5 for a better visualization), thus indicating that it is transiently populated by the optically excited electrons.

The two dynamics have been fitted with a single exponential decay $Ae^{-(t-t_0)/\tau}$, where A is the intensity, τ the characteristic decay time and t_0 indicates the time zero, *i.e.* the temporal overlap between pump and probe pulses. The function is convoluted with a Gaussian accounting for the finite experimental temporal resolution, i.e. $\sim$ 250 fs.

The single decaying exponential fit of the CB dynamics gives a characteristic time $\tau_{CB} = 0.8 \pm 0.2$ ps, which is significantly different from $\tau_{VB} = 1.6 \pm 0.2$ ps obtained from the fit of the signal originated by VB. We notice that the maximum of the signal in VB is delayed with respect to the one recorded in CB.

These findings can be rationalized considering a different orbital

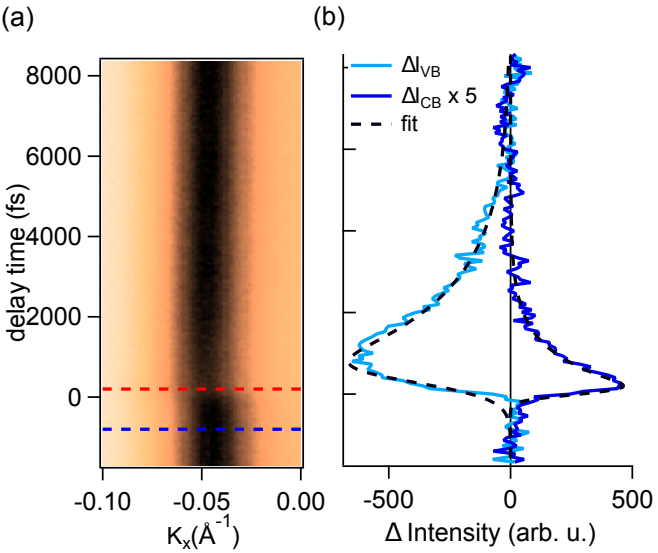

Figure 4.2: (a) Temporal evolution of the MDCs at −0.2 eV, integrated in the momentum window in the red rectangle of figure 4.1 (a). (b) Temporal dynamics of the electron population in CB and VB, obtained from the integration of the signal in the rectangles of figure 4.1 (b).

character for the VB and the CB. Different diffusion mechanisms can be responsible for both the electrons (holes) accumulation at the bottom (top) of CB (VB) and for their subsequent relaxation as reported, for example, for the case of the second generation topological insulators [116].

4.2 Study of the Pump-Probe Dynamics

In order to perform a more quantitative analysis of the Tr-ARPES data and compare the results obtained here with the results of the equilibrium study reported in Chapter 2, we exploit an approach similar to the one used for interpreting the data shown in figure 3.7 (b). In particular, the Full Widths at Half Maximum (FWHM) of the fit of the extracted MDCs was used to evaluate the temperature evolution of the quasiparticle lifetime, τ_l.

The lifetime τ_l increases with decreasing temperature, as expected for a metal, between 300 K and 175 K. Conversely, below $T < 175$ K, τ_l monotonically decreases. This finding was interpreted as the signature of an increased electron scattering rate as the VB approaches its full occupation.

Figure 4.3 summarizes the dynamics of the optically induced shift of the band structure. We compare the temporal dynamics of the MDCs measured at the equilibrium lattice temperatures of 125 K (blue) and 300 K (red). For these two temperatures, the MDCs are extracted at -0.2 eV and -0.14 eV, respectively, in order to compare the dynamics of the emission peak at the same k_a value, as discussed in the previous chapter.

Figure 4.3 (a) shows, with a vertical offset, two MDCs for an equilibrium lattice temperature of 125 K before (-800 fs, dark blue) and after the optical excitation (200 fs, light blue), along with the best fits obtained (black dashed lines). Each MDC has been fitted with a double Lorentzian function and a polynomial background, as done for the analysis of the MDCs in the previous chapter. From each fit we have obtained the temporal evolution of the parameters of the Lorentzian function: intensity, position of the maximum and width. Hereafter, we limit the discussion to the results for the band branch at negative k_a values.

Figure 4.3 (b) shows the evolution of the Lorentzian intensity, normalized to the value at equilibrium. The intensity decreases after optical excitation as a consequence of the increase of the temperature (broadening of the Fermi Dirac distribution) and the charge excitation

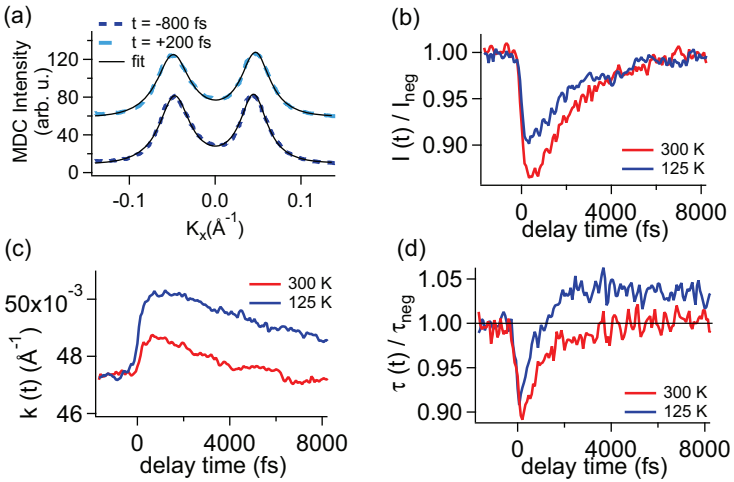

Figure 4.3: (a) MDCs extracted for a lattice temperature at equilibrium of 125 *K at* -0.2 *eV, as measured before* (-800 *fs, dark blue) and after* (200 *fs, light blue) optical excitation, displayed with a vertical offset. The best fit curves (black lines) are obtained with a double Lorentzian function plus a polynomial background. (b-d) results of the analysis of the Lorentzian fit to the MDCs as extracted at* -0.2 *eV (blue,* 125 *K) and* -0.14 *eV (red,* 300 *K). The two energies are chosen in order to compare the band peak dynamics at the same* k_a *position. (b) Dynamics of the left Lorentzian peak intensity at* 300 *K and* 125 *K, normalized to the negative time values. (c) Comparison between the peak positions. (d) Temporal evolution of the quasiparticle lifetime* τ_l*. A significant increase in the lifetime is observed at long delay time, only for the equilibrium lattice temperature of* 125 *K.*

from VB to CB. The ricovery time is approximately the same for both the temperatures.

Figure 4.3 (c) shows the dynamics of the momentum position of the maximum intensity, which shifts to larger momentum values reflecting the band energy shift. The two curves seem comparable in the dynamics even if the intensity of that at 300 K is half of that at 125 K.

Finally, we focus on the Lorentzian width, which is expressed in term of the quasiparticle lifetime τ_l, normalized to the value before optical excitation. In stark contrast to the intensity and the momentum position of the maximum intensity, which have qualitatively the same dynamics both at T = 300 K and 125 K, τ_l shows different behaviors for the two different equilibrium lattice temperatures. On a short time scale, both at 300 K and 125 K, τ_l lowers its value in correspondence to the optical excitation. However, on longer time scales, the two curves behave in a very different way. At 300 K, τ_l recovers its equilibrium value with a single decaying exponential with characteristic time of 1.1 ps. Conversely, at 125 K τ_l changes sign increasing by $\sim 5\%$ respect to the equilibrium value with a dynamics which is lasting longer than the investigated delay range. The increase of the quasiparticle lifetime is consistent with the increase of the electronic and lattice temperature, as shown in figure 3.7 (b).

4.3 Fluence Dependence of the Pump-Probe Dynamics

In this section, we study the influence of the pump fluence on the transient dynamics recorded in Tr-ARPES experiments. However, the fragility of $ZrTe_5$ crystals (they can be easily damaged by intense light pulses) and the relatively weak time-resolved transients limit the fluence range that can be safely explored from ~ 20 $\mu J/cm^2$ to ~ 400 $\mu J/cm^2$. As a matter of comparison, the pump power we set varied in the range $1 - 20$ mW.

The measurements have been performed at 125 K. Tr-ARPES images have been acquired for each pump fluence at three different delay times, as shown in figure 4.4 (a):

1. the first image has been taken at negative delay times, i.e. before the arrival of the pump pulse ($t - t_0 = -800$ fs). The data extracted from these measurements have been used as the reference.

2. The second image has been acquired at $t - t_0 = 0$ fs.

3. The third image has been collected at positive delay times, precisely at $t - t_0 = 2000$ fs.

MDCs have been extracted from each Tr-ARPES image at a binding energy of -0.2 eV, integrating over a 20 meV window. They have been fitted with a function constitued by two Lorentzian curves and a polynomial background. Similarly to the analysis performed for the data of figure 4.3, the relevant quantities are the Lorentzian peak intensity, its peak position and the lifetime (calculated from the width) of the two Lorentzian curves. Figure 4.4 reports the results of the analysis.

All the results have been referenced to the value determined before the arrival of the pump pulse, hence the values reported in figure 4.4 are relative and the ones referring to the $t-t_0 = -800$ fs case (reported in blue) are identically equal to 1.

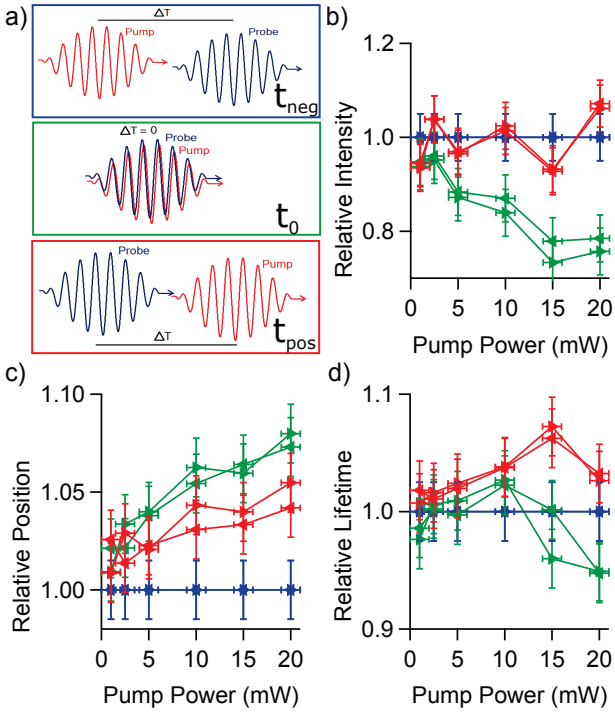

Figure 4.4: (a) Sketch of the three different delay times. (b) Relative intensity as a function of the pump power. (c) Relative peak position as a function of the pump power. (d) Relative lifetime as a function of the pump power. All the values have been evaluated respect to their t_{neg} value (blue). In green the values at t_0 and in red the values at $t_{pos} \sim 2000$ fs.

Figure 4.4 (b) shows the evolution of the intensity of the Lorentzian curves with respect to the $t - t_0 \sim -800$ fs case (in blue). At $t - t_0 = 0$ fs (in green), the intensity of the Lorentzian curves decreases upon increasing the pump fluence, showing a linear trend. This behaviour has been also observed in figure 4.3 (b), and can be explained by two combined effects: the increase of temperature (broadening of the Fermi Dirac distribution) and the charge excitation from VB to CB.

Both these two processes are enhanced by an increased pump fluence, hence explaining the linear behavior observed in the reduction of the intensity of the band. Since the dynamic of the intensity is quite fast, at $t - t_0 = 2000$ fs, as represented in red in figure 4.4 (b), the intensity has already recovered the value displayed for $t < t_0$.

Figure 4.4 (c) shows the behaviour of the peak position of the Lorentzian curves with respect to the $t - t_0 = -800$ fs values (in blue). As we have learned, it is possible to optically induce a rigid shift of the band structure. From the trend reported in figure 4.4 (b), it results that this shift is linear with the pump fluence, and shows no evidence of saturation, at least before sample damage occurs. The shift is clearly maximal at $t = t_0$, however a clear (but smaller) shift is also seen at $t - t_0 = 2000$ fs. It is interesting to note that the trend is linear also at $t - t_0 = 2000$ fs, and that the coefficient of the proportionality is similar for both delays.

The picture emerging from figure 4.4 (d) about the lifetime is less clear, and this is probably due to the fact that at the largest fluences a degradation of the quality of the ARPES images starts.

In conclusion, we observed that $ZrTe_5$ exhibits a non-saturating shift of the band structure up to the highest excitation level sustained by the material.

4.4 Conclusions

In this chapter, we have proven the possibility to optically modify the binding energy and quasiparticle lifetime of the valence band of $ZrTe_5$ on ultrafast timescales. The effects on the electronic band structure are perfectly matching their counterpart obtained under equilibrium conditions by changing the sample temperature. Consequently, the control on the ultrafast time scale of the transport properties of $ZrTe_5$, determined by the electronic properties of the sample, should be possible.

The analysis has been done first qualitatively by comparing the results obtained at equilibrum with those obtained out of equilibrium. Then, a quantitative analysis has been performed in order to verify the behaviour of the band structure dynamics, revealing a dynamics of the lifetime and of the peak position (i.e. of the band shift)lasting on a timescale larger than the probed temporal window. A study of the dependence of the band shift from the pump fluence has been also performed, revealing the possibility of controlling the band shift increasing the pump power.

These results provide an external knob to ultrafast control the $ZrTe_5$ conductivity and to unlock the route for a unique platform for magnetoelectric, optical, and thermoelectric transport applications [24].

Acknowledgments

We acknowledge M. Grioni for the fruitful discussions and A. Magrez, H. Berger and Ph. Bougnon for providing the $ZrTe_5$ single crystals.

5

On the Strong Topological Insulator Character of $ZrTe_5$

In Chapter 1, we have introduced the recent debate about the topological character of $ZrTe_5$ [14, 16–23]. In the present chapter, we report the results of a multi-disciplinary study aimed to address the question about the topological nature of this material [25–27]. Several experimental techniques and theoretical tools were used to this purpose:

- an ARPES study, in the ultraviolet (UV) range and in the soft x-ray (SX) range, was performed in order to measure with high accuracy the band structure in proximity of E_F and to disentangle, thanks to different probe depths and light polarizations, surface and bulk contributions.

- Scanning tunneling microscopy (STM) and spectroscopy (STS) measurements were done, in collaboration with the group of *M. Fonin* of the University of Konstanz. These measurements allowed to observe the surface order of the investigated samples, along with the metallic character of the $ZrTe_5$ surface.

- $ZrTe_5$ lies in proximity of a topological phase transition between strong and weak topological insulator, depending on its interlayer lattice distance [14, 15]. DFT calculations, done by the group leaded by *O. Yazyev* at the EPFL in Lausanne, have reproduced and confirmed the prediction of this topological phase transition.

- Since these calculations predict a strong dependence of the topological character of $ZrTe_5$ upon the interlayer distance $b/2$, XRD measurements were carried out in order to compare the exact experimental value with our calculations.

- Circularly Dichroic (CD-) ARPES was used as an indirect tool to estimate the spin polarization of the states at E_F. In particular, the strong CD signal observed in proximity of E_F is proposed to be a fingerprint of the presence of spin polarized states.

- Finally, the strong topological insulator character of $ZrTe_5$ was confirmed also by the measurements of the spin polarization of the surface state in proximity of E_F. This achievement was made possible thanks to the state-of the-art spin resolved ARPES setup available at the APE beamline (see Chapter 2).

5.1 Disentangling Bulk and Surface States in Proximity of the Fermi Energy: UV- and SX-ARPES Measurements

UV-ARPES measurements were performed at the APE beamline. The first spectrum acquired in this study is shown in figure 5.1 (a). It was taken at 165 K and at a photon energy of 22 eV. The temperature of 165 K was chosen to fully observe the electronic band structure below E_F, being the electronic band structure shift maximal around this temperature, as discussed in Chapter 3.

Two different states are clearly resolved in proximity of E_F. One, indicated as the valence band (VB), displays a M-like shape, while the second, labelled as a surface state (SS), reaches E_F following a linear dispersion.

Figure 5.1 (b) and (c) show the UV-ARPES measurements along the same direction, k_a, for two photon energies, 23.5 eV and 29 eV, corresponding to the ΓX and YX_1 high symmetry directions of the 3D Brillouin zone (BZ), respectively. In figure 5.1 (b), VB disperses almost linearly at the Γ point, with a small charge carrier density at E_F. In figure 5.1 (c), we observe additional spectral weight at $E - E_F = 0.1$ eV, for wave-vectors smaller than the one of the linearly dispersing state, as indicated by a black arrow. The VB state reaches its maximum below E_F and its dispersion deviates from linear, forming a M-like shape.

Looking at figure 5.1 (a-c), SS disperses linearly and it crosses E_F with no appreciable photon energy dependence. This behaviour is consistent with a state having a 2D character, i.e. a surface state.

Before discussing about the surface or bulk nature of the two states observed in the spectra of figure 5.1, it is important to analyze in more detail the two quasi-degenerate states in proximity of E_F. Figure 5.2 shows high resolution ARPES data, measured at 16 K and at the same photon energy of 22 eV. Although at 16 K the band structure shifts towards lower binding energies, leading to the impossibility of observing the top of the M-shaped band, the low temperature helps

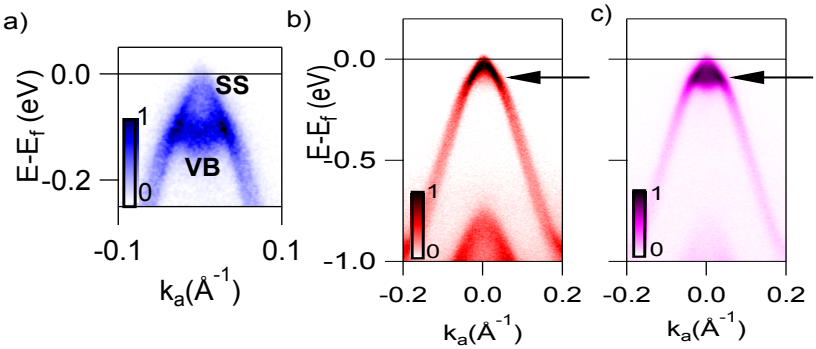

Figure 5.1: (a) A zoom of the UV ARPES measurements at E_F measured at 22 eV. Two states are clearly resolved. (b) and (c) UV ARPES measurements, for 23.5 eV and 29 eV corresponding to $\Gamma - X$ and $Y - X_1$. At Y two states are observed, one crossing E_F and the other forming a M*-like shape reaching its maximum below* E_F.

in getting sharper bands and, consequently, permits to determine finer details, like the presence of more than one band. Indeed, we can see that two bands are actually present.

Figure 5.2 (a) shows the Fermi surface of $ZrTe_5$, where the blue and green markers highlight the concentric hole pockets contours. These two quasi-degenerate bands crossing the Fermi Level can be easily observed in figure 5.2 (b), where an ARPES image taken at $k_c = 0$ Å^{-1} is shown. The presence of the two bands was already reported in the literature [13].

Further evidence of the presence of two distinct states in proximity of E_F, is obtained from a momentum distribution curve (MDC), integrated over 15 meV, as shown in figure 5.2 (b). The resulting MDC intensity is reported in figure 5.2 (c). Each branch at both positive and negative wavevectors clearly shows two peaks, thus confirming the presence of two distinct states in proximity of E_F at ~ 16 K.

In order to investigate the dimensionality of SS and VB, we performed an ARPES study of the $ZrTe_5$ electronic band structure as a function of the photon energy. Figure 5.3 (a) and (b) shows two con-

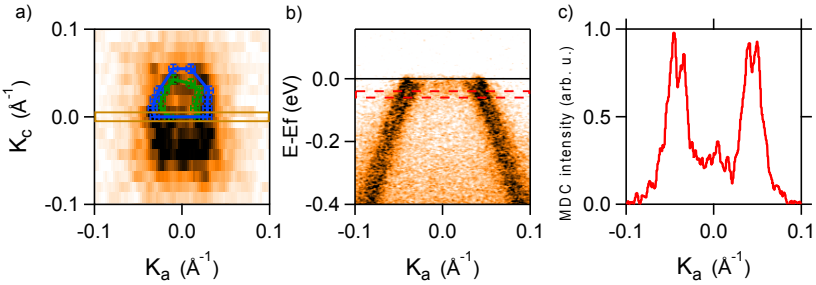

Figure 5.2: (a) Fermi Surface measured at 16 K and 22 eV. The blue and green markers indicate the position of the two concentric hole pockets. (b) Electronic band structure at $k_c = 0$ Å^{-1}. (c) MDC extracted in proximity of E_F. The band shows the presence of two quasi-degererate states.

stant energy maps (CEMs) extracted from the plane formed by the chain direction, k_a, and the surface orthogonal, k_b. The CEMs are extracted at -130 meV and -50 meV, respectively. This dataset was acquired with T= 210 K. These energies were chosen immediately below, 5.3 (a), and above, 5.3 (b), the maximum of VB at the Y point, as shown by the black and blue lines drawn on the ARPES image in figure 5.3 (c-d). In figure 5.3 (a-b) dashed colored lines indicate the positions of the band dispersion shown in figure 5.1. In figure 5.3 (a) we identify two contours: the first contour forms a closed pocket centered at the Y point. It arises from VB and its k_b dependence clearly reflects the bulk character of the state. The second contour is open, it arises from SS and it shows negligible k_b dispersions. In figure 5.3 (b), for energies larger than the maximum of VB at Y, only non-dispersing open contours are resolved.

The larger photoelectron mean free path achieved in SX-ARPES provides a more accurate mapping of the 3D periodicity of the BVB dispersion [132], as shown in figure 5.3 (e), displaying the SX photon energy scan for LV polarization. In all these measurements the sample temperature was kept at 15 K in order to suppress Debye-Waller-like reduction of the coherent spectral weight [133]. In this dataset the binding energy of the CEM is -50 meV, which corresponds to the

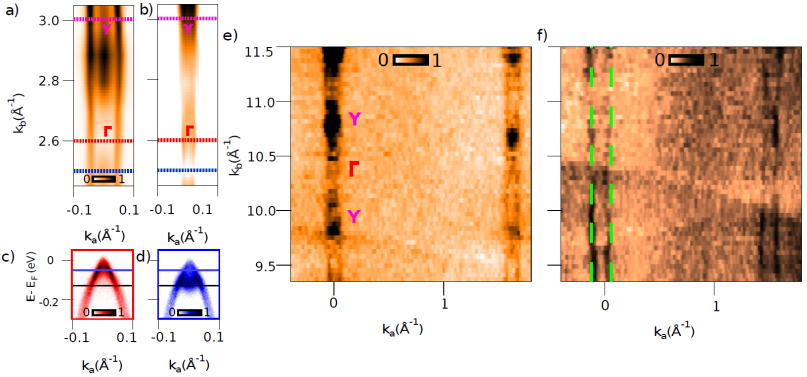

Figure 5.3: Photon energy dependent study of $ZrTe_5$. (a), (b) UV-ARPES constant energy map (CEM) in the (k_a,k_b) plane. The CEMs correspond to -130 and -50 meV, respectively. (c) and (d) ARPES images with black and blue lines indicating the energy of the CEM of panel (a) and (b), respectively. (e) and (f) CEM from SX-ARPES with LV and LH polarization, respectively. Green dashed lines indicate the 2D open contour of the surface state in (f).

same energy position of figure 5.3 (a) with respect to the electronic band structure, owing to the temperature dependent energy shift of the band structure seen in the previous chapters. We clearly resolve the VB state with 3D dispersion, with three replica along k_b well reproducing the data of figure 5.3 (a).

Furthermore, it is interesting to note the different origin of VB and SS, as inferred from their different response to the photon polarization. Indeed, figure 5.3 (f) shows a photon energy scan performed under the same experimental conditions of figure 5.3 (e), but with LH polarization. The 3D bulk pockets associated to VB are not anymore visible and only the open contours associated to SS are still present, indicated by the green dashed lines.

Figure 5.4 shows measurements taken along the $ZrTe_5$ chain direction with linear vertical (LV) polarization (on the right) and linear horizontal (LH) polarization (on the left) and for photon energies equal to 366 eV (on the top) and 341 eV (on the bottom) corresponding to

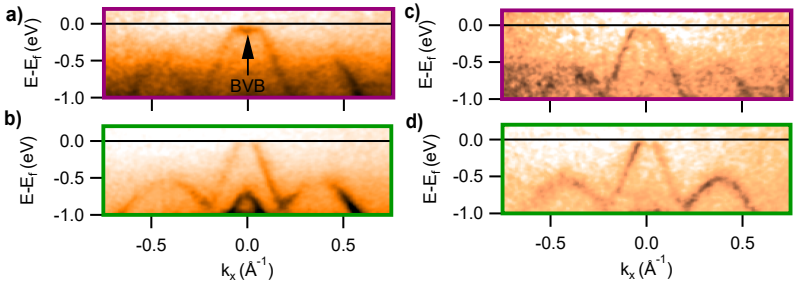

Figure 5.4: Electronic band structure of $ZrTe_5$ *measured with different light polarizations and photon energies. (a) 366 eV, vertical polarized light. (b) 341 eV, vertical polarized light. (c) 366 eV, horizontal polarized light. (d) 341 eV, horizontal polarized light.*

the Y-X_1 and Γ-X high symmetry directions, respectively.

As shown in figure 5.3, SS is well visible for LH polarization in both the ARPES images taken with photon energies of 341 eV and 366 eV. In contrast, VB is visible only with LV polarization and for $h\nu = 366$ eV. Accordingly to the SX-ARPES geometry, this effect can be interpreted as a consequence of the different symmetries of VB and SS, being the former *even* and the latter *odd*, with respect to the $ZrTe_5$ symmetry plane. The different matrix element effects in UV-ARPES and SX-ARPES experiments reflect the two different experimental geometries shown in chapter 2.

Figure 5.5 shows a comparison of the CEMs with UV-ARPES and SX-ARPES at the same binding energy shown in figure 5.3 (a).
Figure 5.5 (a-b) shows two CEMs taken in the (k_a, k_c) plane for two different photon energies. The former corresponds to the plan passing through the bulk Γ high symmetry point for $k_b \sim 2.6$ Å^{-1}, while the latter is taken at $k_b \sim 2.5$ Å^{-1}. By comparing figure 5.5 (a) and (b) we observe that additional spectral weight appears when the photon energy corresponds to k_b values far from the Γ point. We attribute this intensity to the M-like shape VB.

The polarization dependent change of the VB spectral weight is

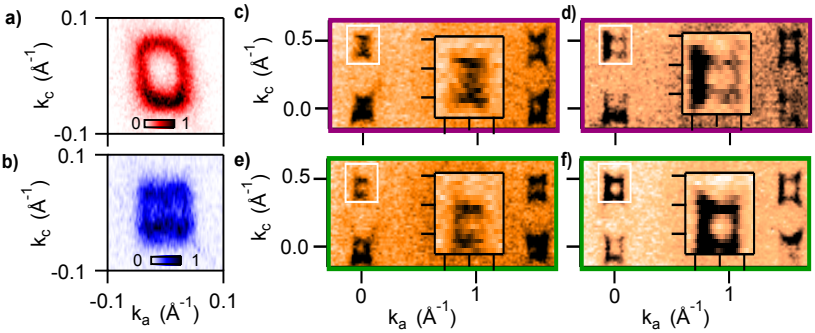

Figure 5.5: (a) CEM taken in the k_a, k_c plane for the $k_b \sim 2.6$ Å^{-1} value, corresponding to the Γ *high symmetry point, (b) CEM taken in the k_a, k_c plane for the $k_b \sim 2.5$ Å^{-1} value. (c) and (d) CEMs corresponding to the plan passing through the* Y *high symmetry point with LV and LH polarization, respectively, (e) and (f) CEMs corresponding to the plan passing for the* Γ *high symmetry point for LV and LH polarization.*

evident in the SX-ARPES CEMs shown in figure 5.5 (c - f). Figure 5.5 (c-d) corresponds to the plane passing through the Y high symmetry point with LV and LH polarization, respectively, while panels (e) and (f) correspond to the plane passing for the Γ high symmetry point for LV and LH polarization. In figure 5.5 (c), the contour measured with LV polarization matches the UV data of figure 5.5 (b). Whereas in figure 5.5 (d), for LH polarization, no spectral weight is present at the Y point, as a consequence of the VB suppression.

The photon energy and polarization dependence of the CEMs provide important additional information to disentangle the surface and bulk contributions at the top of VB.

5.2 Gapless States Observed with Scanning Tunneling Microscopy and Spectroscopy

We have performed scanning tunneling microscopy (STM) and spectroscopy (STS) investigations on $ZrTe_5$ with the aim of looking for the presence or the absence of a gap in the density of staets (DOS) at E_F.

The STM and STS experiments were performed[1] on *in situ*-cleaved samples in a UHV chamber equipped with an Omicron Cryogenic STM, operating in constant-current mode at 10 K. The STS measurements were recorded using a lock-in amplifier with a modulation voltage of 5 mV_{rms} and a modulation frequency of 687 Hz. The bias voltage is applied with respect to the sample. This allows to directly access both the occupied and unoccupied DOS, below and above E_F. High-resolution STM images show the atomic structure of the $ZrTe_5$ surface, composed of chains of protruding pairs, separated by apparently monoatomic lines, as depicted in figure 5.6 (a).

According to our ARPES results, the top of VB lies in proximity of E_F. Hence, in order to obtain insight about the conductivity in the bulk band gap, we performed STS in a low bias voltage range. Figure 5.6 (b) presents the dI/dV spectrum in the range -150 meV - $+150$ meV. The negative energy values correspond to the occupied states. Within this range, the curve appears to be characterized by a monotonic decrease/increase of conductivity with a minimum at around -15 meV, as clearly seen in the inset of figure 5.6 (b), which represents a plot of the same spectrum in the range -50 meV - $+50$ meV.

Remarkably, within our experimental resolution, the conductivity of the sample never vanishes. To further investigate this matter, we performed STM imaging at very low voltage bias, as shown in figure 5.6 (c) and (d). Both below (-20 mV) and above ($+10$ mV) E_F, we were able to image the atomic stripes of the $ZrTe_5$ structure, even over areas which are larger than 100 nm.

In order to demonstrate the two-dimensional nature of the state

[1] STM and STS measurements and analysis have been carried out in the group of *M. Fonin* at the University of Konstanz.

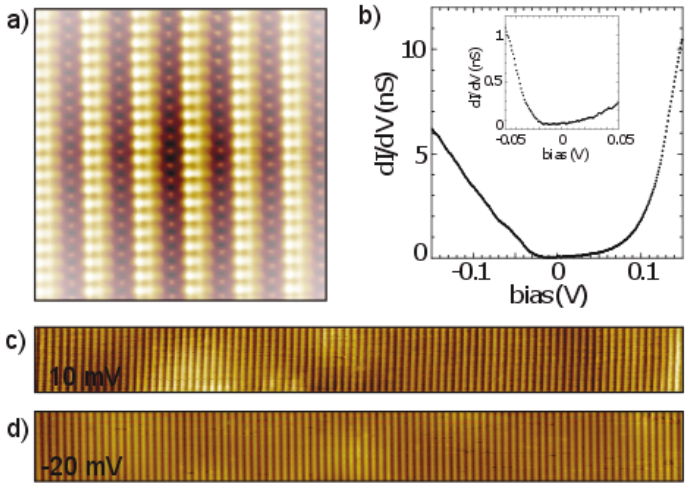

Figure 5.6: Gapless density of states at the surface of $ZrTe_5$. (a) Atomic-resolution STM image of the $ZrTe_5$ surface (8 nm × 8 nm). Image conditions: $V = -300$ mV, $I = 300$ pA. (b) dI/dV spectrum on the $ZrTe_5$ surface. Set point: $V = 0.15$ V, $I = 0.3$ nA, $V_{mod} = 5$ mV. Inset: detail of the same spectrum, plotted in the ± 50 mV range, (c) and (d) STM topography image of the $ZrTe_5$ surface (120 nm × 13 nm) recorded at $V = 10$ mV and $V =$ -20 mV respectively, $I = 250$ pA.

close to E_F, we acquired $\mathrm{d}I/\mathrm{d}V$ conductance maps on $ZrTe_5$. Whereas, adsorbed defects seemed to be unable to produce the necessary scattering conditions, in the presence of step edges we revealed standing wave oscillations of the local density of states, whose features depend on the acquisition energy.

Figure 5.7 (a) shows the topographic image reported also in figure 5.6 (d) and figure 5.7 (b-g) the $\mathrm{d}I/\mathrm{d}V$ maps, of the same region as a function of the bias voltage. The measurements have been acquired in close proximity of a step edge, which has been kept just over the scan frame in order to prevent tip instabilities during the map acquisitions.

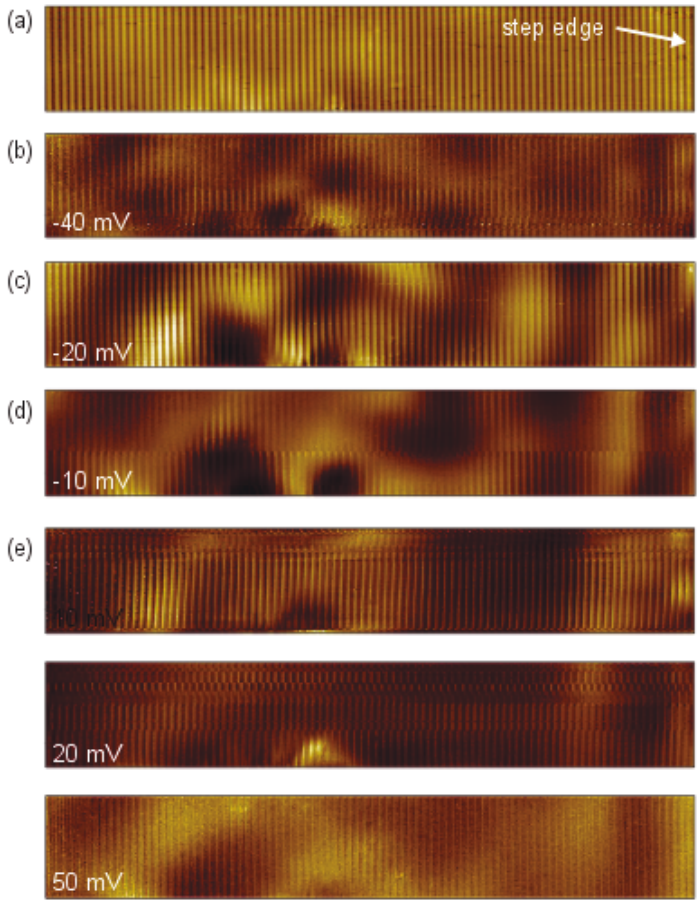

Figure 5.7: (a) STM topography image (V = -20 mV) at the vicinity of a step edge oriented along the a crystallographic axis of $ZrTe_5$. (b-g) Corresponding dI/dV maps obtained at different energies. Image conditions: 120 x 20 nm, $I = 250\ pA$, $V_{mod} = 5\ mV$.

A modulation of the contrast of the map is evident in all the maps. This effect can be attributed to standing electron waves, extending over the whole picture frame. The wavelenghts of these features can roughly be estimated in few tens of nm and it is apparently varying with the energy. Therefore we attribute them to the surface state of $ZrTe_5$.

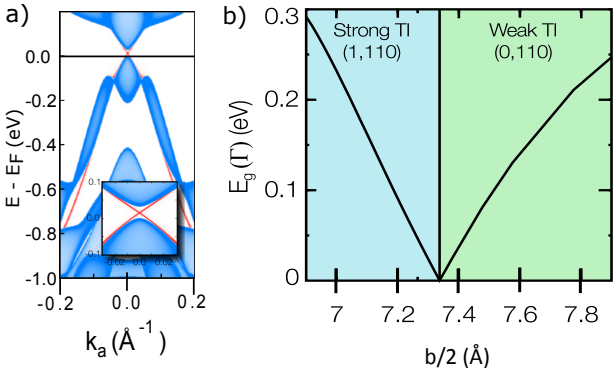

Figure 5.8: (a) Calculated momentum resolved bulk density of states projected on the (010) *surface (blue) and momentum resolved surface density of states at the* (010) *surface (red), for* $b/2 = 7.23$ *Å. The surface state is more clearly visible in the zoom at* E_F *in the inset. (b) Band gap at* Γ *as a function of the interlayer distance* $b/2$.

5.3 Theoretical Prediction of the Topological Phase Transition and Estimation of $b/2$ with X-Ray Diffraction

The interpretation of the experimental results has been supported by DFT calculations[2] of the electronic band structure of $ZrTe_5$.

Ab initio calculations have been carried out, using the crystal lattice parameters taken from Ref. [134], within the density functional theory (DFT) framework employing the generalized gradient approximation (GGA) as implemented in the QUANTUM ESPRESSO package [135]. Spin-orbit effects were accounted by using fully relativistic norm-conserving pseudopotentials [136].

The measured band structure is well reproduced by *ab initio* calculations, as shown in figure 5.8 (a). The projected bulk band structure

[2] *Ab initio* calculations have been done by the group of *O. Yazyev* of the École Politechnique Fédérale de Lausanne.

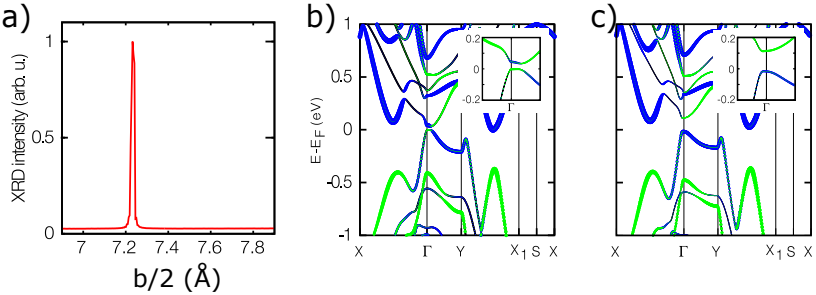

Figure 5.9: (a) X-ray diffraction intensity of the $b/2$ peak measured at 300 K. (c- d) Calculated band structure of bulk $ZrTe_5$ for the experimental interlayer distance $b/2 = 7.23$ Åand an enlarged interlayer distance of 7.5 Å, respectively. Green and blue colors indicate the weight of the states on the Te_d and Te_z p orbitals. The inset shows a closeup in the bulk gap region at Γ.

(blue area) captures the evolution of VB from linear to the M-like shape. More importantly, a surface state (red line) disperses within the band gap, as emphasized in the inset.

When *ad hoc* measured crystal structure parameters are used, DFT calculations predict that $ZrTe_5$ is a STI. When the spin-orbit coupling is not taken into account, conduction and valence bands are degenerate along a nodal line in the $k_y = 0$ plane. Spin-orbit coupling breaks this degeneracy resulting in a STI phase with a band inversion at Y. The product of parities of the valence band states at the Y point $k_Y = (\frac{1}{2}, \frac{1}{2}, 0)$ is reversed with respect to the other time-reversal invariant momentum (TRIM) k-points which indicates that the Z_2 topological invariants are $(1, 110)$.

Upon increasing the interlayer distance $b/2$, the gap at Γ decreases, closes and reopens (see figure 5.8 (b)) in a phase where the product of parities of the valence states at Γ is reversed and $ZrTe_5$ is a WTI with invariants $(0, 110)$. The observation of a topological phase transition is in agreement with the results of *Weng et al.* in Ref. [14].

At the transition between the weak and strong phases, for $b/2 =$

7.35 Å, the gap is closed at Γ and $ZrTe_5$ lies in a Dirac semimetal phase. However, it is of paramount importance to note that this Dirac semimetal phase requires a fine tuning of the interlayer distance.

Figure 5.9 (a) shows the results of our x-ray diffraction study. The experiment has been performed at the XRD1 beamline using a photon energy of 8.8 keV and measuring at 300 K. The experimental value of the interlayer distance is $b/2 = 7.23 \pm 0.02$ Å. This is consistent with a previous XRD study [134], indicating that the $ZrTe_5$ sample investigated in our work lies in the STI phase.

The band structure of $ZrTe_5$ in the strong phase obtained from the experimental structure, and in the weak phase, as obtained for a strained structure with $b/2 = 7.5$ Å, are shown in figure 5.9 (b) and (c), respectively. The band inversion taking place at Γ during the topological phase transition can be highlighted by computing the weight of the states on the p orbitals of the Te_d and Te_z atoms, indicated by blue and green colors in figure 5.9 (b-c).

The temperature evolution of the interlayer lattice distance $b/2$ was investigated by performing a XRD study in the temperature range 300 K - 100 K. Figure 5.10 shows the evolution of the $b/2$ value as extracted from the XRD data. We report a monotonic decreasing of the interlayer distance, from $b/2 = 7.23\pm 0.02$ Å (at 300 K) to $b/2 = 7.20\pm 0.02$ Å (at 100 K).

This monotonic decrease of the interlayer lattice distance is in agreement with what reported by *Fjellvåg et al.* in Ref. [134]. The authors have measured a variation of all the lattice parameters with the temperature. The variation along the three structural directions takes place upon cooling (or heating) but it is not proportional along the three structural axis [134]. This fact is not accounted for a *normal* thermal expansion [134].

The relatively strong bonding and the low thermal expansion along the a direction, which is the direction of the Zr chains, reflect the first structural approximation which consider $ZrTe_5$ as a pseudo-one-dimensional material [134]. However, the Te_3 - Te_3 linkages along the a, c directions give the distinct two dimensional character of this compound, qualifying $ZrTe_5$ as a quasi two dimensional material obtained

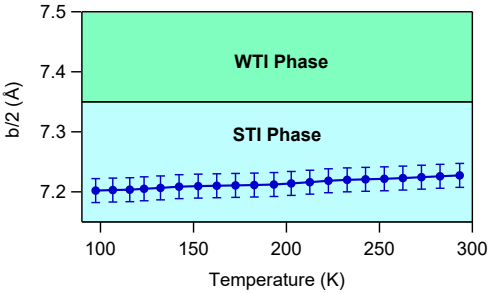

Figure 5.10: Temperature evolution of the interlayer lattice distance b/2, as extracted from the XRD measurements in the temperature range 300 K - 100 K. Black line indicates the b/2 = 7.35 Å value which is predicted by the theory to separate the WTI phase (larger b/2 values) from the STI phase (smaller b/2 values).

from the stacking of different planes connected by a weak interlayer binding energy [134]. Since the interlayer distance (along the b axis) is quite large, the weak interlayer coupling was interpreted by a previous theoretical work as being of van der Waals type [14].

In the work of *Weng et al.*, the interlayer binding energy, i.e., the unit-area total-energy difference between the single-layer sheet and the 3D bulk, is calculated for one single set of lattice parameters [14]. Their result suggests that the interlayer binding energy of $ZrTe_5$ ($\sim$ 12.5 meV/ Å^2) is as weak as that of graphite ($\sim$ 9.3 meV/ Å^2) and is much smaller than that of Bi_2Se_3 ($\sim$ 27.6 meV/ Å^2) and Bi (111) bilayers ($\sim$ 40.1 meV/ Å^2) [14]. The variation of the interlayer binding energy as a function of the change of the interlayer distance induced by the temperature is not reported in any published study, at the best of our knowledge.

By plotting the experimental $b/2$ values obtained with XRD measurements and the $b/2$ value predicted to be at the boundary between the WTI and the STI phases, we can conclude that the experimental $b/2$ value is always smaller than the value of 7.35 Å.

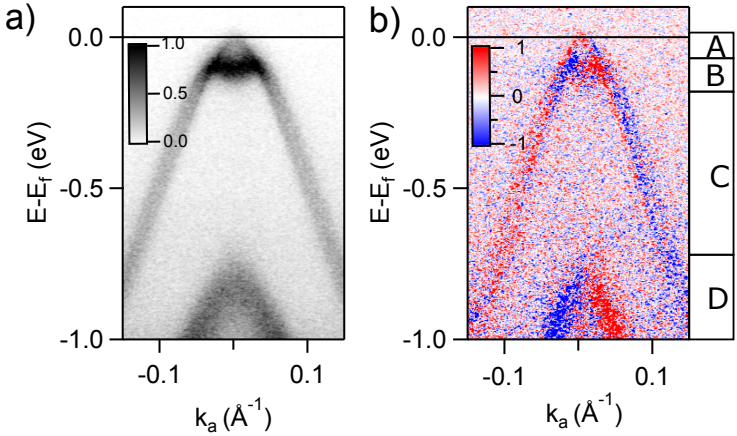

Figure 5.11: (a) ARPES image taken at $h\nu = 22$ eV and $T = 210$ K. The photon energy was linear horizontal. (b) Dichroic differential image obtained from the difference $I^L - I^R$ where I^L and I^R have been obtained with circular polarized light (left and right, respectively). The image has been divided in four energy regions of interest A, B, C and D.

5.4 Circular Dichroic ARPES Measurements

Either a direct or an indirect measurement of the spin polarization of the SS can provide another proof of the STI character of $ZrTe_5$. The need to study the spin texture of strongly spin-orbit-coupled materials has recently promoted circular dichroic angular resolved photoelectron spectroscopy (CD-ARPES) as an indirect but powerful tool to infer about the spin polarization. Nonetheless, a quantititave analysis requires to account for final state and photoelectron interference effects [137].

Figure 5.11 (a) reports the ARPES data measured at 22 eV, with linear horizontal polarization at 210 K. These data are used for comparison with the CD-ARPES data taken at 210 K shown in figure 5.11 (b). This figure has been obtained from the difference $I^L - I^R$ between two ARPES maps acquired with left (I^L) and right (I^R) circularly po-

larized light.

The ARPES map of figure 5.11 (b) can be divided in four different energetic regions. In region A, B and C the SS and the VB have been taken in exam. In particular, A and C share the same behaviour, i.e. positive signal for negative k_a and viceversa. It is important to note that, in region A, the VB and the SS states are well separated in energy, whereas they are almost degenerate in the region C.

Region B displays an opposite behaviour. The signal is negative for negative values of k_a and viceversa. In this region the CD signal is clearly distributed along the M-like shape of BVB, hence it mainly originates from the bulk state.

In a STI, the existence of a topologically protected surface state is a consequence of an inversion in the energy ordering of the states forming the band gap. These are also characterized by different parities at time reversal invariant high symmetry points (in particular, in the present case at Γ) [47]. In the case of $ZrTe_5$, the opening of an inverted band gap has been also interpreted as the origin of the M-like shape at the VB top. We propose that the CD signal sign reversal at the top of VB might be the signature of this band inversion between the bottom of the CB and the top of the VB.

Finally, in region D, the h_2 band presents a very strong dichroic signal. This band exhibits an opposite character, compared to the behavior of the VB and the SS in region C. This confirms that h_2 is not a replica of the VB, as also discussed in chapter 3. Hence, the different CD-ARPES signal reported in region C and D indicates a different orbital character of SS in h_1 and the top of h_2.

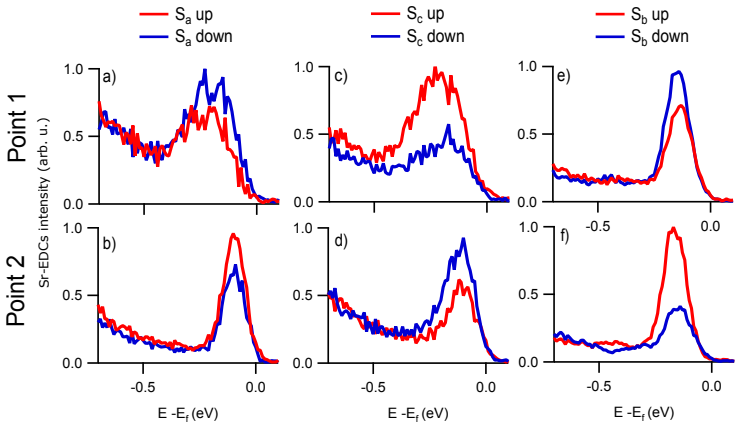

Figure 5.12: Sr-EDCs for the spin up (red) and down (blue) polarization parallel to (a-b) k_a, (c-d) k_c and (eff)k_b. The Sr-EDCs have been measured in Point 1 *($k_a = -0.06$ Å^{-1}, $k_c = 0$ Å^{-1}) and* Point 2 *($k_a = +0.06$ Å^{-1}, $k_c = 0$ Å^{-1}), respectively.*

5.5 The Spin Polarized State at the Surface

The non trivial topological character of the SS was further investigated by means of spin resolved ARPES (Sr-ARPES) using the setup available at the APE beamline, described in Chapter 2 and in Ref. [124].

The experiment was carried out at 165 K, with a photon energy equal to 22 eV. The photon energy has been chosen considering that, at 22 eV, spin integrated ARPES is capable to fully resolve the dispersion of the SS from the VB, as shown in figure 5.11 (a) of the previous section. The angular resolution of the setup is $\sim 0.75°$ and the energetic resolution is ~ 100 meV. The S_a component has been measured with the *white* detector, while the S_b and S_c components have been measured with the *black* detector.

Owing to the lower energy and angular resolution of Sr-ARPES, when compared to spin integrated ARPES, the VB and the SS emissions cannot be disentagled in the Sr-EDCs. Nonetheless, we assume that VB does not contribute to the measured spin polarization, since

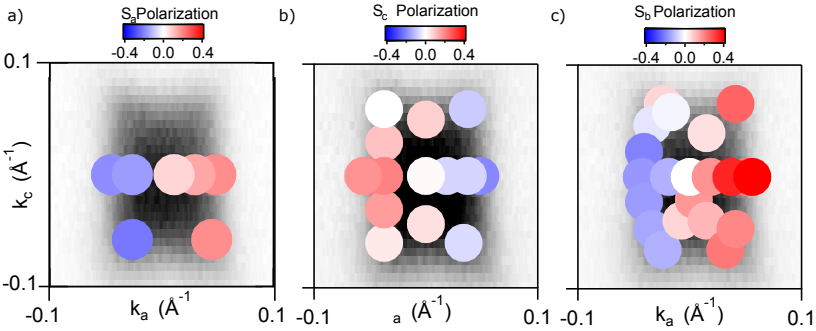

Figure 5.13: Fermi surface (FS) in the (k_a, k_c) *plane obtained in the same experimental condition of the spin resolved measurements, at* 165 *K with* 22 *eV photon energy. Open circles indicate the point where spin resolved energy distribution curves (SR-EDCs) have been acquired. The color of the circle corresponds to the degree of spin polarization along the* k_c *direction. The circle dimension corresponds to the momentum resolution of the measurements. In panel (a) the intensity of the spin polarization parallel to the* k_a *direction is reported, in panel (b) the intensity of the spin polarization parallel to* k_c *and in panel (c) the out of plane component, parallel to* k_b.

VB is a 3D bulk state and it is expected to be spin unpolarized. The presence of VB emission represents a background constant for both spin components and it might only lead to an underestimation of the real spin polarization of SS.

Figure 5.12 reports Sr-EDCs along the three cristallographic components a, b and c. They have been reported for two significative points of the FS. *Point 1* is at ($k_a = -0.06$ Å$^{-1}, k_c = 0$ Å^{-1}) and *Point 2* is its symmetric: ($k_a = 0.06$ Å$^{-1}, k_c = 0$ Å^{-1}).

All the three directions report a clear signal of spin polarization of the band. The spin polarization reverses sign with the change of sign of k_a for all the measured components.

For the S_a (5.12 (a-b)) and S_c (5.12 (c-d)) components the signal is small and noisy, while for the S_b component (5.12 (e-f)) a stronger signal is evident.

Figure 5.13 shows the Fermi surface (FS) in the (k_a, k_c) plane and

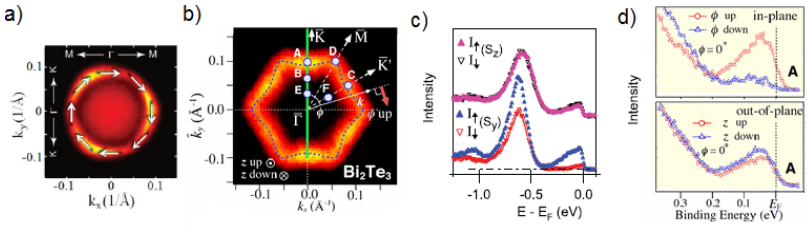

Figure 5.14: (a) FS of Bi_2Se_3. The theoretical spin polarization orientation of the SS at E_F is depicted by the white arrows. (b) FS of an n-type Bi_2Te_3 crystal, highlighting the snowflake-like FS. (c) Sr-EDCs along the in-plane P_y and out-of-plane components P_z. (d) In-plane and Out-of-plane Sr-EDCs measured in corrspondence of the A-point of (b). (a) and (c) have been adapted from [138]. (b) and(d) have been adapted from [139].

the colored circles indicate the positions in the BZ where spin resolved energy distribution curves (Sr-EDCs) have been acquired. The color of the circles quantifies the spin polarization values, averaged under the Sr-EDCs peak. The dimension of the circles is approximately reproducing the angular resolution of each measurement. Here, it results evident that all the three components reverse sign with the change of sign of k_a.

While the sign reversal of the S_c and S_b components is evident and geometrically clear, the behaviour of the S_a component is surprising and not completely understood. Unfortunately, the S_a component is also the one with less statistics. Data for positive k_c values are needed to better understand the behaviour of the S_a component. Consequently, we will discuss only the S_b and S_c components.

The highest polarization measured along the S_c components is $\sim$ 20%, while the maximal polarization along the S_b component is $\sim$ 40%. The strong signal along the S_b component is another surprising result of these Sr-ARPES measurements. The measured spin polarization in proximity of E_F fully supports the presence of surface spin helical states.

The spin-polarized surface states, forming the Dirac-cone, have

been investigated for many topological insulators with spin integrated and spin resolved techniques. Bi_2Se_3, the prototipical topological insulator, shows a circular FS [138], as reported also in figure 5.14 (a).

Another topological insulator of the *second generation* is Bi_2Te_3. This TI has, instead, a snowflake-like FS, as shown in figure 5.14 (b). It has been shown that the FS shape and the spin projections have a correlation. Bi_2Se_3, with its perfectly circular FS, has only tangential components of the spin orientations [138] while Bi_2Te_3 has spin projections with a non-zero out-of-plane component [139]. This is clearly shown in figure 5.14 (c-d).

A quick comparison between the Bi_2Te_3 case and the measurements reported in figure 5.13 for $ZrTe_5$ point out a possible origin for the non-zero S_b component of $ZrTe_5$. The FS of $ZrTe_5$ is not perfectly circular and shows a clear warping in its contours. This can be at the origin of the non-zero S_b component measured in our experiment, as in the Bi_2Te_3 case of Ref. [139].

5.6 Conclusions

In this chapter we have shown the results of a comprehensive experimental and theoretical investigation of the electronic and structural properties of the bulk $ZrTe_5$ [25–27].

The material is a bulk strong topological insulator (STI), both above and below the temperature of the resistivity peak T*. ARPES experiments, performed in the UV and SX photon energy ranges, show that the top of the valence band is formed by two nearly degenerate states. One has bulk 3D character, while the second shows no dispersion with the photon energy, and it is interpreted as a surface state. By exploiting Sr-ARPES, the spin polarization of the surface state is clearly resolved. Finally, scanning tunneling spectroscopy (STS) reports a gapless density of state for energy above and below E_F, thus fully supporting the description of $ZrTe_5$ in term of a STI. $ZrTe_5$ is calculated to lie near a topological phase transition to a weak topological insulator (WTI) phase that can be triggered by an increase of the interlayer distance, b/2. For the sample investigated in this study, values of b/2 between 7.23 Å and 7.2 Å were determined by x-ray diffraction measurements froom room temperature to 100 K, ensuring that the material is in the STI phase for all the studied temperatures.

Our observations reconcile the recent conflicting results about the topological character of $ZrTe_5$ [14, 16–23]. Importantly, $ZrTe_5$ is not a 3D Dirac semimetal, as this phase is not protected by crystalline symmetry and can only be realized precisely at the topological phase transition. Nonetheless, the band dispersion is close to a 3D Dirac semimetal thus explaining the recent optical and electron transport measurements [16, 20, 21, 28–30].

The close vicinity to the topological phase transition suggests the possibility of engineering the topological phase by a small variation of the interlayer distance, entering in the WTI phase. This can be achieved by changing the concentration of defects, that may vary depending on the growth conditions, thus also accounting for the experimental observation of different T* in different studies [16, 24, 33, 140]. The topological phase transition may also be achieved in a controlled

way either via alkali metal intercalation [19], as exploited for decoupling MoS_2 single layer [141], or via chemical substitution [17]. This will require further ARPES investigations of *ad hoc* grown samples with controlled doping and/or defect density. Finally, the observed monotonic decrease of $b/2$ as a function of temperature suggests that, once the WTI phase is achieved, transition to the STI phase can be controlled by temperature, thus making $ZrTe_5$ a versatile platform for spintronics applications [144].

Acknowledgments

We acknowledge prof. O. V. Yazyev and G. Autès for providing the DFT calculations, prof. M. Fonin, L. Gragnaniello, T. Kuhn, V. Enenkel for the STM and STS measurements and A. Magrez, H. Berger and Ph. Bougnon for supplying the $ZrTe_5$ single crystals.

Thanks to I. Vobornik, J. Fuji, P. K. Das for the support during the experiments at the APE beamline, to L. Barba for the help during the XRD measurements performed at the XRD1 beamline at Elettra and to V. N. Strocov and F. Bisti for their support during the SX-ARPES measurements at the ADRESS beamline of SLS.

A special acknowledge also to C. Bigi for the fruitful discussions regarding the spin ARPES data analysis.

Concluding Remarks

For several years the transport properties of the pentatelluride $ZrTe_5$ have challenged scientists for the anomalies displayed at a characteristic temperature T*. The resistivity is peaked at T*, tripling its room temperature value. The thermopower, instead, inverts its sign, passing from a positive value at $T > T^*$ to a negative value at $T < T^*$.

The recent rush for the discovery of new topological materials has renewed the interest on $ZrTe_5$, since it has been proposed to be either a 3D topological Dirac semimetal (TSM) or a weak or a strong topological insulator (WTI and STI, respectively).

Clarifying its topological and transport properties appears challenging for the variety of the apparent discordant results present in the literature. The reported values of T*, for example, are not unanimous and they can vary from 60 K up to 170 K. Several theories have been proposed to explain the origin of such anomalies, but they all have been rejected or no experimental evidences have been found.

The aim of this thesis work was to find an answer to these open questions about the electronic and topological character of $ZrTe_5$. Angle resolved photoelectron spectroscopy (ARPES) have been recognized as one of the most powerful technique for addressing this problem. The possibility to use ARPES with different probing photon sources has granted us to access a wide range of novel informations.

A study of the temperature behaviour of the electronic band structure of $ZrTe_5$ has given the possibility to reveal a rigid and non-monotonic shift of the electronic band structure, when the temperature of the material is changed [24, 25]. Measurements performed at 16 K have revealed a hole-like linear dispersion in proximity of the Fermi energy (E_F). The hole-like band crosses E_F both at room temperature and at 16 K but it moves towards higher binding energies when T* is approached. When the sample is at T*, only a Dirac point, and consequently a very low density of states, is crossing E_F. These findings explain the resistivity anomaly of $ZrTe_5$, unfortunately, the sign reversal of the thermopower is still not understood.

Having clarified the long-lasting question regarding the origin of the resistivity anomaly in $ZrTe_5$, the possibility to optically modify the electronic properties of this material was proved [24]. The use of a time resolved (Tr-) ARPES setup has opened to the possibility to heat the material on the ultrafast time scale and to observe its evolution in time. This result provide an external knob to control the $ZrTe_5$ conductivity and to unlock the route for a unique platform for magnetoelectric, optical, and thermoelectric transport applications.

Thanks to a comprehensive experimental and theoretical investigation of the electronic and structural properties of the bulk $ZrTe_5$ the STI character of the material has been proved [25–27]. Several experimental and theoretical techniques have been exploited: ultra violet (UV-) ARPES, soft X-ray (SX-) ARPES, circularly dichroic (CD-) ARPES, spin resolved (Sr-) ARPES, scanning tunneling microscopy (STM) and spectroscopy (STS), X-ray diffraction (XRD) and density functional theory (DFT) calculations. $ZrTe_5$ is found near a topological phase transition from the STI phase to the WTI phase. This phase transition can be triggered by an increase of the interlayer distance. The material is not a 3D TSM, as this phase is not protected by crystalline symmetry and it can only be realized precisely at the topological phase transition. Nonetheless, the band dispersion closely resembles the one of a 3D Dirac semimetal thus explaining the recent results reported by other groups.

The vicinity to the topological phase transition suggests the pos-

sibility of engineering the topological phase by a small variation of the interlayer distance, entering in the WTI phase. The topological phase transition may also be achieved in a controlled way either via alkali metal intercalation or via chemical substitution. This will require further ARPES investigations of ad hoc grown samples with controlled doping and/or defect density. Finally, the observed monotonic decrease of b/2 as a function of temperature suggests that, once the WTI phase is achieved, transition to the STI phase can be controlled by temperature, thus making $ZrTe_5$ a versatile platform for spintronics applications.

For all these reasons, the studies reported in this thesis advance the understanding of the topological nature and of the transport properties of $ZrTe_5$.

Bibliography

[1] S. Furuseth, L. Brattås and A. Kjekshus, *The Crystal Structure of $HfTe_5$*, Acta Chem. Scand. **27**, 2367 (1973).

[2] E. F. Skelton, T. J. Wieting, S. A. Wolf, W. W. Fuller, D. U. Gubser, T. L. Francavilla and F. Levy, *Giant resistivity and X-Ray diffraction anomalies in low-dimensional $ZrTe_5$ and $HfTe_5$*, Solid State Commun. **42**, 1 (1982).

[3] T. E. Jones, W. W. Fuller, T. J. Wieting and F. Levy, *Thermoelectric power of $HfTe_5$ and $ZrTe_5$*, Solid State Commun. **42**, 793 (1982).

[4] M.N. Ali, J. Xiong, S. Flynn, J. Tao, Q.D. Gibson, L. M. Schoop, T. Liang, N. Haldolaarachchige, M. Hirschberger, N.P. Ong and R. J. Cava, *Large, non-saturating magnetoresistance in WTe_2*, Nature **514**, 205 (2014).

[5] A. Tamai, Q. S. Wu, I. Cucchi, F. Y. Bruno, S. Riccó, T. K. Kim, M. Hoesch, C. Barreteau, E. Giannini, C. Besnard, A.

A. Soluyanov and F. Baumberger, *Fermi Arcs and Their Topological Character in the Candidate Type-II Weyl Semimetal $MoTe_2$*, Phys. Rev. X **6**, 031021 (2016).

[6] A. A. Soluyanov, D. Gresch, Z. Wang, Q. S. Wu, M. Troyer, X. Dai and B. A. Bernevig, *Type-II Weyl semimetals*, Nature **527**, 495 (2015).

[7] Z. Zhu, G. W. Winkler, Q. S. Wu, J. Li and A. A. Soluyanov, *Triple Point Topological Metals*, Phys. Rev. X **6**, 031003 (2016).

[8] S. Takahashi, T. Sambongi, J. W. Brill and W. Roark, *Transport and elastic anomalies in $ZrTe_3$*, Solid State Commun. **49**, 1031-1034 (1984).

[9] R.T. Littleton IV, T. M. Tritt, J. W. Kolis and D. R. Ketchum, *Transition-metal pentatellurides as potential low-temperature thermoelectric refrigeration materials*, Phys. Rev. B **60**, 13453 (1999).

[10] T. M. Tritt and R.T. Littleton IV, *Recent Trends in Thermoelectric Materials Research II - Semiconductors and Semimetals*, Elsevier, Vol. **70**, Chap. 6 (2001).

[11] F.J. DiSalvo, R.M. Fleming and J.V. Waszczak, *Possible phase transition in the quasi-one-dimensional materials $ZrTe_5$ or $HfTe_5$*, Phys. Rev. B **24**, 2935 (1981).

[12] M. Rubinstein, *$HfTe_5$ and $ZrTe_5$: Possible polaronic conductors*, Phys. Rev. B **60**, 1627 (1999).

[13] D.N. McIlroy, S. Moore, D. Zhang, J. Wharton, B. Kempton, R. T. Littleton IV, M. Wilson, T. M. Tritt and C. G. Olson, *Observation of a semimetal-semiconductor phase transition in the intermetallic $ZrTe_5$*, J. Phys. Condens. Matter **16**, L359 (2004).

[14] H. Weng, X. Dai and Z. Fang, *Transition-Metal Pentatelluride $ZrTe_5$ and $HfTe_5$: A Paradigm for Large-Gap Quantum Spin Hall Insulators*, Phys. Rev. X **4**, 011002 (2014).

[15] Z. Fan, Q.-F. Liang, Y. B. Chen, S.-H. Yao and J. Zhou, *Transition between strong and weak topological insulator in $ZrTe_5$ and $HfTe_5$*, arXiv:1611.04263v2 (2016).

[16] Q. Li, D.E. Kharzeev, C. Zhang, Y. Huang, I. Pletikosic, A.V. Fedorov, R.D. Zhong, J.A. Schneeloch, G.D. Gu and T. Valla, *Chiral magnetic effect in $ZrTe_5$*, Nature Physics **12**, 6, 550-555 (2016).

[17] R. Wu, J.-Z. Ma, S.-M. Nie, L.-X. Zhao, X.Huang, J.-X Yin, B.-B. Fu, P. Richard, G.-F. Chen, Z. Fang, X. Dai, H.-M. Weng, T. Qian, H. Ding and S. H. Pan, *Evidence for Topological Edge States in a Large Energy Gap near the Step Edges on the Surface of $ZrTe_5$*, Phys. Rev. X **6**, 02017 (2016).

[18] Y. Zhang, C. Wang, L. Yu, G. Liu, A. Liang, J. Huang, S. Nie, Y. Zhang, B. Shen, J. Liu, H. Weng, L. Zhao, G. Chen, X. Jia, C. Hu, Y. Ding, S. He, L. Zhao, F. Zhang, S. Zhang, F. Yang, Z. Wang, Q. Peng, X. Dai, Z. Fang, Z. Xu, C. Chen and X. J. Zhou, *Electronic Evidence of Temperature-Induced Lifshitz Transition and Topological Nature in $ZrTe_5$*, arXiV:1602.03576v1 (2016).

[19] L. Moreschini, J. C. Johannsen, H. Berger, J. Denlinger, C. Jozwiack, E. Rotenberg, K. S. Kim, A. Bostwick and M. Grioni, *Nature and topology of the low-energy states in $ZrTe_5$*, Phys. Rev. B **94**, 081101 (R) (2016).

[20] R. Y. Chen, S. J. Zhang, J. A. Schneeloch, C. Zhang, Q. Li, G. D. Gu and N. L. Wang, *Optical spectroscopy study of the three-dimensional Dirac semimetal $ZrTe_5$*, Phys. Rev. B **92**, 075107 (2015).

[21] R. Y. Chen, Z. G. Chen, X. Y. Song, J. A. Schneeloch, G. D. Gu, F. Wang and N. L. Wang, *Magnetoinfrared Spectroscopy of Landau Levels and Zeeman Splitting of Three-Dimensional Massless Dirac Fermions in $ZrTe_5$*, Phys. Rev. Lett. **115**, 176404 (2015).

[22] X.-B. Li, W.-K. Huang, Y.-Y. Lv, K.-W. Zhang, C.-L. Yang, B.-B. Zhang, Y. B. Chen, S.-H. Yao, J. Zhou, M.-H. Lu, L. Sheng, S.-C. Li, J.-F. Jia, Q.-K. Xue, Y.-F. Chen and D.-Y. Xing, *Experimental Observation of Topological Edge States at the Surface Step Edge of the Topological Insulator $ZrTe_5$*, Phys. Rev. Lett. **116**, 176803 (2016).

[23] L. Shen, M.X. Wang, S.C. Sun, J. Jiang, X. Xu, T. Zhang, Q.H. Zhang, Y.Y. Lv, S.H. Yao, Y.B. Chen, M.H. Lu, Y.F. Chen, C. Felser, B.H. Yan, Z.K. Liu, L.X. Yang and Y.L. Chen, *Spectroscopic evidence for the gapless electronic structure in bulk $ZrTe_5$*, accepted on Journ. Electron Spectrosc. Relat. Phenom. (2016).

[24] G. Manzoni, A. Sterzi, A. Crepaldi, M. Diego, F. Cilento, M. Zacchigna, Ph. Bugnon, H. Berger, A. Magrez, M. Grioni and F. Parmigiani, *Ultrafast Optical Control of the Electronic Properties of $ZrTe_5$*, Phys. Rev. Lett. **115**, 207402 (2015).

[25] G. Manzoni, A. Crepaldi, G. Autès, A. Sterzi, F. Cilento, A. Akrap, I. Vobornik, L. Gragnaniello, Ph. Bugnon, M. Fonin, H. Berger, M. Zacchigna, O. V. Yazyev and F. Parmigiani, *Temperature Dependent Non-Monotonic Bands Shift in $ZrTe_5$*, accepted on Journ. Electron Spectrosc. Relat. Phenom. (2016).

[26] G. Manzoni, L. Gragnaniello, G. Autès, T. Kuhn, A. Sterzi, F. Cilento, M. Zacchigna, V. Enenkel, I. Vobornik, L. Barba, F. Bisti, Ph. Bugnon, A. Magrez, V. N. Strocov, H. Berger, O. V. Yazyev, M. Fonin, F. Parmigiani and A. Crepaldi, *Evidence for a Strong Topological Insulator Phase in $ZrTe_5$*, Phys. Rev. Lett. **117**, 237601 (2016).

[27] G.Manzoni et al., *Spin Polarized States at the Surface in $ZrTe_5$*, in preparation (2016).

[28] Y. Zhou, J. Wu, W. Ning, N. Li, Y. Du, X. Chen, R. Zhang, Z. Chi, X. Wang, X. Zhu, P. Lu, C. Ji, X. Wan, Z. Yang, J. Sun, W. Yang, M. Tian and Y. Zhang, *Pressure-induced semimetal*

to superconductor transition in a three-dimensional topological material $ZrTe_5$, Proc. Natl. Acad. Sci. USA **113** (11), 2904-2909 (2016).

[29] J. Niu, J. Wang, Z. He, C. Zhang, X. Li, T. Cai, X. Ma, S. Jia, D. Yu, X. Wu, *Electrical transport in nano-thick $ZrTe_5$ sheets: from three to two dimensions*, Phys. Rev. B **95**, 035420 (2017).

[30] A. Pariari and P. Mandal, *Coexistence of topological Dirac fermions in the surface and three-dimensional Dirac cone state in the bulk of $ZrTe_5$ single crystal*, Sci. Rep. **7**, 40327 (2017).

[31] F. Levy and H. Berger, *Single crystals of transition metal trichalcogenides*, J. Cryst. Growth 61, 61 (1983).

[32] R.T. Littleton IV, T. M. Tritt, C. R. Feger, J. Kolis, M. L. Wilson and M. Marone, *Effect of Ti substitution on the thermoelectric properties of the pentatelluride materials $M_{1-x}Ti_xTe_5$ (M = Hf, Zr)*, Appl. Phys. Lett. **72**, 16 (1998).

[33] W. Yu, Y. Jiang, J. Yang, Z. L. Dun, H. D. Zhou, Z. Jiang, P. Lu and W. Pan, *Quantum Oscillations at Integer and Fractional Landau Level Indices in $ZrTe_5$*, arXiv:1602.06824 (2016).

[34] T. M. Tritt, N. D. Lowhorn, R. T. Littleton IV, A. Pope, C. R. Feger and J. W. Kolis, *Large enhancement of the resistive anomaly in the pentatelluride materials $HfTe_5$ and $ZrTe_5$ with applied magnetic field*, Phys. Rev. B **60**, 7816 (1999).

[35] G. Grüner, *The dynamics of charge-density waves*, Rev. Mod. Phys. **60**, 4 (1988).

[36] C. G. Kuper, *On the Thermal Properties of Frohlich's One-Dimensional Superconductor*, Proceedings of the Royal Society A (1955).

[37] D. E. Moncton, J. D. Axe and F. J. DiSalvo, *Study of Superlattice Formation in 2H-$NbSe_2$ and 2H-$TaSe_2$ by Neutron Scattering*, Phys. Rev. Lett. **34**, 734 (1975).

[38] P. Monçeau, N. P. Ong, A. M. Portis, A. Meerschaut and J. Rouxel, *Electric Field Breakdown of Charge-Density-Wave - Induced Anomalies in $NbSe_3$*, Phys. Rev. Lett. **37**, 602 (1976).

[39] J. A. Wilson, F. J. DiSalvo and S. Mahajan, *Charge-density waves and superlattices in the metallic layered transition metal dichalcogenides*, Adv. Phys. **24**, 117-201 (1975).

[40] J.C. Tsang, C. Hermann and M. W. Shafer, *Raman Spectroscopy of the Charge-Density Wave State in TaS_3*, Phys. Rev. Lett. **40**, 1528 (1978).

[41] K. Tsutsumi and M. Shimoda, *Charge-Density-Wave Behavior at Low Temperature in $K_{0.3}MoO_3$*, Jpn. J. Appl. Phys. **26**, 613 (1987).

[42] F. Clerc, C. Battaglia, H. Cercellier, C. Monney, H. Berger, L. Despont, M. G. Garnier and P. Aebi, *Fermi surface of layered compounds and bulk charge density wave systems*, J. Phys.: Condens. Matter **19**, 355002 (2007).

[43] J. P. Tidman and R. F. Frindt, *Resistivity of thin TaS_2 crystals*, Canad. J. of Phys., **54**, 23 2306-2309 (1976).

[44] G.N. Kamm, D. J. Gillespie, A. C. Ehrlich, T. J. Wieting and F. Levy, *Fermi surface, effective masses, and Dingle temperatures of $ZrTe_5$ as derived from the Shubnikov-de Haas effect*, Phys. Rev. B **31**, 7617 (1985).

[45] K. v. Klitzing, G. Dorda and M. Pepper, *New Method for High-Accuracy Determination of the Fine-Structure Constant Based on Quantized Hall Resistance*, Phys. Rev. Lett. **45**, 494 (1980).

[46] Nobelprize.org, http://www.nobelprize.org/nobel_prizes/physics/laureates/, *All Nobel Prizes in Physics* (2016).

[47] M. Z. Hasan and C. L. Kane, *Colloquium: Topological insulators*, Rev. Mod. Phys. **82**, 3045-3067 (2010).

[48] R. B. Laughlin, *Quantized hall conductivity in two dimensions*,Phys. Rev. B, vol. **23**, 5632 (1981).

[49] B. I. Halperin, *Quantized hall conductance, current-carrying edge states, and the existence of extended states in a two-dimensional disordered potential*, Phys. Rev. B **25**, 2185 (1982).

[50] T. Das, *A pedagogic review on designing model topological insulators*, arXiv: 1604.07546 (2016).

[51] L. Fu and C. L. Kane, *Topological insulators with inversion symmetry*, Phys. Rev. B, vol. **76**, 045302 (2007).

[52] D. J. Thouless, M. Kohmoto, M. P. Nightingale and M. den Nijs, *Quantized Hall Conductance in a Two-Dimensional Periodic Potential*, Phys. Rev. Lett. **49**, 405 (1982).

[53] S. Murakami, N. Nagaosa and S.-C. Zhang, *Dissipationless quantum spin current at room temperature*, Science, **301**, 1348 (2003).

[54] C. L. Kane and E. J. Mele, *Quantum Spin Hall Effect in Graphene*, Phys. Rev. Lett. **95**, 226801 (2005).

[55] M. Köning, S. Wiedmann, C. Brüne, A. Roth, H. Buhmann, L. W. Molenkamp, X.-L. Qi and S.-C. Zhang, *Quantum spin hall insulator state in HgTe quantum wells*, Science **318**, 766 (2007).

[56] C. L. Kane and E. J. Mele, Z_2 *topological order and the quantum spin hall effect*, Phys. Rev. Lett. **95**, 146802 (2005).

[57] B. A.Bernevig and S.-C. Zhang, *Quantum spin hall effect*, Phys. Rev. Lett. **96**, 106802 (2006).

[58] L. Fu, C. L. Kane and E. J. Mele, *Topological Insulators in Three Dimensions*, Phys. Rev. Lett. **98**, 106803 (2007).

[59] J. E. Moore and L. Balents, *Topological invariants of time-reversal-invariant band structures*, Phys. Rev. B **75**, 121306 (2007).

[60] R. Roy, *Topological phases and the quantum spin Hall effect in three dimensions*, Phys. Rev. B **79**, 195322 (2009).

[61] B. A. Bernevig, T. L. Hughes and S.-C. Zhang, *Quantum Spin Hall Effect and Topological Phase Transition in HgTe Quantum Wells*, Science **314**, 5806, 1757-1761 (2006).

[62] P. Hofmann, *Synchrotron-radiation studies of topological insulators*, arXiv:1210.2672 (2012).

[63] M. Bianchi, R. C. Hatch, D. Guan, T. Planke, J. Mi, B. B. Iversen and P. Hofmann, *The electronic structure of clean and adsorbate-covered Bi_2Se_3 : an angle-resolved photoemission study*, Semicond. Sci. Technol. **27**, 124001 (2012).

[64] D. Hsieh, D. Qian, L. Wray, Y. Xia, Y. S. Hor, R. J. Cava and M. Z. Hasan, *A topological Dirac insulator in a quantum spin Hall phase*, Nature **452**, 970 (2008).

[65] C. R. Ast and H. Höchst, *Fermi Surface of Bi(111) Measured by Photoemission Spectroscopy*, Phys. Rev. Lett. **87**, 177602 (2001).

[66] H. Zhang, C.-X. Liu, X.-L. Qi, X. Dai, Z. Fang and S.-C. Zhang, *Topological insulators in Bi_2Se_3, Bi_2Te_3 and Sb_2Te_3 with a single Dirac cone on the surface*, Nature Phys. **5**, 438 (2009).

[67] Y. Xia, D. Qian, D. Hsieh, L. Wray, A. Pal, H. Lin, A. Bansil, D. Grauer, Y. S. Hor, R. J. Cava and M. Z. Hasan, *Observation of a large-gap topological-insulator class with a single Dirac cone on the surface*, Nature Phys. **5**, 398 (2009).

[68] H.-J. Noh, H. Koh, S.-J. Oh, J.-H. Park, H.-D. Kim, J. D. Rameau, T. Valla, T. E. Kidd, P. D. Johnson, Y. Hu and Q. Li, *Spin-orbit interaction effect in the electronic structure of Bi_2Te_3 observed by angle-resolved photoemission spectroscopy*, Europhys. Lett. **81**, 57006 (2008).

[69] Y. L. Chen, J. G. Analytis, J.-H. Chu, Z. K. Liu, S.-K. Mo, X. L. Qi, H. J. Zhang, D. H. Lu, X. Dai, Z. Fang, S. C. Zhang, I. R.

Fisher, Z. Hussain and Z.-X. Shen, *Experimental Realization of a Three-Dimensional Topological Insulator, Bi_2Te_3*, Science **325**, 178 (2009).

[70] D. Hsieh, Y. Xia, D. Qian, L. Wray, J. H. Dil, F. Meier, J. Osterwalder, L. Patthey, J. G. Checkelsky, N. P. Ong, A. V. Fedorov, H. Lin, A. Bansil, D. Grauer, Y. S. Hor, R. J. Cava and M. Z. Hasan, *A tunable topological insulator in the spin helical Dirac transport regime*, Nature **460**, 1101 (2009).

[71] S. M. Young, S. Zaheer, J. C. Y. Teo, C. L. Kane, E. J. Mele and A. M. Rappe, *Dirac Semimetal in Three Dimensions*, Phys. Rev. Lett. **108**, 140405 (2012)

[72] Z. K. Liu, J. Jiang, B. Zhou, Z. J. Wang, Y. Zhang, H. M. Weng, D. Prabhakaran, S-K. Mo, H. Peng, P. Dudin, T. Kim, M. Hoesch, Z. Fang, X. Dai, Z. X. Shen, D. L. Feng, Z. Hussain and Y. L. Chen, *A stable three-dimensional topological Dirac semimetal Cd_3As_2*, Nat. Mater. **13**, 3990 (2014).

[73] X.-L. Qi and S.C. Zhang, *Topological insulators and superconductors*, Rev. Mod. Phys. **83**, 1057-1110 (2011).

[74] A. K. Geim and K. S. Novoselov, *The rise of graphene*, Nat. Mater. **6**, 183-191 (2007).

[75] Z. Wang, H. Weng, Q. Wu, X. Da and Z. Fang, *Three-dimensional Dirac semimetal and quantum transport in Cd_3As_2*, Phys. Rev. B **88**, 125427 (2013).

[76] K. Fukushima, D. E. Kharzeev and H. J. Warringa, *Chiral magnetic effect*, Phys. Rev. D **78**, 074033 (2008).

[77] Z. Wang, H. Weng, Q. Wu, X. Dai, and Z. Fang, *Three-dimensional Dirac semimetal and quantum transport in Cd_3As_2*, Phys. Rev. B **88**, 125427 (2013).

[78] C.Z. Li, L.-X. Wang, H. Liu, J. Wang, Z.-M. Liao and D.-P. Yu, *Giant negative magnetoresistance induced by the chiral anomaly in individual Cd_3As_2 nanowires*, Nat. Commun. **6**, 10137 (2015).

[79] S. Borisenko, Q. Gibson, D. Evtushinsky, V. Zabolotnyy, B. Büchner and R. J. Cava, *Experimental Realization of a Three-Dimensional Dirac Semimetal*, Phys. Rev. Lett. **113**, 027603 (2014).

[80] Z. K. Liu, B. Zhou, Y. Zhang, Z. J. Wang, H. M. Weng, D. Prabhakaran, S.-K. Mo, Z. X. Shen, Z. Fang, X. Dai, Z. Hussain and Y. L. Chen, *Discovery of a Three-Dimensional Topological Dirac Semimetal, Na_3Bi*, Science **343**, 6173, 864-867 (2014).

[81] Z. Wang, Y. Sun, X.-Q. Chen, C. Franchini, G. Xu, H. Weng, X. Dai and Z. Fang, *Dirac semimetal and topological phase transitions in A_3Bi (A=Na, K, Rb)*, Phys. Rev. B **85**, 195320 (2012).

[82] F. Arnold, C. Shekhar, S.-C. Wu, Y. Sun, R. Donizeth dos Reis, N. Kumar, M. Naumann, M. O. Ajeesh, M. Schmidt, A. G. Grushin, J. H. Bardarson, M. Baenitz, D. Sokolov, H. Borrmann, M. Nicklas, C. Felser, E. Hassinger and B. Yan, *Negative magnetoresistance without well-defined chirality in the Weyl semimetal TaP*, Nat. Commun. **7**, 11615 (2016).

[83] R. D. dos Reis, M. O. Ajeesh, N. Kumar, F. Arnold, C. Shekhar, M. Naumann, M. Schmidt, M. Nicklas and E. Hassinger, *On the search for the chiral anomaly in Weyl semimetals: the negative longitudinal magnetoresistance*, New J. Phys. **18** 085006 (2016).

[84] K. Banerjee, J. Son, P. Deorani, P. Ren, L. Wang and H. Yang, *Defect-induced negative magnetoresistance and surface state robustness in the topological insulator $BiSbTeSe_2$*, Phys. Rev. B **90**, 235427 (2014).

[85] J. B. Pendry, *Low-Energy Electron Diffraction*, Interaction of atoms and molecules with solid surfaces, Physics of Solids and Liquids, 201-211 (1988).

[86] S. Hüfner, *Photoemission Spectroscopy: Principles and Applications*, Springer-Verlag, 1995.

[87] H. Hertz, *Ueber sehr schnelle electrische Schwingungen*, Ann. Phys. **17**, 983 (1887).

[88] A. Einstein, *Ueber einen die Erzeugung und Verwandlung des Lichtes betreffenden heuristischen Gesichtspunkt*, Ann. Physik **31**, 132 (1905).

[89] A. Damascelli, *Probing the electronic structure of complex systems by ARPES*, Physica Scripta, **T109**, 61 (2004).

[90] G. D. Mahan, *Theory of photoemission in simple metals*, Phys. Rev. B **2**, 4334 - 4350 (1970).

[91] A. A. Abrikosov, L. P. Gorkov and I. E. Dzialoshinskii, *Quantum Field Theoretical Methods in Statistical Physics*, Pergamon, Elmsford (1965).

[92] L. Hedin, *Solid State Physics: Advances in Research and Applications*, Academic, New York (1969).

[93] G. D. Mahan, *Quantum Theory of Many-Particle Systems*, Plenum, New York (1981).

[94] G. Rickayzen, *Green's Functions and Condensed Matter in Techniques of Physics*, **7**, Academic, London (1991).

[95] W. L. Schaich and N. W. Ashcroft, *Model calculations in the theory of photoemission*, Phys. Rev. B **3**, 2452-2465 (1971).

[96] C. Caroli, D. Lederer-Rozenblatt, B. Roulet and D. Saint-James, *Inelastic effects in photoemission: microscopic formulation and qualitative discussion*, Phys. Rev. B **8**, 4552-4569 (1973).

[97] P. J. Feibelman and D. E. Eastman, *Photoemission spectroscopy-correspondence between quantum theory and experimental phenomenology*, Phys. Rev. B **10**, 4932-4947 (1974).

[98] H.Y. Fan, *Theory of photoelectric emission from metals*, Phys. Rev. **68**, 43-52 (1945).

[99] C. N. Berglund and W. E. Spicer, *Photoemission studies of copper and silver: theory* Phys. Rev. **136**, A1030-A1044 (1964).

[100] A. Damascelli, Z. Hussain and Z.-X. Shen, *Angle-resolved photoemission studies of the cuprate superconductors*, Rev. Mod. Phys. **75**, 473-541 (2003).

[101] G. W. Gobeli, F. G. Allen and E. O. Kane, *Polarization Evidence for Momentum Conservation in Photoelectric Emission from Germanium and Silicon*, Phys. Rev. Lett. **12**, 94 (1964).

[102] E. Dietz, H. Becker and U. Gerhardt, *Polarization Dependence of Angular-Resolved Photoemission from d Bands of Cu*, Phys. Rev. Lett. **37**, 115 (1976).

[103] T. Miller, W. E. McMahon and T.-C. Chiang, *Interference between Bulk and Surface Photoemission Transitions in Ag(111)*, Phys. Rev. Lett. **77**, 1167 (1996).

[104] F. Rodolakis, B. Mansart, E. Papalazarou, S. Gorovikov, P. Vilmercati, L. Petaccia, A. Goldoni, J. P. Rueff, S. Lupi, P. Metcalf and M. Marsi, *Quasiparticles at the Mott Transition in V_2O_3: Wave Vector Dependence and Surface Attenuation*, Phys. Rev. Lett. **102**, 066805 (2009).

[105] M. Hajlaoui, E. Papalazarou, J. Mauchain, L. Perfetti, A. Taleb-Ibrahimi, F. Navarin, M. Monteverde, P. Auban-Senzier, C. R. Pasquier, N. Moisan, D. Boschetto, M. Neupane, M. Z. Hasan, T. Durakiewicz, Z. Jiang, Y. Xu, I. Miotkowski, Y.P. Chen, S. Jia, H. W. Ji, R. J. Cava and M. Marsi, *Tuning a Schottky barrier in a photoexcited topological insulator with transient Dirac cone electron-hole asymmetry*, Nat. Comm. **5**, 3003 (2014).

[106] F. Offi, S. Iacobucci, P. Vilmercati, A. Rizzo, A. Goldoni, M. Sacchi and G. Panaccione, *Attenuation lengths of low-energy elec-*

trons in solids: The case of CoO, Phys. Rev. B **77**, 201101(R) (2008).

[107] C. L. Smallwood, J. P. Hinton, C. Jozwiak, W. Zhang, J. D. Koralek, H. Eisaki, D.-H. Lee, J. Orenstein and A. Lanzara, *Tracking Cooper Pairs in a Cuprate Superconductor by Ultrafast Angle-Resolved Photoemission*, Science **336**, 6085, 1137-1139 (2012).

[108] J. Graf, C. Jozwiak, C. L. Smallwood, H. Eisaki, R. A. Kaindl, D-H. Lee and A. Lanzara, *Nodal quasiparticle meltdown in ultrahigh-resolution pump-probe angle-resolved photoemission*, Nature Physics **7**, 805-809 (2011).

[109] J. C. Johannsen, S. Ulstrup, F. Cilento, A. Crepaldi, M. Zacchigna, C. Cacho, I. C. E. Turcu, E. Springate, F. Fromm, C. Raidel, T. Seyller, F. Parmigiani, M. Grioni and P. Hofmann, *Direct View of Hot Carrier Dynamics in Graphene*, Phys. Rev. Lett. **111**, 027403 (2013).

[110] I. Gierz, F. Calegari, S. Aeschlimann, M. Chávez Cervantes, C. Cacho, R. T. Chapman, E. Springate, S. Link, U. Starke, C. R. Ast and A. Cavalleri, *Tracking Primary Thermalization Events in Graphene with Photoemission at Extreme Time Scales*, Phys. Rev. Lett. **115**, 086803 (2015).

[111] L. Perfetti, P. A. Loukakos, M. Lisowski, U. Bovensiepen, H. Berger, S. Biermann, P. S. Cornaglia, A. Georges and M. Wolf, *Time Evolution of the Electronic Structure of 1T-TaS_2 through the Insulator-Metal Transition*, Phys. Rev. Lett. **97**, 067402 (2006).

[112] A. Crepaldi, B. Ressel, F. Cilento, M. Zacchigna, C. Grazioli, H. Berger, Ph. Bugnon, K. Kern, M. Grioni and F. Parmigiani, *Ultrafast photodoping and effective Fermi-Dirac distribution of the Dirac particles in Bi_2Se_3*, Phys. Rev. B **86**, 205133 (2012).

[113] M. Hajlaoui, E. Papalazarou, J. Mauchain, G. Lantz, N. Moisan, D. Boschetto, Z. Jiang, I. Miotkowski, Y. P. Chen, A. Taleb-Ibrahimi, L. Perfetti and M. Marsi, *Ultrafast Surface Carrier*

Dynamics in the Topological Insulator Bi_2Te_3, Nano Lett. **12**, 3532 (2012).

[114] J. A. Sobota, S. Yang, J. G. Analytis, Y. L. Chen, I. R. Fisher, P. S. Kirchmann and Z.-X. Shen, *Ultrafast Optical Excitation of a Persistent Surface-State Population in the Topological Insulator Bi_2Se_3*, Phys. Rev. Lett. **108**, 117403 (2012).

[115] Y. H. Wang, D. Hsieh, E. J. Sie, H. Steinberg, D. R. Gardner, Y. S. Lee, P. Jarillo-Herrero and N. Gedik, *Measurement of Intrinsic Dirac Fermion Cooling on the Surface of the Topological Insulator Bi_2Se_3 Using Time-Resolved and Angle-Resolved Photoemission Spectroscopy*, Phys. Rev. Lett. **109**, 127401 (2012).

[116] A. Sterzi, G. Manzoni, L. Sbuelz, F. Cilento, M. Zacchigna, Ph. Bugnon, H. Berger, A. Crepaldi, M. Grioni and F. Parmigiani, *Bulk Diffusive Relaxation Mechanisms in Optically Excited Topological Insulators*, Accepted on Phys. Rev. B (2017).

[117] C. L. Smallwood, C. Jozwiak, W. Zhang and A. Lanzara, *An ultrafast angle-resolved photoemission apparatus for measuring complex materials*, Rev. Sci. Instrum. **83**, 123904 (2012).

[118] J. Faure, J. Mauchain, E. Papalazarou, W. Yan, J. Pinon, M. Marsi and L. Perfetti, *Full characterization and optimization of a femtosecond ultraviolet laser source for time and angle-resolved photoemission on solid surfaces*, Rev. Sci. Instrum. **83**, 043109 (2012).

[119] F. Cilento, A. Crepaldi, G. Manzoni, A. Sterzi, M. Zacchigna, Ph. Bugnon, H. Berger and F. Parmigiani, *Advancing non-equilibrium ARPES experiments by a 9.3 eV coherent ultrafast photon source*, Journ. Electron Spectrosc. Relat. Phenom. **207**, 7 (2016).

[120] F. Frassetto, C. Cacho, C. A. Froud, I. C. E. Turcu, P. Villoresi, W. A. Bryan, E. Springate and Luca Poletto, *Single-*

grating monochromator for extreme-ultraviolet ultrashort pulses, Opt. Express **19**, 19169 (2011).

[121] M. Zonno, *Studio della dinamica delle quasi-particelle eccitate alla superficie di materiali Rashba di volume - A glance on hot quasiparticles dynamics at the surface of bulk Rashba materials*, Tesi di laurea Magistrale, Universitá degli Studi di Trieste (2014).

[122] V. N. Strocov, T. Schmitt, U. Flechsig, T. Schmidt, A. Imhof, Q. Chen, J. Raabe, R. Betemps, D. Zimoch, J. Krempasky, X. Wang, M. Grioni, A. Piazzalunga and L. Patthey, *High-resolution soft X-ray beamline ADRESS at the Swiss Light Source for resonant inelastic X-ray scattering and angle-resolved photoelectron spectroscopies*, Journ. Synchrotron Radiat. **17(5)**, 631-43 (2010).

[123] G. Panaccione, I. Vobornik, J. Fujii, D. Krizmancic, E. Annese, L. Giovanelli, F. Maccherozzi, F. Salvador, A. De Luisa, D. Benedetti, A. Gruden, P. Bertoch, F. Polack, D. Cocco, G. Sostero, B. Diviacco, M. Hochstrasser, U. Maier, D. Pescia, C. H. Back, T. Greber, J. Osterwalder, M. Galaktionov, M. Sancrotti and G. Rossi, *Advanced photoelectric effect experiment beamline at Elettra: A surface science laboratory coupled with Synchrotron Radiation.*, Rev. Sci. Instrum. **80**, 043105 (2009).

[124] C. Bigi, J. Fujii, I. Vobornik, P. K. Das, D. Benedetti, F. Salvador, G. Panaccione and Giorgio Rossi, *Very Efficient Spin Polarization Analysis (VESPA): New Exchange Scattering-based Setup for Spin-resolved ARPES at APE-NFFA Beamline at Elettra*, arXiv:1610.06922 (2016).

[125] S. LaShell, B. A. McDougall and E. Jensen, *Spin Splitting of an Au(111) Surface State Band Observed with Angle Resolved Photoelectron Spectroscopy*, Phys. Rev. Lett. **77**, 3419 (1996).

[126] A. L. Ryland, *X-ray diffraction*, J. Chem. Educ., **35**, 2, 80 (1958).

[127] N. W. Ashcroft and N. D. Mermin, *Solid State Physics*, Cengage learning (1976).

[128] C. Giacovazzo, H. L. Monaco, D. Viterbo, F. Scordari, G. Gilli, G. Zanotti and M. Catti, *Fundamentals of Crystallography*, International union of crystallography, Oxford Science Publications (1992).

[129] W. H. Bragg and W. L. Bragg, *The Reflection of X-rays by Crystals*, Proc R. Soc. Lond. A. **88** (605), 428-38 (1913).

[130] A. Crepaldi, L. Moreschini, G. Autés, C. Tournier-Colletta, S. Moser, N. Virk, H. Berger, Ph. Bugnon, Y. J. Chang, K. Kern, A. Bostwick, E. Rotenberg, O. V. Yazyev and M. Grioni, *Giant Ambipolar Rashba Effect in the Semiconductor BiTeI*, Phys. Rev. Lett. **109**, 096803 (2012).

[131] A. Pasquarello, M.S. Hybertsen and R. Car, *Si 2p Core-Level Shifts at the Si(001)-SiO_2 Interface: A First-Principles Study*, Phys. Rev. Lett. **74**, 1024 (1995).

[132] V. N. Strocov, *Intrinsic accuracy in 3-dimensional photoemission band mapping*, J. Electron Spectrosc. Relat. Phenom. **130**, 65-78 (2003).

[133] J. Braun, J. Minar, S. Mankovsky, V. Strocov, N. Brookes, L. Plucinski, C. M. Schneider, C. S. Fadley and H. Ebert, *Exploring the XPS limit in soft and hard x-ray angle-resolved photoemission using a temperature-dependent one-step theory*, Phys. Rev. B **88**, 205409 (2013).

[134] H. Fjellvåg and A. Kjejshus, *Structural properties of $ZrTe_5$ and $HfTe_5$ as seen by powder diffraction*, Solid State Commun. **60**, 91 (1986).

[135] P. Giannozzi, S. Baroni, N. Bonini, M. Calandra, R. Car, C. Cavazzoni, D. Ceresoli, G. L. Chiarotti, M. Cococcioni, I. Dabo,

A. Dal Corso, S. de Gironcoli, S. Fabris, G. Fratesi, R. Gebauer, U. Gerstmann, C. Gougoussis, A. Kokalj, M. Lazzeri, L. Martin-Samos, N. Marzari, F. Mauri, R. Mazzarello, S. Paolini, A. Pasquarello, L. Paulatto, C. Sbraccia, S. Scandolo, G. Sclauzero, A. P. Seitsonen, A. Smogunov, P. Umari and R. M. Wentzcovitch, *QUANTUM ESPRESSO: a modular and open-source software project for quantum simulations of materials*, J. Phys.: Condens. Matter **21**, 395502 (2009).

[136] A. Dal Corso and A. Mosca Conte, *Spin-orbit coupling with ultrasoft pseudopotentials: Application to Au and Pt*, Phys. Rev. B **71**, 115106 (2005).

[137] A. Crepaldi, F. Cilento, M. Zacchigna, M. Zonno, J. C. Johannsen, C. Tournier-Colletta, L. Moreschini, I. Vobornik, F. Bondino, E. Magnano, H. Berger, A. Magrez, Ph. Bugnon, G. Autés, O. V. Yazyev, M. Grioni and F. Parmigiani, *Momentum and photon energy dependence of the circular dichroic photoemission in the bulk Rashba semiconductors BiTeX (X=I, Br, Cl)*, Phys. Rev. B **89**, 125408 (2014).

[138] C. Jozwiak, Y. L. Chen, A. V. Fedorov, J. G. Analytis, C. R. Rotundu, A. K. Schmid, J. D. Denlinger, Y.-D. Chuang, D.-H. Lee, I. R. Fisher, R. J. Birgeneau, Z.-X. Shen, Z. Hussain and A. Lanzara, *Widespread spin polarization effects in photoemission from topological insulators*, Phys. Rev. B **84**, 165113 (2011).

[139] S. Souma, K. Kosaka, T. Sato, M. Komatsu, A. Takayama, T. Takahashi, M. Kriener, K. Segawa and Y. Ando, *Direct Measurement of the Out-of-Plane Spin Texture in the Dirac-Cone Surface State of a Topological Insulator*, Phys. Rev. Lett. **106**, 216803 (2011).

[140] S. Okada, T. Sambongi, M. Ido, Y. Tazuke, R. Aoki, and O. Fujita, *Negative Evidences for Charge/Spin Density Wave in* $ZrTe_5$, J. Phys. Soc. Jpn. **51**, 460 (1982).

[141] T. Eknapakul, P. D. C. King, M. Asakawa, P. Buaphet, R.-H. He, S.-K. Mo, H. Takagi, K. M. Shen, F. Baumberger, T. Sasagawa, S. Jungthawan and W. Meevasana, *Electronic Structure of a Quasi-Freestanding MoS_2 Monolayer*, Nano Letters **14**, 1312 (2014).

[142] J.C. Johannsen, G. Autés, A. Crepaldi, S. Moser, B. Casarin, F. Cilento, M. Zacchigna, H. Berger, A. Magrez, P. Bugnon, J. Avila, M. C. Asensio, F. Parmigiani, O. V. Yazyev and M. Grioni, *Engineering the topological surface states in the $(Sb_2)_m$ - Sb_2Te_3 superlattice series*, Phys. Rev. B **91**, 201101 (2015).

[143] J.A. Sobota, S.L. Yang, A.F. Kemper, J.J. Lee, F.T. Schmitt, W. Li, R.G. Moore, J.G. Analytis, I.R. Fisher, P.S. Kirchmann, T. P. Devereaux and Z. X. Shen, *Direct optical coupling to an unoccupied dirac surface state in the topological insulator Bi_2Se_3*, Phys. Rev. Lett. **111**, 136802 (2013).

[144] D. Pesin and A. H. MacDonald, *Spintronics and pseudospintronics in graphene and topological insulators*, Nature Materials **11**, 409 - 416 (2012).

List of Publications

- G. Manzoni, A. Sterzi, A. Crepaldi, M. Diego, F. Cilento, M. Zacchigna, Ph. Bugnon, H. Berger, A. Magrez, M. Grioni and F. Parmigiani
  Ultrafast Optical Control of the Electronic Properties of $ZrTe_5$
  Phys. Rev. Lett. **115**, 207402 (2015).

- G. Manzoni, L. Gragnaniello, G. Autès, T. Kuhn, A. Sterzi, F. Cilento, M. Zacchigna, V. Enenkel, I. Vobornik, L. Barba, F. Bisti, Ph. Bugnon, A. Magrez, V. N. Strocov, H. Berger, O. V. Yazyev, M. Fonin, F. Parmigiani and A. Crepaldi
  Evidence for a Strong Topological Insulator Phase in $ZrTe_5$
  Phys. Rev. Lett. **117**, 237601 (2016).

- F. Cilento, A. Crepaldi, G. Manzoni, A. Sterzi, M. Zacchigna, Ph. Bugnon, H. Berger and F. Parmigiani
  Advancing non-equilibrium ARPES experiments by a 9.3 eV coherent ultrafast photon source
  Journ. Electron Spectrosc. Relat. Phenom. **207**, 7 (2016).

- A. Sterzi, A. Crepaldi, F. Cilento, G. Manzoni, E. Frantzeskakis, M. Zacchigna, E. van Heumen, Y. K. Huang, M. S. Golden and F. Parmigiani

SmB_6 electron-phonon coupling constant from time- and angle-resolved photoelectron spectroscopy
Phys. Rev. B **94**, 081111(R) (2016).

- M. Dell'Angela, F. Hieke, M. Malvestuto, L. Sturari, S. Bajt, I. V. Kozhevnikov, J. Ratanapreechachai, A. Caretta, B. Casarin, F. Glerean, A. Kalashnikova, R. Pisarev, Y.-D. Chuang, G. Manzoni, F. Cilento, R. Mincigrucci, A. Simoncig, E. Principi, C. Masciovecchio, L. Raimondi, N. Mahne, C. Svetina, M. Zangrando, R. Passuello, G. Gaio, M. Prica, M. Scarcia, G. Kourousias, R. Borghes, L. Giannessi, W. Wurth and F. Parmigiani
Extreme ultraviolet resonant inelastic X-ray scattering (RIXS) at a seeded free-electron laser
Sci. Rep. **6**, 38796 (2016).

- A. Crepaldi, G. Autès, A. Sterzi, G. Manzoni, M. Zacchigna, F. Cilento, I. Vobornik, J. Fujii, Ph. Bugnon, A. Magrez, H. Berger, F. Parmigiani, O. V. Yazyev and M. Grioni
Persistence of a surface state arc in the topologically trivial phase of $MoTe_2$
Phys. Rev. B **95**, 041408(R) (2017).

- G. Manzoni, A. Crepaldi, G. Autès, A. Sterzi, F. Cilento, A. Akrap, I. Vobornik, L. Gragnaniello, Ph. Bugnon, M. Fonin, H. Berger, M. Zacchigna, O. V. Yazyev and F. Parmigiani
Temperature Dependent Non-Monotonic Bands Shift in $ZrTe_5$
Accepted on Journ. Electron Spectrosc. Relat. Phenom. (2016).

- A. Sterzi, G. Manzoni, L. Sbuelz, F. Cilento, M. Zacchigna, Ph. Bugnon, H. Berger, A. Crepaldi, M. Grioni and F. Parmigiani
Bulk Diffusive Relaxation Mechanisms in Optically Excited Topological Insulators
Accepted on Phys. Rev. B (2017).

- A. Crepaldi, G. Autès, G. Gatti, S. Roth, A. Sterzi, G. Manzoni, M. Zacchigna, C. Cacho, R. Chapman, E. Springate, Ph. Bugnon, A. Magrez, H. Berger, I. Vobornik, M. Kalläne, K. Rossnagel, F.

Parmigiani, O. V. Yazyev and M. Grioni
Ultrafast electron dynamics reveals the emergence of the Weyl points in the type-II Weyl semimetal $MoTe_2$
Submitted to Nat. Phys. (2017).

- F. Cilento, G. Manzoni, A. Sterzi, S. Peli, A. Ronchi, A. Crepaldi, F. Boschini, C. Cacho, R. Chapman, E. Springate, M. Capone, M. Berciu, A. Kemper, A. Damascelli, C. Giannetti and F. Parmigiani
Antinodal collapse in superconducting copper oxides driven by charge-transfer manipulation
ArXiv: 1703.03877 (2017).

- G. Manzoni et al.
Spin Polarized States at the Surface in $ZrTe_5$
In preparation.

- A. Sterzi, G. Manzoni et al.
Linear Dichroic Signal in the ARPES study of the Topological Insulator $GeBi_2Te_4$
In preparation.